To the Graduate Council:

I am submitting herewith a dissertation written by Andreas Boller entitled "The Thermal Analysis of Gel-Spun Ultra-High Molar Mass Polyethylene Fibers." I have examined the final copy of this dissertation for form and content and recommend that it be accepted in partial fulfillment of the requirements for the degree of Doctor of Philosophy, with a major in Chemistry.

Bernhard Wunderlich, Major Professor

We have read this dissertation
and recommend its acceptance:

Accepted for the Council:

Associate Vice Chancellor and
Dean of The Graduate School

The Thermal Analysis of Gel-Spun Ultra-High Molar Mass Polyethylene Fibers

A Dissertation

Presented for the

Doctor of Philosopy

Degree

The University of Tennessee, Knoxville

Andreas Boller

December 1996

DEDICATION

This thesis is dedicated to my wife

Maria Cecilia Austin

without whose support

this work might never be finished

Acknowledgments

I am grateful to my major professor, Dr. Bernhard Wunderlich for giving me the opportunity to work on this interesting topic. I would also like to thank the other committee members, Dr. S.D. Alexandratos, Dr. G. Bhat, Dr. M. Dadmun and Dr. J. Spruiell, for the support in the progress of my thesis. My thanks also extend to Dr. Yigang Fu, for the measurement and analysis of the full pattern wide angle x-ray scattering data, to Dr. Wei Chen for the measurements of the solid state NMR data, Dr. A. Habenschuss for the measurement of the powder x-ray diffraction, and Dr. B. Annis for supplying the small-angle x-ray scattering data. Thanks are extended to Dr. S. Kavesh of Allied-Signal Inc. for providing the samples and information of the mechanical properties of PE-I and PE-IV, T. Y. Tam of Allied-Signal Inc. for providing samples PE-II and PE-III, Professor M. Yasuniwa of Fukuoka University, Japan, for providing sample PE-V, and Dr. G. Bhat , for providing sample PE-VI. I would also like to thank the support staff at the Department of Chemistry for providing an environment conducive to research. Special thanks go to B. Gurley and J. Jones for keeping the computers in the best conditions, and T. Free at the machine shop, for the support with the design of the fiber winding tool.

The author also gratefully acknowledges constructive discussions with Dr. M. Reading, ICI Paints, Messrs. L. Thomas and B. S. Crowe of TA Instruments, R. Truttmann of Mettler-Toledo, and all attendees of the Third and Fourth

Lähnwitz Seminar regarding the development of the best method of measuring the fiber heat capacities. Special thanks are extended to Dr. Ch. Schick, University of Rostock, and Dr. G. Höhne, University of Ulm, for providing the means to perform some experiments at their respective facilities. I would like to thank the US Department of Energy, the National Science Foundation and ICI Paints for providing research funds. The support for instrumentation, coming from Mettler-Toledo, and TA Instruments, Inc. is also appreciated - many of the results could not have been obtained without it.

A very special acknowledgment is given to Dr. Michael Keene, whose teaching in 'writing for publication' gave me the tools to write, and also to Tom Griffith, who pointed out my many mistakes in writing, thus enabling me to communicate better.

There are many colleagues, friends and well-wishers who have helped me and given me cheerful inspiration. The paucity of space does not permit me to mention them, but I will never forget. Last, but not least, I would like to express my sincere appreciation to my wife, Maria Cecilia Austin, and my family in Switzerland, for their patience, understanding, and strong support.

Abstract

The thermal analytical properties of gel-spun ultra-high molar mass polyethylene (UHMMPE) fibers were studied with differential scanning calorimetry (DSC), thermo-optical analysis (TOA), and thermo-mechanical analytical (TMA) methods. The thermal analysis data were combined with the results from full-pattern x-ray diffraction analysis, small-angle x-ray scattering, powder x-ray diffraction, and solid state ^{13}C nuclear magnetic resonance experiments. At room temperature, these fibers show mainly the common orthorhombic and a small amount of monoclinic crystals, in addition to an intermediate, oriented fraction and a minimal amount of amorphous phase. The structure parameters of the orthorhombic phase change slightly with the processing history. The chains of the intermediate phase have a largely *trans*-conformation and are oriented preferentially parallel to the fiber axis, but are disordered laterally. The mobility (correlation time) of the carbon atoms of the intermediate phase is higher than that of the crystalline phase by one order of magnitude, but lower than that of the amorphous phase by one order of magnitude. The intermediate phase can contribute significantly to the meridional x-ray diffraction peaks 00ℓ, but not to the equatorial peaks $hk0$. A simple structural model is proposed to reconcile the experimental results.

This dissertation contains the first published account of heat capacities of UHMMPE fibers. The results from these heat capacity measurements show that

the post-drawing of the gel-spun fibers creates structures which have the same heat capacity, C_p, throughout the range of 175 to 400 K. The non-post-drawn fiber, in contrast, shows a step-increase in heat capacity in the temperature range from 260 to 290 K. Comparisons with the vibrations-only and the experimental, 100%-crystalline, extended-chain polyethylene heat capacities lead to the conclusion that the intermediate, non-crystalline material has a steady increase of C_p from 180 to 290 K. This increase is interpreted as the mesophase glass transition. The increase from 290 to 360 K is solely due to the increase in gauche conformations. At 360 K the locally reversible melting of the non-crystalline intermediate starts. The mass dependent DSC experiments revealed that melting occurred in one step at 412 K, opposed to the often cited multiple-stage melting. The one-step melting was confirmed by optical observation of the melting of UHMMPE fibers in a microscopy hot-stage and thermomechanical analysis. This one-step melting behavior combines the isotropization of the crystalline and the mesophase material into one transition. The two phases are therefore highly connected and interdependent. It is concluded that such behavior requires a nano-phase separation of the mesophase and the crystalline phase.

The mesophase model suggested by the experimental data allows a correlation of the structure to properties.

"Where shall I begin, please your Majesty?" he asked.

"Begin at the beginning," the King said gravely, "and go on till you come to the end: then stop."

Table of Contents

List of Figures

Chapter 1

Introduction

The research described in this thesis was designed to establish the thermal properties of ultra-high molar mass polyethylene fibers. Standard and novel thermal analysis techniques are used in their characterization. Both, NMR and x-ray techniques were used to add microscopic information about fiber structure and molecular motion. These analyses were carried out in cooperation with Drs. Y. Fu, W. Chen, A. Habenschuss and B. Annis at The University of Tennessee, Knoxville, and the Oak Ridge National Laboratory (ORNL). All data were used to arrive at a better understanding of the fiber structure, properties and processing. The experiments performed during this thesis lead to the first published values of heat capacities of fibers. The existence of an intermediate non-crystalline phase was further established and supporting evidence to the fact of nano-phase separation of the crystalline and non-crystalline phases was collected.

1.1 Justification & Goal

Heat capacity values of polyethylene fibers are required for the link between experimentally determined properties and the thermodynamic functions. Until this work, no heat capacity data on polyethylene fibers were available. With the heat capacity reported in this thesis, this key element is provided.

The goal of this thesis is to establish the thermal properties of UHMMPE fibers and to compare the thermal properties with the physical properties as established by structural (X-ray, NMR) and mobility analysis (NMR). The discussion is extended to the relationship between the mechanical behavior and morphology by combining mechanical and structural data from gel-spun UHMMPE fibers.

The structure of polyethylene (PE) fibers has been widely studied [1-3]. Considerable evidence has been accumulated for oriented, noncrystalline chains in some PE fibers. These oriented, noncrystalline chains play an important role in the understanding of fiber properties. Extensive efforts have been devoted to the development of mathematical modeling or simulation of polymer processes to develop sophisticated manufacturing methods. However, according to the National Research Council [4], much remains to be done.

The sophistication of the models used and the accuracy of the input data are always the major issues. In spite of their computational complexity, such models answer only simple process questions. Molecular-based models of flow behavior are emerging which, if properly combined with a process model, are likely to be able to answer more subtle questions about both the process and the product. For example, beyond simply determining the filling of the mold, predicting the crystallinity and molecular orientation (and thus the mechanical properties of the product) would be useful. Many of the current efforts focus on the basic understanding of the effects of phase transitions and anisotropy. For the modeling of fiber properties, many models require several phases (see Ref.

[5] p. 315ff). In this research, the properties of the individual phases and their transitions are investigated with the model of a nano-phase separated multi-phase material.

The relationship between processing and properties, particularly for complex polymer systems, is not fully developed. New probes for the determination of structure during processing would be of immense value. Until that day, however, analysis of the final product is in order. Of course, a linkage must be made between the structure generated during processing and the performance of the product.

Over the past 40 years, the semicrystalline state of flexible polymers has been the subject of many investigations. Some theoretical understanding has been generated concerning the thermodynamics and kinetics of crystallization. However, this area still has many unanswered questions. For example, the structure and properties of the crystal-amorphous interphase and their dependence on chemical structures need more attention because of their technological importance for high-performance materials. Also needed is a better understanding of chain topology, such as chain entanglements and tie-chains interconnecting crystals in the intercrystalline region. The variation of entanglement and intercrystalline structure with crystallization conditions, and its influence on final material properties needs to be established. Theoretical and simulation studies should aid in improving the properties of polyethylene and many other synthetic fibers and films [4].

1.2 Polyethylene

Expressed by the smallest repeating unit $(CH_2-)_n$, polyethylene (PE, source based name) has the same structural formula as poly(methylene) (structure-based name). Polyethylene is one of the world's most used polymers. Despite much research, open questions about the thermodynamic properties of the material in its anisotropic forms still exist. The results of this thesis resolve the problem of unavailable heat capacity data and the question of the multiple melting peaks in the DSC experiments. Ultra high molar mass polyethylene (UHMMPE) is the material used for the formation of high performance fibers through a gel-spinning and post-stretching process. The resulting fibers are used in many applications. These range from the manufacturing of low density, high-performance composites to bulletproof vests. All these properties are the result of the structure generated by the specific manufacturing process. Only a combination of methods can lead to the understanding of the structure of the UHMMPE fibers. The collection of all the parameters from the processing and analysis is expected to yield further insight into the processing-structure-property relationship.

1.3 Three-Phase Treatment for Highly Anisotropic Polymeric Materials

Polymer fibers are traditionally considered a two-phase system frozen in a nonequilibrium structure. These phases are the crystalline and amorphous

material. If more than one crystal form is present, each of these is treated independently as a crystalline phase. The amorphous phases below and above its glass transition exhibits different properties, each of which need to be accounted for. In this connection the term "phase" must be understood as micro phase because typical crystalline and amorphous phases in a semicrystalline polymer are usually only 5-50 nm in one or more dimensions. The smallest crystals and amorphous areas may even be nanophases, *i.e.,* they are not only influenced by surfaces and interfaces but also experience interactions between surfaces on opposite sides of the crystal. The molecular segments immediately surrounding the crystals, with strained connections to them, are thought to be the major part of the intermediate phase.

The three-phase approach to polymers with highly anisotropic features requires the introduction of an "intermediate phase" or mesophase. It is assumed that at a point between the glass transition of the amorphous and the melting transition, this "third phase" or "rigid amorphous phase" gains mobility and therefore shows a transition in the thermal analysis experiments. The mesophase may have both a mesophase glass transition and one or more disordering transitions. Thermal analysis techniques are therefore most likely able to confirm the existence of such a phase. Such an attempt is presented in the results section of this thesis.

The highly anisotropic ultra-high molar mass polyethylene (UHMMPE) fibers cannot be treated in a satisfactory way by the standard two-phase model. Experiments done by X-ray, NMR, RAMAN, IR and thermal analysis point to the

need for a more elaborate model (Chapter 2). The measurements presented are interpreted with an improved multi-phase approach, which will be discussed in Chapter 6.

1.4 Thermal Properties

The thermodynamic properties of polyethylene will be briefly described. A more detailed treatment of the general thermodynamic principles involved in the determination and evaluation of heat capacity data by differential scanning calorimetry (DSC) will be given in Chapter 3.

1.4.1 Heat Capacity

Analysis of the heat capacity offers a way to establish the relative stabilities of various metastable forms of chemically identical, but morphologically and conformationally different, polymeric materials. The analysis of heat capacity and transition enthalpies, permit to derive values of enthalpy, entropy, and Gibbs free energy, integral functions which are the basis of the thermodynamic characterization of any material. Heat capacities and enthalpies of transition are preferably obtained in separate calorimetry experiments with instrument parameters adjusted for optimum results. In principle, both experiments allow obtaining the crystallinity of a particular sample. In the heat capacity measurement, the crystallinity can be regarded as a function of temperature, while the determination of the transition enthalpy gives the crystallinity only at the

transition temperature. The results of the temperature dependent crystallinity are compared with the crystallinity from transition enthalpy measurements. An attempt is also made to link the temperature-dependent crystallinity to the multi-phase approach for anisotropic polymeric material.

1.4.2 Glass Transition

The glass transition is a universal phenomenon of all matter that solidifies as a fully or partially disordered structure. The temperature at which the material solidifies on cooling, as well as the temperature at which this transition occurs on heating, is characteristic for the loss or gain of large amplitude molecular mobility. The macroscopic (or engineering) properties and the utility of the material change drastically at the glass transition. The glass transition is characterized by a step-increase in heat capacity. The glass transition temperature is defined as the temperature at half of the step of the heat capacity. The heat capacity increases from the heat capacity of the vibration-only solid to the heat capacity of the liquid. Glass transitions exist both for amorphous and mesophase glasses.

1.4.3 Melting

First order phase changes occur in materials with well-defined phases before and after the change particularly in the melting of small molecules which have sharp phase transitions. The mesophases (liquid crystals, plastic crystals and condis

crystals) also show often first order phase changes. A more detailed discussion of the first order transition is given in Chapter 3.

1.4.4 Polymer Melting

The melting of a metastable, polymeric material involves often not a simple first order phase change but is complicated by simultaneous effects, such as lamellar thickening, annealing, and melting of smaller crystals and subsequent crystallization onto larger crystals. Caution has to be taken to extract the analysis of the first order phase transition which characterizes the melting of the polymer from these multiple processes. In the course of this thesis, the melting behavior of the UHMMPE fibers was investigated.

1.4.5 Multiple Melting Peaks

Research on UHMMPE fibers must answer the question of multiple melting peaks in UHMMPE fibers. Several solutions have been proposed without conclusive answers. The origin of the multiple melting peaks will be shown to be inherent to the packing of the sample and in part due to thermal gradients within the sample pan, using experiments with variable mass. Doing experiments with as small a mass as is possible will be shown to be one solution for the problem. Another solution to eliminate these gradient problems is the use of a mixture with sufficient thermal conductivity (e.g., a mixture with anhydrous aluminum oxide), as will be presented in Chapter 5.

1.4.6 Shrinkage

The shrinkage of polymers needs to be linked to the microscopic mobility of the individual C-C bonds. The gain of mobility in the segments causes macroscopically observable shrinkage. Thermo-mechanical analysis (TMA) of the polymer fibers is expected to display shrinkage in two distinct temperature regions, the glass transition and the melting/crystallization region. In the case of a substantial presence of rigid amorphous material, the shrinkage is expected to be occurring between the glass and the melting transition. For the fibers in this study, the shrinkage only occurs simultaneously with the melting transition. This is an indication of the tight link between the crystalline and the non-crystalline material in the fiber, for which the only plausible explanation is a nano-phase separation. Nano-phase separation has a particularly strong effect when the individual macromolecules reach over many phase boundaries.

1.5 Processing Structure Property Relationship

The application of academic research to the applied engineering sciences has formed the basis for many discussions. With the results from the research presented here, it is hoped that a link can be made from basic science to the application of materials science. Future research in open cooperation with manufacturers of polymeric fibers is proposed to achieve maximum benefit (Chapter 8). Defining the processing-structure-property relationship is the ultimate goal, but it is hardly possible without the free exchange of information.

****

Overall, this thesis deals with the integration of basic research and applied fiber science. The findings are expected to be directly applicable to the understanding of the processing-property relationship.

In the present work, the thermal analysis methods of differential scanning calorimetry (DSC), thermo-mechanical analysis (TMA) and thermomicroscopy (TOA) were used for characterization of the fibers. In addition, the full-pattern wide-angle X-ray diffraction (FPWAXD), small-angle X-ray scattering (SAXS), and solid-state nuclear magnetic resonance (NMR) provided information on structure and mobility. Only the combination of all methods will give a complete answer to the question of how processing, structure, and ultimate properties are related.

Chapter 2

Review of Materials Properties of Polyethylene

2.1 General information

2.1.1 Historical

Commercial production of polyethylene commenced in England during the early 1940s using a free radical process operating at very high pressures (200 -350 MPa). The structure was far more complex than the simple textbook repeat unit, -CH2-, would suggest. The backbone has short- and long-chain branches. The short-chain branches, four carbons long, interfere with the ability of the chain to crystallize, thus affecting solid-state properties. The long-chain branches (comparable in length to half the backbone), on the other hand, mainly affect the melt rheological or flow properties that influence processing behavior. Because the short-chain branches reduce crystallinity and, thus, density, this material is called low-density polyethylene (LDPE).

In the late 1950's, a linear or unbranched form of polyethylene was developed because of advances in coordination polymerization catalysis. An accidental finding by K. Ziegler in the early 1950s at the Max Planck Institute of Mulheim, Germany, resulted in a new approach to polyolefins [6]. It was found that transition metal complexes could catalyze the polymerization of ethylene to

produce linear chains with more controlled structures at atmospheric pressure. As a result, this polymer is more crystalline with higher density and known as high-density polyethylene (HDPE). Similar procedures were used by G. Natta [7] to produce crystalline polypropylene. The properties of this polymer are a result of unprecedented control of the stereochemistry of polymerization.

Because of the effects of molecular structure on crystallinity, HDPE is as much as five times stronger and one order of magnitude stiffer than LDPE. The newer material did not replace the older one; it was used for different purposes. In the 1970s, the high-pressure LDPE process became increasingly expensive compared with the lower-pressure HDPE process. The cost factor plus innovations in catalysts and process technology led to a new material that had most of the attributes of LDPE but was produced by a more economical low-pressure process similar to that used for HDPE. It is a copolymer of ethylene and an alpha-olefin (like 1-butene, 1-hexene). Therefore, short-chain branches of controlled length and number are introduced into the chain without long-chain branches, and the material is called linear low-density polyethylene (LLDPE).

Production of this material grew at a rate of 20% per year during the 1980s to a current usage of more than 10^9 kilograms per year. As a result, the production of LDPE initially declined, but its production has been growing again since 1986. Construction of new high-pressure production facilities may be required in the next decade to meet demands. Currently, this is the only process by which copolymers can be made with polar monomers such as vinyl acetate or acrylic acid. The HDPE is fabricated primarily by molding. Blow-molded food

bottles and gasoline tanks are major markets. Very large containers made by rotational molding, represent a specialized growth area.

A process known as 'gel-spinning' has been commercialized, which produces fibers of ultrahigh molar mass polyethylene. Polymers with ultrahigh molar mass are defined as having molar masses greater than 10^6 Da. The less crystalline LDPE and LLDPE are primarily extruded into thin film products with each having specialized uses. New technology based on single-site metallocenes holds promise for the production of a new range of products.

2.1.2 Processing of UHMMPE into Fibers

The extraordinary properties of fibers are based on the extension of the individual molecules along the fiber axis. This is achieved by drawing the extruded fiber in a second step. The ultimate draw ratios for ultra high molar mass polyethylene are in the order of 5-10x for melt spun fibers. The process of gel-spinning [8] greatly reduces the entanglements between the polymer molecules and therefore allows draw ratios exceeding 150x.

Gel-spinning technology represents a major breakthrough in fiber processing because it succeeds in preparing ultra strong fibers from flexible molecules such as polyethylene, poly(vinyl alcohol) and polyacrylonitrile.

The formation of high-tenacity fibers through gel spinning and drawing of UHMMPE is a prime example for realizing the theoretical potential of polymers as high-performance materials [9]. The gel spinning starts with a solution of UHMMPE. The solvents used in industrial processes are paraffin oil, wax, or

decalin. The dissolution temperature is approximately 420 K. This solution is extruded in air, (approx. 408 K) where the solvent and the polymer phase separate and a transformation into a gel takes place. Then the high boiling solvent is extracted with a low-boiling nonsolvent for PE, such as *n*-hexane, and the porous fiber is, next, hot drawn at 390 K to draw ratios from 40 to 80x, free of solvent. The stretching of a molecular network with controlled amounts of entanglements, due to the gel-precipitation, to such a high extent forms the highly aligned spatial architecture. A careful balance of entanglements and molecular length is believed to be the basis of successful gel spinning. This is in contrast to melt-extruded fibers where entanglements prevent extensions beyond 5-10x [9]. The special properties of these very strong fibers are attributed to the high orientation of the macromolecules in the gel.

2.1.3 PE Properties

Polyethylene is a macromolecule containing only one chain atom per repeat unit. The only stable crystal form for PE is orthorhombic [2]. It has a packing density of 0.70. The crystal system is orthogonal with the space group *Pnam* and a 1*2/1 helix. The unit cell axes are a = 0.742, b = 0.495 and c = 0.254 nm, with 4 repeat units per unit cell. The resulting crystal density is 0.9972 Mg/m^3. The monoclinic unit cell is: *a* = 0.809, *b* = 0.479, *c* = 2.53 nm, γ = 107.9° [10], in early analyses the monoclinic phase is sometimes described by its primitive triclinic unit cell [2].

In addition, a hexagonal phase [11-13], which has also been called a rotator phase, corresponds to the definition of a conformationally disordered (CONDIS) phase [13]. This metastable phase has great significance for the crystal perfection, and its implications for the fiber properties will be discussed in Chapter 6.

The C-H bond length is 0.1069 nm, the C-C bond length is 0.153 nm, the H-C-H bonding angle is 107°, and the C-C-C bond-angle is 112°.

2.2 Results by analysis technique

2.2.1 X-ray

Fiber x-ray diffraction patterns record the diffraction intensities of all components of a fiber. The presence of the oriented, noncrystalline chains may, because of their similarity to the crystalline chains, contribute to the intensities of some crystal diffraction peaks. Only if the diffraction intensities of the crystalline phase can be deconvoluted from those of the oriented, non-crystalline chains can a more detailed structure information of the latter be obtained. This process involves a full-pattern (two-dimensional profile) fitting to first determine and then remove the diffraction intensity of the crystalline phase [14,15]. The fiber x-ray diffraction method where each reflection is treated as a single point cannot accomplish this task. This is one reason for the limited progress in

understanding of fibers, despite the solution of the PE crystal structure more than 50 years ago [16].

The recent development of the full-pattern (two-dimensional Rietveld) fiber x-ray diffraction refinement method [14,15,17-23] overcomes the disadvantage of the traditional x-ray fiber diffraction method. Each reflection peak is fully characterized. The positions, the maximum intensities, and the two-dimensional profiles of all measurable diffraction peaks are used to derive crystal structure morphological parameters. Besides a more detailed and accurate crystal structure, the full-pattern x-ray diffraction method permits the quantitative separation of the non-crystalline scattering from the overall scattering pattern for further structure analysis. Details will be given in the experimental section.

In an earlier study of semicrystalline poly(ethylene terephthalate) (PET) fibers, the advantages of the full-pattern method were shown [14,15,17]. It was found that two types of oriented chains, a crystalline and an intermediate phase, exist. Removal of the crystalline diffraction by the full-pattern method revealed the noncrystalline scattering. Further removal of the azimuthally isotropic scattering of the amorphous phase revealed the anisotropic scattering of the intermediate phase. The chains of the intermediate phase have some degree of preferential orientation parallel to the fiber axis and are the main load-bearing fraction in the PET fiber [14].

In a first attempt, the full-pattern method had previously been applied in a study of a UHMMPE fiber [23]. In this study an attempt was made to fit the intensities of diffraction peaks in two dimensions to a single, disordered crystal

structure. For this attempt one had to assume multiple *equivalent* positions for the asymmetric unit of the crystal. These positions had to be randomly and fractionally occupied. About 20% of the carbon atoms had to be assigned to positions of disorder. The present interpretation suggests a much more plausible structure and brings the x-ray results into agreement with the interpretation of other analysis methods.

Kavesh and Schultz [24] reported on the development of an x-ray diffraction method for the simultaneous determination of crystallinity (including intra-crystalline defects), effective Debye-Waller factors, and atomic positions. They applied this method to semicrystalline polyethylene. According to their interpretation this material is a two-phase system. They measured intra-crystalline lattice disorder in the chain direction and perpendicular to the chain direction in the ratio 1:2.5. Paracrystalline disorder in the [110] direction was less than 2.4% at all experimental conditions. Their results include measurements of degree of crystallinity, particle size, space group, and unit cell parameters and variation of these quantities with crystallization temperature, ambient (storage) temperature, and time. The results of the present study are in contrast to this assessment and studies need to be performed on the identical samples.

2.2.2 NMR

An oriented, noncrystalline phase with predominantly *trans*-conformations, *i.e.,* the intermediate phase, has been proposed in a previous publication of a solid state ^{13}C NMR study of an ultra-high-molecular-mass (UHMMPE fiber [25]. The

chemical shift of the NMR resonance peak is the same for carbon atoms of both the orthorhombic and the intermediate phases. The mobility of the carbon atoms of the intermediate phase is, however, much higher than in the orthorhombic phase. Similar results have been reported by other researchers [26-28] who separated three oriented phases of different mobility. The relaxation times are known to change considerably from fiber to fiber. Their conformation is that of a *trans* zig-zag-chain, as in the crystalline phases, but their lateral packing is less perfect. Presence of two oriented components has also been reported in a two-dimensional ^{13}C NMR study of other UHMMPE samples [28].

The separation of the proton NMR signal into a Lorentzian function (corresponding to spins in regions that are motionally narrowed) and a Gaussian function (corresponding to spins in regions that are not motionally narrowed) has been performed by Kauffman and Dybowski [29]. They therefore conclude that domains of different mobility exist. These domains are isolated for NMR spectroscopy which allows a quantitative analysis of the amount of non-crystalline material. Spin diffusion between domains would make it difficult to determine the crystalline content accurately through a proton line shape study.

According to Cheng et al. [30], the observation of chain conformation and mobility in polyethylene by solid state ^{13}C magic-angle-spinning (MAS) nuclear magnetic resonance (NMR) permits identification and quantitative analysis of an intermediate phase. On average, the carbon-carbon bonds in the intermediate phase adopt an all-*trans* conformation and are more mobile than in the crystalline state (room temperature rate of reorientation approx. 10^7 Hz). Comparisons of

crystallinities by differential scanning calorimetry, wide angle x-ray diffraction, and NMR support the high orientation of the intermediate phase and suggest a lower heat of fusion than for the crystals. Results from ^{13}C spin-lattice relaxation and ^{1}H spin diffusion show that the mass fractions are approx. 20% and the domain size about 3.6 nm (36 Angstrom). Both change with crystallization and annealing conditions.

A system with some similarities to the intermediate non-crystalline or oriented mobile phase, is the polyethylene chain in the urea-polyethylene inclusion complex. These urea-polyethylene inclusion complexes (UPEC) are discussed by Kashiwabara et al. [31]. The UPEC is an interesting material because a single polyethylene chain is located in a hexagonal canal of urea molecules, and it must be expected that the polyethylene chain can behave differently from the bulk system like solution-grown crystals or material recrystallized from the melt. Their results showed no mobility in bulk polyethylene below 180 K. While the amorphous part develops mobility in the range from 200 to 300 K, the crystalline part remains immobile. The crystalline part develops mobility in the range above 330 K due to the introduction of gauche defects. For extended chain crystals of polyethylene, the situation seems similar to that for bulk polyethylene, though the mobile fraction is smaller than that of bulk polyethylene.

On the other hand, the second moment of d-UPEC (a system with polyethylene in channels of deuterated urea molecules) determined by broad band NMR is completely different from normal polyethylene. The second

moment is smaller than that of solution-grown material or extended chain crystals throughout the temperature range of observation. This means that the polyethylene chain in d-UPEC is much more mobile than in the other two materials which are rigid below 150 K. The observed second moment reaches a maximum value at 295 K and then remains constant at higher temperatures. This constant value is very close to the value calculated for free rotation, 5.94 x $10^{-8}T^2$ [31]. Therefore, the second moment at 125 K was interpreted as reflecting the vibration around the chain axis with an amplitude of 30°; *i.e.* these two features, vibration at low temperature and free rotation at high temperature, are thought to be consistent with the broad band NMR results. The urea-polyethylene inclusion complex may be of use as a model for some of the molecules in the UHMMPE fibers.

2.2.3 Thermal Properties

2.2.3.1 Heat Capacity

Based on the collected data in the ATHAS Data Bank, the heat capacity of polyethylene is well established. A table of the data is available from the ATHAS Data Bank. The calculations of the limiting amorphous and crystalline heat capacities will be discussed in the results section. The heat capacities of polyethylene fibers can however not to be found in the literature, yet the suggestion to measure the heat capacity and the intention to use such data, whenever available, was published by Peterlin and Meinel [32] in 1965.

2.2.3.2 Melting

The isotropization temperature was and still is the origin of some controversy, although extended chain crystals have been grown and the melting temperature of those samples under slow heating conditions [33] in a dilatometer has been determined. The melting of poly(methylene) is extremely sharp with no evidence of premelting up to 410 K.

Polymer crystals of large chain extension exhibit an inherently slow melting that often leads to superheating of larger crystals before fusion is complete [1]. Reorganization and recrystallization as well as relaxation of strained tie molecules may further obscure the melting process. Only well-crystallized, extended-chain crystals of polymers melt slowly enough so that the melting kinetics can be followed *via* microscopy. These experimental methods were, however, limited to heating through conduction from the outside of the crystal and provide no atomistic details of the structural and dynamic changes that occur during melting from the superheated state. A summary of the equilibrium melting data on polyethylene is given by Wunderlich and Czornyj [34].

Polyethylene (PE) and *n*-paraffins form a homologous series of hydrocarbons, and their crystal structures and dynamic properties are related. In addition, the study of paraffins and PE [31,35-39] offers a model for other polymers. A detailed knowledge of dynamic and structural properties of paraffins and PE is thus fundamental to the understanding of the behavior of many systems that contain linear paraffinic sequences, such as biomembranes and micelles, liquid crystals, and mesophases in general. Currently, details of the

dynamics are still not fully understood as they apply to processes such as polymorphic phase transitions, defect formation, and melting.

Thermodynamically, the melting point is the temperature at which there is no difference in free energy between the crystal and the melt. Consequently :

$$\Delta G = \Delta H_m - T_m \Delta S_m = 0 \quad \textbf{(1)}$$

or

$$T_m = \frac{\Delta H_m}{\Delta S_m} \quad \textbf{(2)}$$

where Δ refers to the differences between the states, G is the Gibbs free energy, H is the enthalpy, S is the entropy and T_m is the melting temperature. The subscript m indicates melting. (Table 2.1)

Table 2.1: Melting parameters of polyethylene [1]

T_m°	414.6 K
ΔH	4.11 kJ mol^{-1}
ΔS	9.91 J K^{-1} mol^{-1}

The description of irreversible melting is based on the two-phase model of semicrystalline, linear macromolecules. When permitting defects in the crystalline portions and order in the amorphous portion of the sample, the crystallinity model has been most successful in describing the melting

phenomena. As the samples become less crystalline and the total fraction of molecules involved in interfaces and interphases becomes more significant, a special treatment of the surface region may be necessary [1].

2.2.3.3 Melting of UHMMPE Fibers

The sample preparation for the melting of UHMMPE fibers in a DSC is described by Bastiaansen and Lemstra [40]. They used chopped fibers, 1-2 mm long, and added a few droplets of silicon-oil to improve the heat contact and to allow friction-free shrinkage upon melting.

The onset temperatures of unconstrained melting of UHMMPE fibers were reported as 415 K by Bastiaansen and Lemstra [40]. In the same article, they show DSC experiments of UHMMPE fibers with only one melting peak, while the unconstrained melting as visually observed consists of only one step as well. The unconstrained melting of a macrofiber, submerged in silicon oil inside a glass capillary, as described by Pennings and Zwijnenburg [41] shows only a single step, while their "free shrinkage" melting in DSC shows three and even four peaks.

Many variations exist in the preparation of constrained fiber samples. On one hand, the physical constraints are spools, frames, or clamps holding the fiber. While spools keep the sample in a constant volume and clamps assure constant length, the frames keep some fibers in a constant length environment, (the innermost layer), while the outer layers are in a constant volume environment. Constant length experiments in the thesis work were performed

with a plate of aluminum where the fibers were wound parallel to ensure constant length.

Another form of constant volume melting is achieved by embedding the fiber in an epoxy matrix. The hardening of the matrix by crosslinking results in a rigid environment for the individual fiber. The cavity occupied by the fiber is assumed to be of constant dimensions. With insufficient hardening, where post cure effects are observed during the melting of the UHMMPE fibers, the matrix can however not be assumed to be rigid. A complete cure is therefore the first necessity for such experiments.

Pennings and Zwijnenburg [41] assigned the peaks in constrained melting experiments in the following manner. The unconstrained parts of the sample and lamellar overgrowth on the shish-kebab fibrils correspond to the first melting peak, which occurs at 414 K after extrapolation to zero heating rate. The second peak at 423 K is attributed to the transformation of the orthorhombic into the hexagonal lattice, while the third peak at 468.5 K is assigned to the melting of this hexagonal lattice. Pennings and Zwijnenburg [41] overlook that in their measurements the end of the third melting peak is never higher than 438 K, while the WAXS reflection of the hexagonal phase is still recognizable well above 450 K. This is even observable at the low heating rate of 0.35 K/min. Such discrepancies need to be addressed with full knowledge of the specific manufacturing and measurement parameters. Since all the details are not known to the researchers unless full cooperation with the manufacturer has been established, this has to be done in the future.

The effect of the constraining geometry and fiber diameter on the melting behavior was studied by van Mele and Verdonck [42]. The effect of the epoxy matrix on the melting is attributed to the inability of the fiber to expand laterally on melting, which is possible in the cases of the fiber being wound on a frame or a spool.

The melting temperature as a function of the draw ratio was studied by Kanamoto et al. [43]. Sample sizes of 40 μg show single peaks except for the cases of melting constrained in an epoxy matrix where the sample is constrained to its initial volume and may show interaction between the matrix and the fiber.

All of the experimental findings are done in one specific set of conditions, individually believed to be the best possible condition. It is noteworthy to mention that only the analysis of all different conditions will lead to the answer to the question of the processing-structure-property relationship. In the experimental results presented in this dissertation, the inherent problems of variable sample mass and self generated constraint in a DSC experiment were addressed. This study is the first to investigate the sample mass dependence of the multiple melting peaks in the DSC experiments of UHMMPE fibers. The findings of the study support the model of a nanophase separated multi-phase material in the UHMMPE fibers.

2.2.4 IR/RAMAN

Micro-Raman spectroscopy on deformation of high-modulus, UHMMPE fibers also revealed at least two types of strain in the oriented C-C bonds with *trans*-conformation [44-47], attributed to extended chains in the crystalline and a non-crystalline domain. The differences in the strained bonds are as much as an order of magnitude [45]. The two types of oriented chains are largely parallel to each other. Using different fitting methods and different fiber samples, the mass fraction of the highly strained chains is 18% in one study [45], and 40% in another [47].

Based on IR/Raman studies Kip et al. [46] suggest that the fibers can be described by two crystalline fractions mixed on the molecular level and an additional small amount of a third fraction with a low Young's modulus. It will be shown in this thesis that the mixing cannot occur on a molecular level but that a minimum domain size is required for both the x-ray scattering of the non-crystalline mesophase and the mesophase glass transition.

2.2.5 Mechanical Properties

Polymer fibers with tensile moduli (stiffness) approaching 300 GPa and strengths of up to 4 GPa have been produced and are called high performance fibers. The commercially available fibers produced in the gel-spinning process and analyzed during this thesis typically have a modulus in the order of 100 to 170 GPa and a strength of 3.5 to 3.5 GPa [48].

The alignment of the molecules in the fiber direction creates highly anisotropic materials. Ultra strong PE fibers exhibit, in addition to very high strength and modulus, high-strain-rate effects [9] that are absent in other reinforcing fibers such as aramid, glass, or carbon. Therefore, ultra strong PE fibers are particularly suitable for applications involving the high deformation rates encountered in explosions and ballistic impacts. The reasons for the damage tolerance of the fibers are explained based on their nanoscale structure.

Several structure models have been proposed to interpret the processing-structure-property relationship [49-53]. These fiber structure models have one most frequent feature to reconcile the mechanical properties with the structure, namely that there exist oriented, noncrystalline chains besides the crystalline and amorphous phases. These chains are usually called taut tie molecules (TTM). The TTM concept was introduced to explain mechanical properties of fibers, but it lacks a connection to the molecular level. The TTM mass fraction is then calculated from the mechanical properties. For the initial modulus one can use, for example, the series-parallel model of Takayanagi [50,54,55]. The TTM are usually assumed to be oriented exactly parallel to the fiber axis and are given the crystalline strength and modulus. The concept of TTM's is based on isolated chains. None of the results, presented in the following, can be explained satisfactorily by this concept. Only a phase of significant size can have an x-ray scattering and a mesophase glass transition.

Chapter 3

Thermodynamics and Thermal Analysis

3.1 Thermodynamic Principles

3.1.1 Equilibrium Thermodynamics

A system can be described [56] in terms of its *functions of state*, such as *total energy, U, temperature, T, volume, V, pressure, P, number of moles, N,* and *mass, M.* The functions of state can be divided into two classes, extensive and intensive. *Extensive functions of state* are proportional to the amount of matter (such as *U, V, N, and M)*, and *intensive functions of state* do not change with changing amount of matter (*T, P)*. If the system is in equilibrium, the interrelations between the functions of state are given in equilibrium thermodynamics. The basis of equilibrium thermodynamics is given in three experimental laws, the laws of thermodynamics. The first law will be discussed in the following. The second law states that, "in an isolated system, spontaneous processes occur in the direction of increasing entropy," and according to the third law "all perfect crystals have zero entropy at absolute zero."

The first law of thermodynamics describes the fact that energy is conserved in all experiments. In other words, the total energy, *U*, of a system in

equilibrium is a function of state, and its value is fixed for a given set of variables of state. For a change of U one can write:

$$dU = \delta Q + \delta w \qquad (1)$$

where Q and w represent the two forms of energy, *heat* and *work*, respectively. The symbols δ are to indicate that although dU is independent of the path, δQ and δw are not. Furthermore, one can always write for a function of state that its change is given by

$$dU = (\partial U/\partial T)_{V,N} dT + (\partial U/\partial V)_{T,N} dV + (\partial U/\partial N)_{T,V} dN + \ldots \qquad (2)$$

The change dU is the sum over all partial changes. The subscripts indicate the variables that are being kept constant. If additional variables are necessary, the equation must be expanded. The first partial differential coefficient on the right, (dU/dT)V, N is given the name *heat capacity at constant volume.* It cannot be easily determined by differential scanning calorimetry, since the condition of constant volume is experimentally impossible in a DSC experiment.

3.1.2 Calorimetry

The central function of state of calorimetry without chemical or phase changes is the *heat capacity.* It is the heat absorbed by a system (which is assumed to be close to constant in composition) on raising the temperature by 1 K:

$$C = Q/\Delta T \qquad (3)$$

According to equation (1), a closed system can exchange only heat and work. Assuming volume work, $-P\,dV$, as the only possible work, makes both right hand terms in Eq. (1) functions of state.

$$dU = dQ - PdV \tag{4}$$

Combining Eqs. (2) and (4), one obtains:

$$dQ = (\partial U/\partial T)_{V,N}\,dT + [(\partial U/\partial V)_{V,N} + P]dV \tag{5}$$

Measuring the heat capacity at constant volume, $dV = 0$, leads to a simple correlation of the measured quantity dQ/dT and the change in internal energy:

$$dQ/dT = (\partial U/\partial T)_{V,N} \equiv C_V \tag{6}$$

Unfortunately, this type of measurement is quite impossible for condensed matter because of the large thermal pressure coefficients.

The description of thermal analysis is greatly simplified by thermodynamic functions that can be used at constant (atmospheric) pressure. The internal energy, U, is not such a function. Expressing U as a function of the independent variables P and T, instead of V and T (assuming again a closed system of constant composition), one obtains:

$$dU = (\partial U/\partial T)_{P,N}\,dT + (\partial U/\partial P)_{T,N}\,dP \tag{7}$$

an equation similar to Eq. (2). The combination of Eqs. (6) and (7), needed for an expression of dQ must now, however, take into account that dV is dependent on changes in pressure, Eq. (8).

$$dV = (\partial V/\partial T)_P \, dT + (\partial V/\partial P)_T \, dP \tag{8}$$

Combining all these equations leads to:

$$dQ = \left[\left(\frac{\partial U}{\partial T}\right)_{P,N} + P\left(\frac{\partial V}{\partial T}\right)_{P,N}\right]dT + \left[\left(\frac{\partial U}{\partial P}\right)_{T,N} + P\left(\frac{\partial V}{\partial P}\right)_{T,N}\right]dP \tag{9}$$

and at constant pressure:

$$\frac{dQ}{dT} = \left(\frac{\partial U}{\partial T}\right)_{P,N} + P\left(\frac{\partial V}{\partial T}\right)_{P,N} \tag{10}$$

Eq. (10) states that at constant pressure, the heat capacity dQ/dT is not sufficient to measure U. The change of V must also be known.

Introducing a new function of state, the *enthalpy*:

$$H \equiv U + PV \tag{11}$$

simplifies matters considerably. In the case of tensile extensions work, it is convenient to define enthalpy as $H \equiv U + PV + f\,l$, where f is force and l equals the length. Since H is made up of other functions of state, it must itself be a function of state. Enthalpy is the internal energy to which one adds the work for expansion at experimental pressure from volume zero to the actual volume of the

system. For the condensed state, the system volume is small. Accordingly, the difference between H and U is small, and H is still an approximate measure of U. The simplification becomes clear on insertion of Eq. (11) into Eq. (10):

$$\frac{dQ}{dT} = \left(\frac{\partial H}{\partial T}\right)_{P,N} - \left(\frac{\partial PV}{\partial T}\right)_{P,N} + P\left(\frac{\partial V}{\partial T}\right)_{P,N} \qquad H \equiv U + PV \qquad \textbf{(12)}$$

Since the last two terms in Eq. (12) are equal at constant P:

$$\frac{dQ}{dT} = \left(\frac{\partial H}{\partial T}\right)_{P,N} \equiv C_P \qquad \textbf{(13)}$$

The *heat capacity at constant pressure*, C_p, is the calorimetrically measured quantity. It is connected to the *free enthalpy* (Gibbs free energy, or Gibbs function), G:

$$G \equiv H - TS \qquad \textbf{(14)}$$

through the definition of enthalpy, Eq. (13)

$$H(T) = H(T_o) + \int_{T_o}^{T} C_P \, dT \qquad \textbf{(15)}$$

Measurement of heat capacity as a function of temperature also permits the evaluation of entropy. Commonly, the following equation is used for the entropy calculation:

$$S(T) = S(T_o) + \int_{T_o}^{T} \frac{C_P}{T} dT \qquad (16)$$

and equation (14) is used for the free enthalpy calculation. The plot of H, TS and G of polyethylene is shown in Fig. 3.1-1 *. The free enthalpy diagrams are also used to characterize different phase transitions.

3.1.3 Transitions

According to Ehrenfest [57], one can distinguish the phase transition types according to the free enthalpy. On traversing a *first order transition,* the free enthalpy G is a continuous function of the variables *T,* and *P*, but it suffers a change of slope at the transition temperature. Consequently at least one, or both, of the first derivatives of *G* show a discontinuous change on going through the transition.

$$(\partial G / \partial T)_P = -S \qquad \text{or} \qquad (\partial G / \partial P)_T = V \qquad (17)$$

The main example of a first order transition is the melting transition. It can be defined as the intersection of the free enthalpies G_a and G_b (Fig. 3.1-2). The systems corresponding to the branches of higher free enthalpy lose their stability at T_m, the melting temperature. Only at T_m, both phases coexist in equilibrium, so

---

* All figures may be found in Appendix A; all tables may be found in Appendix B.

that ΔG, the change in free enthalpy is zero and the equilibrium melting temperature becomes:

$$T_m = \Delta H_f / \Delta S_f \qquad \textbf{(18)}$$

where ΔH_f is the *heat of fusion* and ΔS_f is the *entropy of fusion.*

For a second order transition, both G and the first derivatives are continuous functions of T and P. But, at least one of the first derivatives has a break at the transition temperature. Accordingly, discontinuities appear in the second derivation of G, *i.e.* in the heat capacity, C_p, thermal expansivity, α, and/or in β, the isothermal compressibility:

$$(\partial^2 G / \partial T^2) = -C_P / T \qquad [\partial^2 G / (\partial P \partial T)] = V\alpha \qquad [\partial^2 G / (\partial P^2)] = -V\beta \qquad \textbf{(19)}$$

Note that on both sides of the transition, phase b is the phase with the lower free enthalpy, *i.e.,* the more stable phase. Thus, a second-order transition is possible only if the continuations of phases a and b, beyond the transition temperature, are not physically realizable states.

3.2 Differential Scanning Calorimetry

A brief review of standard DSC experiments with a listing of all the assumptions is presented. The development of the standard DSC technique towards Alternating Heating Rate DSC (ADSC), and the benefit for the measurement of fiber heat capacities conclude this section.

3.2.1 Review of Standard DSC

For the understanding of DSC, the principle on which it is based needs to be known. Figure 3.2-1 shows the set-up of a DSC cell and indicates the locations at which the temperatures of Block (T_b), Sample (T_s) and Reference (T_r) are determined.

In Figure 3.2-2, the profiles of the three temperatures are presented as a function of time. The relation between the temperature profile and the heat capacity is possible with the calculations as indicated in figure 3.2-3.

The Figures 3.2-4 and 3.2-5 show the temperature profiles through a first order transition. The heating diagram (Figure 3.2-4) shows that as long as the substance has not completely gone through the phase transition, the temperature of the sample stays constant. This is a direct consequence of the phase rule. On cooling (Figure 3.2-5), this rule should hold true as well. However, only samples without supercooling display ideal symmetrical behavior with constant temperature throughout the transition. Depending on the degree of supercooling, the cooling rate, the crystallization kinetics, and a variety of other factors, the temperature profile follows the dotted or dashed lines. Both heating and cooling curves with their respective temperature difference signals are presented in Figure 3.2-6. The temperature difference signal is transformed into a heat flow signal, dQ/dt, using Newton's law of cooling . With proper calibration, it can be used to calculate heat capacity. For the calculation of heat capacity, the instrument has to be calibrated for temperature deviations, theoretical onset

slope, and "zero mass difference heat flow". This "zero mass difference heat flow" (also called baseline) is a measure for the imbalance of the DSC cell. Only after these calibrations is the heat flow signal proportional to heat capacity. The proportionality factor is determined by measuring a standard material of known heat capacity. Sapphire is most often used for this purpose.

The heat capacity, C_p, based on a standard heat-conduction DSC as shown in Figure 3.2-1 under linear heating or cooling conditions is expressed as follows :

$$C_p = K\Delta T/q + [(C_p' + K\Delta T/q)(d\Delta T/d T_s)] \quad \textbf{(20)}$$

where ΔT is the temperature difference between reference and sample, K is a temperature-dependent constant (determined by heat capacity comparison with a calibration standard like sapphire), and C_p' is the heat capacity of the empty reference pan (equal weight reference and sample pans). The term in brackets is small for C_p measurement (about 1%) and often omitted. The heat capacity is then only approximately proportional to the temperature difference between sample and reference or heat flow measured by DSC:

$$C_p = K\Delta T/q = K'\Delta HF/q \quad \textbf{(21)}$$

3.2.2 Alternating Heating Rate DSC

The measurement of heat capacity depends on a number of factors, such as establishment of a steady state, negligible thermal gradients within the sample, and different calibrations for measurements on heating and on cooling. Due to this, only limited attempts have been made to measure heat capacity on heating and on cooling.

To avoid difficulties assigning the different potential features in the measurement of the heat capacity of fibers, a method was developed which involved measurement of heat capacity both on heating and on cooling. This method was chosen after extensive experimentation with a new Temperature Modulated DSC (TMDSC) technique. The results of these experiments have been published and the abstracts of these papers are collected in the appendix.

3.2.3 Benefits of the Short Ramp DSC Measurement

Step-wise measurement of heat capacity (C_p) permits the measurement of C_p in short intervals. In this manner, the stability of the baseline does not need to be extrapolated over a large range. The correction for baseline changes (performed by the instrument software for each individual segment) improves the quality of the heat capacity data. Such an improvement was essential for the measurement of the fiber samples.

3.2.4 Procedure

The determination of heat capacity depends on a set of measurement parameters. The following list was developed in the ATHAS laboratory and is followed in the present research:

- Correct for contributions due to sample pan weight differences. The combination of sample pan and measuring cell asymmetries was studied and presented at an international thermal analysis conference: "Determination of Cell Asymmetry in Temperature Modulated Differential Scanning Calorimetry" submitted for publication J. Thermal Analysis, 1996
- Correct for instrument baseline.

The instrument zero-line is a function of the laboratory environment, power fluctuations, and factors with limited control. The accurate determination of this zero-line is essential for the quality of the heat capacity determination. In the present research, it is taken into account by shortening the time for each heating and cooling segment by inserting the intermediate isotherms into the overall heating and cooling ramp. In this way, the fluctuations of the instrument zero-line are easily detected and accounted for.

- Use the *actual* heating or cooling rate for the heat capacity calculation.

The differences between the indicated heating rates to the actual sample heating rates are minimal for the case of slow transitions. For the heat capacity measurements in the present research this condition was fulfilled.

- Calculate the calibration constant for each data point using NIST sapphire standard values or an operator-selected reference material.

The calibration with the sapphire was performed with the exact same heating and cooling profile, and each point was individually corrected on heating as well as on cooling.

- Calculate the heat capacity at each temperature.

With the determination of the heat capacity calibration constant at each point this condition is fulfilled.

3.3 General Scheme of Classification of Materials and Transitions

The properties of most materials change drastically at their phase transitions. A general scheme for the condensed phases and the intermediate, mesophases has been presented by Wunderlich and Grebowicz [58]. The basis of the discussion was the operational definition of solids and liquids: "A solid is defined as either a crystal or a glass, which changes at its melting or glass transition temperature to a liquid." The glass is an amorphous solid, metastable relative to

the crystalline state. Both the melting transition T_m and the glass transition T_g are easily detected by thermal analysis.

In mesophases, order is in between the perfection found in crystals and the disorder typical for liquids and glasses. To classify the mesophases it is useful to subdivide the order gained by a crystal on fusion in three categories: *positional, orientational,* and *conformational.* If on fusion these types of disorder are not gained in one step, mesophases result. For materials with special molecular properties, mesophases (such as liquid crystals, plastic crystals and condis crystals) can exist.

The glass transition separates corresponding solid and mobile states of a given amount of disorder. In solids, small-amplitude vibrations are the dominant thermal motion. In the mobile states, additional large-amplitude motion, such as translation, rotation, and internal rotation (conformational motion) cause the typical macroscopic properties. Figure 3.3-1 shows a schematic of the basic condensed phases [58]. Between the melt (liquid) and the crystal, three mesophases are located. The liquid crystal is distinguished from the liquid by some orientational order (and reduced rotational motion) due to the presence of rod-, board-, or disc-like mesogens [59]. The plastic crystal shows long-range crystalline order, but orientational motion (rotation) is possible within the crystal, due to a close-to-spherical shape of the molecules [60]. Conformationally disordered crystals (condis crystals) have some or complete conformational disorder and mobility but long-range orientational and positional order [13]. The crystals, melt, and the mesophases are linked by first-order transitions during

which they change their order and mobility, as indicated on the right side of Figure 3.3-1. Also shown are typical entropies connected with the various types of order.

Besides the crystalline state, there are four glassy solids indicated. Each glass is linked to the corresponding mobile phase through a glass transition, as shown on the left side of Figure 3.3-1. Each fully mobile part of the molecule (bead) contributes the indicated change to the heat capacity at the glass transition. The basic glass transition has been known for many years [61]. It is seen on vitrification of a liquid that is unable to crystallize for kinetic or structural reasons. As is indicated in Fig. 3.3-1, mesophases may also show glass transitions because they carry out some large-amplitude motion. These and other glass transitions of partially ordered materials were also reviewed recently [62]. The first observation of glasses of liquid crystals is credited to Vorlaender [63]. Considerable progress in the understanding of glass transitions of the mesophase crystals was achieved by Suga and Seki, who calorimetrically analyzed the glass transitions in several liquid crystals with rod-like mesogens, such as cholesteryl hydrogen phthalate [64] and N-(*o*-hydroxy-*p*-methoxybenzylidine)-*p*-butylaniline [65] and disc-like benzene hexa-*n*-alkanoate mesogens [66-68], as well as plastic crystals, such as cyclohexanol, cyclohexene, and 2,3-dimethyl butane [69-72]. The glass transitions in condis crystals were reviewed in Ref. [13].

A simplified classification scheme with only one mesophase is presented in Fig. 3.3-2. The solid phases, crystal, mesophase glass, and glass, are shown

on the bottom of the graph in order of decreasing thermodynamic stability. The transitions, indicated on the left side, have an associated heat of transition and therefore a step change in entropy. The glass transitions of mesophase and the amorphous glass, indicated on the right hand side, show only a step increase in the heat capacity. Both the glass transition and the enthalpy of isotropization are detectable with thermal analysis methods, as will be shown in Chapter 5.

It will be shown in the following that the results of this thesis are consistent with the existence of a conformationally disordered mesophase in the UHMMPE fibers. The existence of this mesophase and the nano-phase structure of crystalline, mesophase and glassy fractions are responsible for the special properties of these fibers.

3.3.1 Application to Fibers

The nomenclature developed previously on PET fibers [15,17] is used in this thesis. The *crystalline* phase has long-range, three-dimensional ordering. The structure, and morphology of the crystal is derived from the full-pattern x-ray diffraction refinement method. There may be more than one polymorph contributing to the crystalline phase. In PE fibers, for example, the crystalline phase may consist of orthorhombic and monoclinic (formerly called triclinic) crystals. All material not contributing to the crystalline diffraction is considered *noncrystalline*. The mesophase can however produce a distinctly anisotropic diffraction pattern in the cases where the mesophase domains are of adequate size. If the noncrystalline material is liquid- or glass-like, a two-phase model with

an *amorphous* and a crystalline phase is sufficient to describe the structure-insensitive properties of the fiber (such as density, modulus, and thermal properties). If the noncrystalline material shows additional anisotropic scattering, one or more *intermediate* phases are present and needed to model the fiber. The polymer chains of the intermediate phases have a certain degree of orientation parallel to the fiber axis but have no long-range crystal ordering, particularly at right angles to the fiber axis. The chain segments surrounding the crystals with strained connections to them are thought to be an important part of the intermediate phase [9].

In this connection, the term *phase* must be understood as microphases, since typical crystalline and amorphous phases in semicrystalline polymers are less than one micrometer in dimension. The smallest crystals, intermediate and amorphous areas, may even be nanophases, *i.e.* of the order of one nanometer in size. Such small phase areas are not only influenced by surfaces and interfaces, as microphases are but also experience interactions between opposing surfaces. The presence of such small phase areas makes it difficult to find a simple model for the fiber description [73].

The multiple phases just described coexist in the one-component PE fibers at various mass fractions over a wide temperature and pressure range (two degrees of freedom). This can only be true if the fibers are not in equilibrium (*i.e.* are metastable). In equilibrium, the phase rule forbids more than one condensed phase outside the transition regions:

(permitted # of phases, P) = (# of components, C) - (# of degrees of freedom, F) + 2

It is experimentally well established that the properties of oriented semicrystalline polymers depend both on crystallinity and on the arrangement of the chains in the noncrystalline part. This is particularly valid for fibers. It will be shown that the properties of polymer fibers cannot be explained unless one admits the existence of two noncrystalline kinds of domains that differ in density and orientation. In the three-phase model, besides a crystalline and a mobile amorphous phase, there is a third phase, variously called oriented, anisotropic, mesomorphic, intermediate, third fraction, or rigid amorphous phase. These three phases exist in the semicrystalline polymer in bulk, in fiber, as well as in film. Experiments with different instruments have in the past been interpreted to show either high-temperature relaxations between T_g and T_m, two glass transitions, or more than one average interchain distance in the fiber samples. The relevant references have been presented in Chapter 2.

While fusion is an endothermic transition with an increase in disorder (entropy) and may occur in more than one process, glasses undergo the solid-liquid transition at the glass transition temperature without change in enthalpy and entropy [56]. Studying the increase in heat capacity at the glass transition, it was found empirically to be a materials constant of about 11 J/(K mol) for each mole of mobile part in the molecule (bead or bond) [56]. Applying this concept to semicrystalline polymers revealed that some of the amorphous glass, most likely the part closely attached to the crystal surface, may not become mobile at the

observed glass transition temperature. The measured change in heat capacity at the glass transition is less than expected from a fully amorphous sample reduced by the fraction of crystallinity. This deficit was ascribed to a *rigid amorphous fraction.*

* * * * * * * * *

In many cases thermal analysis is able to decide quickly between the various types of mesophases, and for many samples, the rigid amorphous fraction can at present only be quantitatively identified by thermal analysis.

Chapter 4

Experimental

4.1 Samples

4.1.1 Fiber Samples

This study included a total of five drawn PE fiber samples. All of these were UHMMPE fibers and were provided by Allied-Signal Inc., all with similarly high molar masses ($M_r > 10^6$). Three of them (PE-I, PE-IV and PE-VI) are research samples which were made from the same polymer. Different processing conditions make these two fibers have different properties. All available mechanical properties are listed in Table 4.1-1. The others are commercial Spectra 2000 and 900 fibers (PE-II and PE-III, respectively). Unfortunately details of the processing history were not available to us. PE VI was obtained as a sample from Dr. Bhat (University of Tennessee, Textiles Department). It is a research sample from Allied-Signal Inc. According to information from Dr. S. Kavesh, of Allied-Signal Inc., it is not hot stretched but otherwise identical to PE-I, II and III. This makes PE-IV and PE-VI have very similar properties. All fibers were prepared by gel-spinning [8,74,75].

4.1.2 Temperature Calibration Samples

The samples for the temperature calibration of the DSC were acetone (T_m = 177.9 K), cyclohexane (T_d = 186.1 K, T_m = 279.7 K), cycloheptane (T_d =134.8 K, T_m = 265.1 K), cyclooctane (T_d = 166.5 K, T_m = 288.0 K), 1-chlorobutane (T_m = 150.1 K), 2-chlorobutane (T_m = 141.9 K), *n*-octane (T_m = 216.4 K), naphthalene (T_m = 353.4 K), indium (T_m = 429.8 K), tin (T_m = 505.1 K), KNO_3 (T_m = 607 K), and tin (K). All of the samples were used over an extended period in the ATHAS laboratories and have different origins.

4.1.3 Heat Capacity and Heat of Transition Calibration Samples

The heat capacity calibration was performed using sapphire as standard materials. The sapphire (Al2O3) is traceable to the NIST (former NBS) heat capacity standard material [76,77]. The temperature program was identical for all measurements, including the empty pan measurement and the sapphire calibration run.

The calibration of the heat of transition [78-80] was done with indium as a standard. The sample was obtained from the instrument manufacturer. Its enthalpy of transition is 28.45 J/g [56].

4.1.4 Sample Preparation

All mass determinations were carried out on a Cahn C-33 electrobalance with a sensitivity of 1 μg and an overall accuracy of ±0.001% of the overall load. Special care was taken to match the sample pans on all the measurements while leaving the same pan on the reference position. The sample pans for all the heat capacity determination measurements weighed 49.050 +/- 0.020 mg.

4.1.4.1 Cut Fibers

Either the fibers were encapsulated in a 40 μL standard aluminum crucible without a center pin and with the cover lid cold welded, or the fibers were placed in an open pan for ease of visual observation of the appearance after melting. In separate experiments, fiber samples were embedded in anhydrous aluminum oxide for enhanced thermal conductivity. Sample masses varied from 24 μg to 4 mg. The reference pan was identical for all measurements. The optimal arrangement was obtained when each fiber made direct contact with the bottom of the pan. This requires sample preparation under the microscope and leads to much smaller masses that range from 0.02 to 0.10 mg.

The cut fibers were prepared in the following manner. The fiber strands were unrolled and taped to a cutting board. Three pieces of approximately 15 cm length were cut and put into a confined space inside a doubly folded weighing paper. This weighing paper and the fibers inside were then cut into about 3 mm wide pieces with a single-edged razor. The fibers were transferred to the DSC pan with the help of the weighing paper. This procedure had the benefit of

avoiding the need to touch the individual fibers with the tweezers. This leaves the fibers largely parallel, which allowed, in turn, maximum sample masses with cut fibers. The maximum mass for cut fibers, depending on the individual fiber properties, was about 8 mg.

4.1.4.2 Fibers on a Spool

In order to achieve maximum sample size for heat capacity measurements, the fibers were wound onto a spool as shown in Fig. 4.1-1. The assembly consisted of a *bottom part* (A) into which the *central rod* (B) (diameter 1.0 mm) was fixed with a *set screw* (C). The other parts from bottom to top are: washer (D), sample (E), pierced sample pan (F) and top part (G) with another set screw (C). For a uniform sample height, the distance between the bottom and the top was adjusted with the help of two DSC sample pans. The *pierced sample pan* in the assembly assured a uniform sample diameter. The *washer at the bottom* was used to push the finished sample off of the *central rod.*

The preparation of the sample involved the assembling of the spool to the desired specifications and the winding of the fibers onto the spool with as small a force as possible to achieve tight winding. Both ends were tied into a knot before loosening the set screw and pushing the sample off of the central rod with the washer. The sample of 5mm diameter and 2 mm thickness, was immediately put into a precisely weighed DSC sample pan to avoid the unraveling of the sample and sealed with a lid. The maximum achievable sample mass, depending on the individual fiber properties, is in the order of 16 to 30 mg.

4.1.4.3 Fibers on an Aluminum Frame

The preparation of a sample for measurement with constant length involved the use of a piece of aluminum which was produced from a DSC pan-cover. The approximate dimensions were 3.5 x 5.0 x 0.25 mm. A single fiber was carefully wound onto this frame to keep the fibers parallel and possibly fully extended without putting too much stress onto the fiber in the process. The ends were tied to a knot and the loose ends cut off with a knife. The final frame-fiber assembly was put into a standard DSC pan. In order to check for the temperature gradients within the sample pan, a piece of indium was put on top of the metal frame. No difference in melting temperature of indium was observed.

4.2 DSC Instrumentation

A commercially available Mettler-Toledo DSC820 module, equipped with a ceramic sensor and sample changer, was used in the research. Dry nitrogen gas with a flow rate of 10 mL/min was purged through the cell. The gas flow rate was monitored and adjusted with a gas controller. The error in the heat capacity calculation is estimated to be <1% above 300 K and <3% below 200 K and <2% between 200 and 300 K. All heat capacities were measured at 10 K/min heating rate. All sample placement was done with the autosampler for increased repeat-ability.

4.2.1 Calibrations

The instrument needed to be calibrated for the different modes. All the parameters which needed to be calibrated for are:

A: temperature calibration and heating rate dependence of the calibration

Both the temperature and the lag calibration were performed with the procedure recommended by the manufacturer. The different samples are measured with different heating rate, and the linear dependence of the onset is used to correct according to the heating rate of the individual experiment. The slight mass dependence of the lag calibration did not have any significant effects on the presented measurements. The onset of melting was determined by the extrapolation of the melting peak to the baseline. The end of the melting peak is defined by the extrapolation of the high-temperature side of the peak to the baseline. The instrument software carried out the correction of the temperature signal automatically which permitted an unlimited amount of transitions for the calibration. A periodic check, before and after a measurement series, revealed no significant deviations of the temperature calibration (less than ±0.1 K) [79,81-87].

B: heat flow (transition) calibration

The heat flow calibration for sharp transitions was performed with a standard indium sample.

C: cell asymmetry calibration

The effects of cell asymmetry, as discussed in [88], had no effect on the measurements of the heat capacity of UHMMPE fibers because they were measured with standard DSC techniques.

D: heat capacity calibration as a function of heating rate.

The heat capacity calibration as a function of the heating rate was performed automatically by using the same heating and a cooling segments for the sample, empty pan, and sapphire measurements.

4.2.2 Heat Capacity Measurement

For the heat capacity determination, the range from 173 to 403 K was used in order to avoid problems associated with shrinkage in the calorimeter pan. The temperature profile and the resulting heat flow for one of the fiber spool samples is shown in Fig. 4.2-1. The measurement started at 173 K with an isotherm of 5 minutes. During this time, the instrument and sample equilibrated and the initial isothermal heat flow could be established. The temperature range from the start temperature to the end temperature at 393 K was subdivided into 20 K steps. Each of the steps was measured with a heating rate of 10 K/min. The time for equilibration at each isothermal temperature was one minute. The first heating ramp started at 173 K and ended at 393 K. The isotherm at this temperature was 5 minutes. In the following overall cooling ramp, the same isothermal temperatures were used to establish the baseline of the measurement. The second overall heating ramp was started from 183 K. In this way, the approach

to the steady state of the individual segments shifted from the first to the second overall heating ramp. The second overall cooling segment concluded the experiment.

The sample, empty pan, and sapphire measurements were performed with this temperature program. The heat capacity calibration was performed with sapphire standards. Special care was taken to match the sample pans on all the measurements while leaving the same pan on the reference position. The sample pans for all the heat capacity determination measurements weighed 49.050 +/- 0.020 mg.

4.2.3 Heat Capacity Calculation

For the calculation of the heat capacities, the empty pan measurement was subtracted from both the sapphire and the sample measurement. The instrument software was then used to calculate the heat capacities. For the calculation of averages, standard deviations, and standard error, the data was exported as ASCII files to SigmaPlot.

4.3 TMA

Thermal mechanical properties of PET fibers were measured with a TA Instruments 943 Thermomechanical Analyzer with a fiber-tension accessory which is designed to examine dimension changes of fibers under tension. The fiber was attached to a probe with two crimped aluminum balls on the ends of the fiber.

Unless indicated, a minimum weight of 50 mg was applied on single fibers to monitor the shrinking or expansion. The dimensions were calibrated with aluminum. The temperature was calibrated with the phase transition of indium. The heating rates were 10 K/min.

The shrinkage at a given temperature or time is calculated based on the following equation:

$$S(\%) = 100 \times (1 - l/l_0) \quad (1)$$

where S is the shrinkage in percent, l_0 is the fiber length at the beginning and l is the length at given temperature or time. Note here $S > 0$ is shrinking and $S < 0$ is expansion.

4.4 Microscopy

The shrinkage behavior was also examined by heating the unconstrained fibers on a hot-stage under a polarizing stereo microscope of the type Olympus SZH, equipped with a coaxial vertical illumination, Intralux® 6000 VOLPI, and operated at a magnification of 20–60×. The dimensions of the sample were observed by video, photography, and the naked eye.

4.5 NMR

The solid state NMR work was performed in cooperation with Dr. W. Chen of our laboratory.

The solid state ^{13}C NMR spectra were measured with a Nicolet NT-200 NMR spectrometer equipped with a Doty Scientific magic-angle spinning (MAS) probe, operating at 50.31MHz and 200.07MHz for ^{13}C and ^{1}H, respectively. Temperature control was obtained using the standard Nicolet controller. Rotors (cylindrical sample container, 5 mm in diameter) were supplied by Doty Scientific and machined from single crystals of Al_2O_3 (sapphire). The end caps used for the rotor were made from brown plastic Vespel® (Registered trademark for a DuPont polyimide). The sample was rotated with nitrogen gas at 4.5 kHz at the magic angle. Prior to each measurement, probe tuning and matching are performed to minimize the reflected radio frequency power.

The conventional one-pulse of ^{13}C with two-level decoupling of protons (BILEV) was performed primarily to obtain the spectra of the mobile molecules, such as that in the isotropic melt and in the amorphous fraction above the glass transition temperature. The pulse width used for ^{13}C was 3.9 μs, corresponding to an 80° flip angle. The recycle delay between two successive pulse sequences was 1 s. These conditions ensure the elimination of resonances from rigid carbon atoms in the well-ordered region having long spin-lattice relaxation times (T_1). Carbon atoms in the *oriented mobile component*, having intermediate mobility, may well become detectable because their spin-lattice relaxation times fall into the order of seconds. The distinction between a liquid-like amorphous and the oriented mobile component in our case can be made by the difference of their chemical shifts and the measurements of spin-lattice relaxation times described in the following.

The ^{13}C spectra of the rigid materials, including those of the oriented mobile component, were obtained using the methods of cross-polarization, high-power proton decoupling, and magic-angle sample spinning (CP-MAS). The signals from the liquid-like amorphous phase will be, in this case, suppressed because the dipolar interaction between protons and carbons is diminished by the fast molecular motion so that no cross-polarization can occur. The CP-MAS experimental parameters were as follows: contact time, 2.0 ms; proton 90° pulse, 5.1 μs; recycle time 3 s; number of transients, 500.

A dephasing experiment at room temperature allowed the measurement of the crystallinities [89]. The dipolar-dephasing pulse sequence was changed from standard CP-MAS to suppress the signals from the more rigid carbons that have strong dipolar coupling with nearby protons. The change involves the insertion of a dephasing delay, τ, following C-H cross-polarization, and prior to signal acquisition (when τ = 0 μs, the dephasing experiment is identical to the standard CP-MAS) [104].

The spin-lattice relaxation times (T_1) were measured at room temperature by using magic-angle spinning and high-power proton decoupling. Both the inversion-recovery (IR) and progressive saturation (PS) methods [90] were carried out. Delay times of 0.1 to 45 s were used. The number of transients was typically 400. Proton saturation was applied during the variable delay time. The ^{13}C 90° and 180° flip angles occur at 4.1 and 8.2 μs, respectively. The recycle time of IR was 10 s. The spectra for relaxation measurements were obtained by

repeatedly cycling through the different delay times, each time adding in a few free induction decays. This method of experiment interleaving eliminates possible errors from long-term changes, such as spinner instability, amplifier drop, *etc.* When plots of the data can be represented by a single exponential, the T_1 values were taken from a least-squares fit. In general, T_1 decreases with increasing temperature. Thus, one expects the crystalline ^{13}C to have the longest T_1, such as 1,000 s; ^{13}C in mesophases as represented by condis, plastic, and liquid crystals have intermediate values for T_1, ranging from 1 to 20 s; and ^{13}C in liquids have a T_1 between 10^1 and 10^3 ms. In the liquid state, in contrast to the solid state, T_1 increases with increasing temperature or mobility (extreme narrowing condition). The difference in T_1 can thus help to assess the nature of the different phases.

In addition, the proton spin-diffusion experiment was carried out to estimate the domain size of the crystalline and the oriented mobile components. A double resonance extension of the Goldman-Shen pulse sequence was used [91,92], and the homonuclear proton dipolar dephasing time was chosen to be 35 μs, which is long enough to eliminate the magnetization of the ^{13}C spins in the ordered domains. The variable spin-diffusion time ranges from 10 μs to 1.5 s.

The ^{13}C chemical-shift reference was set using hexamethylbenzene (17.36 ppm for the methyl carbon relative to tetramethylsilane) prior to the experiment. The field drifting of the spectrometer was estimated to be less than 0.05 ppm during an experiment.

Cross-polarization, high-power proton decoupling, and magic-angle spinning (CP-MAS) were applied to determine the mass fractions of the components of the fibers. Temperature-dependent NMR experiments were carried out on PE-I to observe the changes in morphology. The standard deviation of the temperature controller is about 2 K. The mobility of the carbon atoms was determined by measuring of the spin-lattice relaxation times (T_1). A proton spin-diffusion experiment was carried out to estimate the domain size of the crystalline and the oriented mobile components.

4.6 X-ray

4.6.1 Full Pattern Wide Angle X-ray Diffraction

The full-pattern wide angle X-ray studies were done in cooperation with Dr. Y. Fu of our laboratory at the Oak Ridge National Laboratory.

The four samples, PE-I-IV, were included in the structure analysis by full-pattern x-ray diffraction. The data on sample PE-I were already collected in the previous study [23] and are included in the present study for reinterpretation. The data collection was carried out in the $\omega/2\theta$ mode, described earlier [23]. Individual fibers were glued with a dilute Collodion solution to form bundles with diameters of 0.8-1.0 mm. The sample bundles were mounted on a Huber four-circle diffractometer and aligned with the fiber axis along the diffractometer ϕ axis (meridian). The x-rays employed were Mo K_α, made monochromatic with a

graphite monochromator. A square counter aperture of 4.0 mm width was located 28 cm from the sample. All data were collected at room temperature.

For PE-II and PE-III, a total of 50 scans were made parallel to the 00ℓ layer lines, eleven centered on each layer (in steps of 0.0785 nm^{-1} in reciprocal space). For each scan, individual counts were measured for 48 seconds at steps of 0.05 nm^{-1}. The limit of data collection was $2° \leq 2\theta \leq 86°$. Every 80 counts a count was made at a reference position to verify that the beam intensity had not varied significantly. For sample PE-IV, a total of 78 scans were made parallel to the 00ℓ layer line, at steps of 0.02 nm^{-1} in reciprocal space, centered on each layer.

The full-pattern refinement was based on an orthorhombic crystal structure model, *i.e.* there is only one equivalent position for each atom in the asymmetric unit of the crystal. The crystal structure and morphology of these four fiber samples were determined by full-pattern refinement, using the program FIBLS that was written by Busing [23]. FIBLS uses as its observations the counts measured at specified positions in two-dimensional reciprocal space corresponding to a particular setting of the diffractometer. Usually these observations are grouped into scans made either parallel to the layer lines or parallel to the fiber-axis or meridional direction. Variables can be categorized as those which primarily affect the peak positions, the peak shapes, or the peak intensities. Peak positions depend on the crystal lattice parameters and on the fiber-axis direction vector. A model of the structure of the crystallites is first used to calculate a three-dimensional diffraction pattern. The three-dimensional,

calculated diffraction pattern is then rotated to produce a two-dimensional, calculated diffraction pattern which is compared to the two-dimensional, observed fiber diffraction pattern at each point of the data collection.

The structure model chosen includes parameters which define the morphology and the crystal structure of the crystallites. The full complement of fitting parameters used in the refinement is the average size of the crystallites in three dimensions, the distribution of disorientation of the crystallites relative to each other (the mosaic distribution), the average orientation of the crystallites with respect to the fiber axis, a scale factor, the unit-cell parameters, the atomic positions (usually determined using a rigid body model), a temperature factor, a paracrystallinity matrix for the defects, and the parameters of the diffractometer.

The crystalline diffraction was separated as outlined in the introduction from the noncrystalline background-scattering using the iterative Fourier filter method [15]. The computer program FIBLS (written by Busing [23]) was employed for the full-pattern refinement of the crystallite structure. The procedure of the refinement was similar to that described in the previous paper [15]. The variables include parameters of the crystal unit-cell, tilting angle, anisotropic crystallite size, disorientation, and paracrystallinity. A constrained molecular structure model was employed in the refinement. The bond lengths were fixed at the corresponding values of similar, small molecular compounds. The results of the crystal structure analyses are summarized in Table 4.4-1.

Peak shapes are determined by anisotropic particle size parameters and by the fiber mosaic spread or disorientation that measures the width of the

distribution of crystallite orientations from the fiber axis. Paracrystallinity parameters cause the peaks to broaden anisotropically as a function of their axial or radial distance from the origin. The width of the observed peaks may also depend on the size of the counter aperture. All these parameters were fitted in the first step of the crystal structure determination and the back-calculation of the crystalline diffraction pattern.

An iterative Fourier-filter method separates the crystal diffraction from the noncrystalline scattering. The background scattering needs to be removed before the fitting of the crystalline pattern. This removal of the background scattering is based on the characteristics of the scattering. The background scattering, due to mesophase and amorphous material, has less sharp peaks. The Fourier transforms of the background and the crystalline diffraction peak scattering are therefore significantly different to allow for the separation.

Overall the procedure of full-pattern refinement was similar to that described earlier [15,23]. The distortions of the first kind and paracrystallinity effects (distortions of the second kind) [93] are included in the fit of the two-dimensional profile of the diffraction peaks [15].

4.6.2 Powder X-ray Diffraction

Powder x-ray diffraction measurements were done on a Scintag PAD-X diffractometer, using nickel-filtered Cu K_α radiation (λ = 0.15406 nm) operating at 45 kV and 40 mA. These experiments were done in cooperation with Dr. A. Habenschuss at the Oak Ridge National Laboratory (ORNL). The diffractometer

was equipped with Soller slits in both incident and reflected beam. Data were collected between 2θ range of 16–28°, in step of 0.1 degrees and at a scanning rate of 10 seconds per point.

Powder x-ray diffraction as a function of temperature was measured with the PE-I fibers, cut into short pieces (millimeter sizes). The short fibers were then packed into an aluminum sample container (20×12×1 mm) with a beryllium cover to provide a flat sample surface for reflection geometry. The container was mounted on a sample stage consisting of a tantalum heating strip (Bühler high temperature chamber). Temperature was recorded by a Chromel-Alumel thermocouple inside the sample container. Temperature was controlled by another thermocouple, welded on the back of the tantalum strip. The temperature error was estimated to be about ±1 K at 298 K.

The powder x-ray diffraction patterns were also collected on two compressed pellets made from the cut pieces of PE-I fibers. One of the compressed samples (PE-IP1) was pressed into a pellet at 0.1 GPa for 10 minutes at room temperature. The other, PE-IP2, was pressed into a pellet at 0.7 GPa for 60 minutes at room temperature. Since the cut fibers segments are still considerably longer than the diameter of the fibers (in the order of 10 micrometers), most of the fibers are likely to orient with the long side perpendicular to the applied force, *i.e.*, most fibers are compressed laterally. The pellets were not enclosed in a container but directly placed on the tantalum strip. Only room temperature powder data were taken with the compressed samples.

4.6.3 Small-angle X-ray Scattering

The small angle x-ray scattering (SAXS) experiments were carried out at the Oak Ridge National Laboratory SAXS [94]. In cooperation with Dr. B. Annis, the expert in this characterization at the facility. The instrument makes use of a rotating anode x-ray source (Cu Kα) with pinhole collimation of 2 mm diameter at the sample (chosen to get maximum intensity for the chosen range of Q at sufficient precision), and a two-dimensional, position-sensitive detector of 20×20 cm dimensions. Various angular ranges were used for data collection by changing the sample-to-detector position. The principal results presented in this paper were obtained at a five meter distance for samples PE-II, PE-III, and PE-IV, and two and one meter distances for samples PE-I and PE-V. These correspond to momentum transfers Q of 0.05-0.8, 0.1-2, and 0.2-4 nm^{-1}, respectively [$Q = (4\pi/\lambda) \sin(\theta_{scat}/2)$].

4.7 Density

The densities of the PE fibers were measured in a density gradient column [95] using carbon tetrachloride (1.584 Mg/m^3) and toluene (0.867 Mg/m^3) at 293 K. The data are given in Table 4.1-1. The density of the crystals was computed from the lattice parameters and is shown in Table 4.6-2.

Chapter 5

Results

The results of the first heat capacity measurements on PE fibers are given in this chapter. The existence of a single melting peak for gel-spun UHMMPE is proven and the multiple peaks are shown to be an artifact. The results of fiber shrinkage experiments will be described. All these thermal analysis data are done on the same samples as the full pattern wide angle x-ray diffraction analysis, powder x-ray diffraction, small angle x-ray analysis and NMR. These analysis were done in cooperation with Drs. Fu, Habenschuss, Annis and Chen. The latter data were documented in the following papers and will be summarized here:

1 Fu Y, Chen W, Pyda M, Londono D, Annis B, Boller A, Habenschuss A, Cheng J, Wunderlich B. Structure-property analysis for gel-spun ultrahigh molecular mass polyethylene fibers. J Macromol Sci -Phys 1996;B35(1):37-87.

2 Boller A, Wunderlich B. Thermal Analysis of Gel-Spun Ultra-High Molar Mass Polyethylene. J Thermal Anal 1996;to be submitted:

Account of Additional Work

Extensive work was done to find the best conditions for the measurement of the heat capacity of the polyethylene fibers. The mostly instrumental aspects of this work have been published elsewhere.

1 B. Wunderlich, I. Okazaki, K. Ishikiriyama, and A. Boller, Specific Heat Capacity Determination by Temperature Modulated DSC and its Separation from Transition Effects. Submitted to Thermochim. Acta (1996).

2 A. Boller, I. Okazaki, K. Ishikiriyama, G. Zhang and B. Wunderlich, Determination of Cell Asymmetry in Temperature Modulated DSC. To be published in the Proc.11th Int. Conf. Thermal Analysis and Calorimetry (ICTAC) in Philadelphia, PA, August 11 15, 1996, Full version, submitted to J. Thermal Analysis, (1996).

3 L. C. Thomas, A. Boller, I. Okazaki, and B. Wunderlich, Modulated Differential Scanning Calorimetry in the Glass Transition Region, IV. Pseudo-Isothermal Analysis of the Polystyrene Glass Transition. To be published Thermochim. Acta , (1996).

4 B. Wunderlich, A. Boller, I Okazaki, and S. Kreitmeier, Modulated Differential Scanning Calorimetry in the Glass Transition Region II. The Mathematical Treatment of the Kinetics of the Glass Transition. In print J. Thermal Analysis for publication in (1996).

5 B. Wunderlich, A. Boller, I. Okazaki and S. Kreitmeier, Linearity, Steady State, and Complex Heat Capacity in Modulated Differential Scanning Calorimetry. To be published, Thermochim. Acta (1996).

6 B. Wunderlich and A. Boller, Modulated Differential Scanning Calorimetry Capabilities and Limits. Proc. 24th NATAS Conf., in San Francisco, CA, Sept. 10 13, 1995, Editor, Shaheer A. Mikhail, pgs. 136-141. Full version by A. Boller, I. Okazaki, and B. Wunderlich, Modulated Differential Scanning Calorimetry in the Glass

Transition Region, III. Evaluation of Polystyrene and Poly(ethylene terephthalate). Thermochim. Acta 284, 1, 1-19,(1996).

7 A. Boller, C. Schick, and B. Wunderlich, Modulated Differential Thermal Analysis in the Glass Transition Range. Proc. 23rd NATAS Conf., in Toronto, Canada, Sept. 25 28, 1994, Editor, John B. Enns, pgs. 464 469. Modulated Differential Scanning Calorimetry in the Glass Transition Region, Thermochim. Acta, 266, 97 - 111 (1995).

8 B. Wunderlich, Y. Jin, and A. Boller, Mathematical Description of Differential Scanning Calorimetry Based on Periodic Temperature Modulation, Thermochim. Acta 238, 277 293 (1994).

9 Y. Jin, A. Boller, and B. Wunderlich, Heat Capacity Measurement by Modulated DSC at constant Temperature, Proc. 22nd NATAS Conf., Denver September 19-22, 1993, Editor K. R. Williams, pgs. 59 64. Full paper published by: A. Boller, Y. Jin and B. Wunderlich, J. Thermal Analysis 42, 307 330 (1994).

5.1 Heat Capacity of PE

In order to analyze the heat capacity of any material the expected and experimental values need to be compared. For a one-phase, crystalline-low-molar mass material in equilibrium, there is a definite value for the heat capacity at all temperatures. For macromolecular materials, a variety of macroconfor-

mations of the amorphous and the crystalline, extended chain macroconformation have significantly different heat capacities in some temperature ranges. In order to classify a material under investigation, these two limiting values need to be determined as a function of temperature.

5.1.1 The Limiting Values For Heat Capacity

The limiting values for the heat capacity of amorphous and crystalline polyethylene are determined from the crystallinity-dependent heat capacity. A series of 67 published heat capacities with known crystallinity was already collected and interpreted in an earlier publication of this laboratory [96]. A literature search for newer publications showed no additions, so that these values were analyzed in more detail than originally. The literature research was performed electronically on the database of the chemical abstracts with the time restrictions of 1980 to present. The keywords included 'heat capacity', 'heat content', 'specific heat' and 'polyethylene'.

Fig. 5.1-1 contains all the data collected in the earlier studies together with the recommended ATHAS Data Bank values for the limiting heat capacities of the glassy and the crystalline material. For the details of the individual measurements, such as method of crystallinity determination and temperature range of the measurement, the original literature should be consulted. The transition temperatures, 237 K for the glass transition and 414.6 K for the equilibrium melting transition are marked with solid vertical lines. Between the glass transition and the melting transition, the extrapolation of the liquid heat

capacity is used as the amorphous reference heat capacity due to the fact that the apparent heat capacity of the semicrystalline samples in this range is dominated by an increase in gauche conformations and the premelting effects of small crystals. Below the glass transition, a recommended experimental heat capacity for the 100 % amorphous state, which will be derived in the following, is also shown.

Figures 5.1-2A-D show the crystallinity dependent heat capacities at 1, 10, 150 and 250 K with their linear regression. In order to become familiar with the error associated with the extrapolation the 95% prediction interval and the confidence interval are shown. The dashed lines are the limits within which 95% of the predicted regression lines fall. The dotted lines are the limits within which 95% of the individual points fall. In Figs. 5.1-2B-D, the open squares represent values which are obviously outside the confidence interval and are therefore excluded from the linear regression. These values are associated with samples of high molar mass at low crystallinities. It is unknown whether the error is in the determination of the heat capacity, the crystallinity, or a systematic error of the particular measurement. Unpublished results by Y. Jin in the ATHAS Laboratories confirm that the heat capacity of UHMMPE can be determined with the same accuracy as for low molar mass PE. It is therefore suspected that the error is in the crystallinity determinations.

All extrapolated heat capacity values for the fully amorphous and the 100% crystalline case are plotted as a function of temperature in Fig. 5.1-3A. The recommended ATHAS Data Bank values are drawn as solid lines. The

100% amorphous Data Bank values are extrapolated from the melt heat capacity measured over a 200 K range above the melting temperature. The heat capacity for the 100% vibration-only case is derived from the extrapolated experimental values fitted to the vibrational spectrum with the appropriate equations [97-102].

In Fig. 5.1-3B, the r^2 values of the linear fit are plotted as a function of temperature. The differences between the extrapolated amorphous and crystalline heat capacities, which correspond to the slopes of the curve fit in Fig. 5.1-2, are drawn as a function of temperature in Fig. 5.1-4A (filled circles). These values, when divided by the limiting amorphous and crystalline heat capacities at the same temperature are shown in Fig. 5.1-4B. The r^2 and the $\%\Delta Cp$ curve have a number of distinct features. These features are labeled A-F in Fig. 5.1-3B and in Fig. 5.1-4B. The meaning of each temperature region is as follows: The low temperature heat capacities in the range of 10 to 25 K (A) are of high quality with a significant percentage difference in the limiting heat capacities. The r^2 value is therefore close to one. In the range from 25 to 175 K (B), a r^2 value ranging from 0.7 to 0.95 indicates that the flatness of the crystallinity dependence prevents an accurate connection between the crystallinity of a sample and its heat capacity. Significant differences in the crystalline and amorphous heat capacity, starting at 175 K, however, do not improve the quality of the fit. The drop in r^2 values at 175 K (C) is an indication of increased uncertainty of the heat capacity to crystallinity correlation. It falls into the area of the glass transition. The determination of the heat capacity in the glass transition is a time dependent

phenomena and also reflects the thermal history of the sample. In addition, it is a function of the heating rate of the measurement. Since the data were collected from many researchers and a multitude of thermal treatments of the samples were involved, it is not surprising that in the glass transition the heat capacities show only a limited correlation with the crystallinity. The drop in the r^2 values can therefore be directly linked to the glass transition. It is important to note that to date this method has not been applied. It may, however, be used in the future for the determination of the glass transition in special cases.

The drop and recovery in the r^2 value (C) is followed by a region of almost perfect correlation between heat capacity and crystallinity (D). In the range from 250 to 330 K, values > 0.95 for r^2 are observed. The drop in r^2 from greater than 0.95 to 0.9 in the range above 330 K may be caused by a change in crystallinity due to partial melting of small crystals in semicrystalline material.

Fig. 5.1-3A also shows the recommended ATHAS Data Bank values as solid lines in the range above 170 K. The value of 237 does correspond to the intersection of the extrapolated 100% amorphous heat capacity (Fig. 5.1-3) and the 50% line between the extrapolated melt heat capacity and the extrapolation of the 100% amorphous heat capacity in the range of 170 to 200 K.

The values for the percentage difference between the limiting values in Fig. 5.1-4B with the same features as the r^2 values plotted as a function of temperature shows two step increases in region (C) and (D). These two separate regions will be used in the interpretation of the fiber heat capacities to

5.1.2 Heat Capacity of UHMMPE Fibers

The heat capacity of any polymeric material is basic information for the analysis of its phase transitions, degree of crystallinity and the temperature range of end use. It is therefore surprising to find that there is no literature on the heat capacity of ultra-high molar mass PE fibers. The measurements presented in this dissertation are therefore the first published data of the heat capacity of UHMMPE fibers.

The lack of results may be due to the fact that, in the measurement of heat capacity of fibers, errors in the range of greater than 10% are commonly observed when applying standard techniques. The problems of sufficient sample mass, non-reproducible settling of the sample inside the sample pan, annealing effects, and other variables have discouraged many people from even attempting to measure precision fiber heat capacity.

The use of multiple samples, measured on heating as well as on cooling, and the use of special sample preparation techniques did however lead to standard errors in the order of 1-3%. These values are comparable to commonly achieved precision in heat capacity measurements by DSC for far less critical samples. In order to have reproducible sample preparation with a maximized sample mass, a winding device was developed as described in the experimental section. The sample masses achievable in this manner were in the order of 20 to 30 mg, which is sufficient for precision heat capacity measurements. Of each material, a number of samples was prepared and measured a minimum of six

times. Each experiment consisted of two heating and two cooling segments. Each of the overall heating or cooling segments had isothermal holds at every 20 K to ensure a optimal correction of the baseline drift. In addition, the heat capacity calibration, including the measurement of the empty pan and the sapphire standard, were performed before and after each measurements series of no more than five experiments. No improvement of the heat capacity data could be detected for the cases where the empty pan and the sapphire measurement were performed before and after each measurement.

The results of the heat capacity measurements for the samples PE-I, PE-II, PE-III, and PE-VI are shown in Fig. 5.1-5. The ATHAS Data Bank values for solid and liquid PE are given as a reference. To eliminate minor systematic errors, the results for all materials were shifted to fit to the vibration-only heat capacity at 180 K, a temperature where only negligible deviations between the samples are expected. Figure 5.1-6 shows the so-corrected data. The post-stretch annealed samples (PE-I, II and III) have identical heat capacities after the correction. The sample PE-VI, which is not post-stretch-annealed shows a step increase in heat capacity over the other samples in the range from 260 to 290 K. In Fig. 5.1-6, the experimentally determined heat capacity of an extended chain polyethylene, measured by Wunderlich (1965) [103] is included as well. The heat capacity of the fully crystalline material falls below the vibration-only heat capacity in the range 250 to 340 K. This was suggested earlier to be due to anharmonicity effects, which are not included in the vibration-only heat capacity calculation. Above this temperature, the increasing number of gauche

conformations in the polyethylene chains increases the heat capacity of the fully crystalline, extended chain material.

The differences between the experimentally determined and the vibration-only heat capacity of the ATHAS Data Bank are plotted in Fig. 5.1-7. The step increase of the heat capacity of PE-VI over the heat capacity of all other fibers between 260 and 290 K is 1.4 J/(mol K). The difference between the experimental fiber heat capacities and the experimental heat capacity of the fully crystalline extended-chain polyethylene in Fig. 5.1-8 shows three distinct regions. The first region between 190 and 290 K shows a continuous increase in the heat capacity of the fibers over the heat capacity of the extended-chain material. Please note that the increase of approx. 3 J/(mol K) is in part due to the simultaneous drop in the extended chain heat capacity. At the end of this region, PE-VI shows the additional 1.4 J/(mol K) increase as already described. The temperature range from 290 to 360 K is dominated by a plateau in the heat capacity for all fibers. The existence of this plateau shows that the increase in heat capacity due to the gauche conformations occurs at the same rate in the fibers as in the fully crystalline extended-chain polyethylene. For PE-VI, this plateau shows a slight increase starting at about 350 K. All other fibers show the start in increased heat capacity after the plateau at 370 K. This increase in heat capacity occurs reversibly. It is regarded as the start of the isotropization of the intermediate non-crystalline fraction.

The results of gel-spun heat-set ultra-high molar mass polyethylene fiber heat capacities revealed a series of interesting results:

- The heat capacities of all different heat-set fibers are identical after the correction for deviations below the glass transition.
- The comparison of heat-set and gel-spun fibers without heat setting is possible due to the increase in heat capacity between 260 and 290 K. The implications of this will have to be found by more detailed studies of the temperature dependence of the mechanical properties.
- Comparison of the fiber heat capacity with 100% crystalline PE material allows the separation of A) a glass transition of the intermediate non-crystalline phase below 290 K, B) a plateau region with no additional cp increase from 290 to 370 K and C) the start of premelting over the gauche contribution to the cp increase above 370 K.

5.2 PE Melting

5.2.1 Melting of Bulk PE

The melting of a polymer is a complex affair. Due to the metastability of the semi-crystalline polymer, a series of events can take place prior to melting and during the melting transition itself. These effects are A) melting of small crystals much earlier than the equilibrium melting temperature, B) recrystallization of the molten material and C) melting into a strained rather than an isotropic melt state.

The melting temperature is also a function of the heating rate at which it is measured. For slow heating rates the pre-melting and reorganization has more

time and therefore leads to higher melting temperatures for poorly crystalline material. The initially poorest crystals therefore can have the highest melting temperatures.

The melting of extended chain material is also heating rate dependent. The effect is however opposite to the poor crystals. The heat transfer from the oven into the sample and the rate of crystal melting lead to higher than expected melting points for faster heating rates. Only at very low heating rates can the equilibrium melting temperatures be detected [33,105-108]. For the small heating rates of a dilatometric experiment, the extended chain polyethylene melts to 80% within 1.6 K at a melting temperature of 414.6 K.

5.2.2 Melting Behavior of UHMMPE Fibers

The interpretation of differential scanning calorimetry (DSC) on melting of ultra high molar mass polyethylene (UHMMPE) fibers has been the focus of much research [42,105,109-116]. Multiple melting peaks were described for such fibers in many of the cited papers. The multitude of different polyethylenes has led to the publication of many different, often conflicting reports on the shape and position of one or more melting peaks. For the understanding of material properties and the correlation of DSC with other experimental methods, it is important to clarify the true nature of the transition for any given sample.

The first endothermic peak is usually assigned to the melting of the orthorhombic phase [12,41]. An alternative assignment is that the first peak is the orthorhombic-hexagonal phase transformation and the second, the melting of

the hexagonal phase [117]. The majority of the orthorhombic crystals can, however, only transform to the hexagonal phase when the fiber is constrained [41,117] or irradiated [38,41,118,119]. Under both conditions, the longitudinal mobility of the polymer chains is hindered. When the temperature exceeds about 350 K, the chains become conformationally mobile. If the chains are hindered to form random coils, the orthorhombic phase transforms at somewhat higher temperature into a condis phase [58], *i.e.* the hexagonal phase. The melting behavior of these fibers is to be discussed further by combining results of several techniques.

The multiple melting peaks observed on differential scanning calorimetry (DSC) of ultra-high molar-mass polyethylene fibers (UHMMPE) are analyzed as a function of sample mass. Using modern DSC capable of recognizing single fibers of microgram size, it is shown that the multiple peaks are in part or completely due to sample packing. Loosely packed fibers fill the entire volume of the pan with rather large thermal resistance to heat flow. On melting, the fibers contract and flow to collect ultimately at the bottom of the pan. This process seems to be able to cause an artifact of multistage melting which is dependent on the properties of the fibers. This method has shown to greatly reduce, or even eliminate, errors of this type. The crucial elements of the analysis of melting behavior and melting temperature are decreasing the sample size and packing the individual fibers in a proper geometry, or introducing inert media to enhance heat transport.

Double melting peaks that were characteristic of the processing conditions of the fibers were observed as were reported before for similar samples [120]. Since no significant amounts of monoclinic or hexagonal crystals were found, polymorphism could not be at the root of the double peak. Since no lamellae were present, this could also not be a reason for the double peak. Finally, since the melting peak areas did not change with heating rate, and it was possible to separate the melting peaks by partial melting, no dynamic recrystallization could be the cause for the double peak. Therefore, the two melting peaks were assigned to orthorhombic crystals with different degrees of restraint to the surrounding intermediate, oriented phase [120]. This solution is not fully satisfying since no clear evidence of a bimodal distribution of crystal sizes could be found from the wide- and small-angle X-ray data. It will be shown in the following that a much simpler interpretation is possible. The double melting peak is an instrumental effect and can be made to disappear by changing the experimental conditions.

Multiple peaks as an effect of instrumental conditions have been studied earlier [80] using a Perkin-Elmer power-compensation DSC. It was shown that the horizontal alignment of small indium pieces along the diameter of the sample pan could produce multiple melting peaks. The one- dimensional non-uniform distribution of the sample inside the pan in such an experiment may well correspond to the three-dimensional, non-uniformity of fibrous samples. The effects of such non- uniform sample arrangement with respect to the DSC sensors has to be considered in special cases. They can be minimized with

different instrumental designs. Both a multiple thermocouple design (Mettler-Toledo) or a sensor larger than the sample pan (TA Instruments) are self- averaging and lessen the effects of the horizontal non-uniformity. It was shown, that in addition to the horizontal positioning of the sample, one also needs to analyze the vertical change in packing within the sample pan, when dealing with the melting behavior of fibrous UHMMPE. Some of the findings of earlier studies are possibly in need of reevaluation in the light of the presented research.

Figure 5.2-1 shows the melting of UHMMPE fibers measured with parameters such as those commonly used in the literature [112,113,121,122], namely 3 to 5 mg mass and a heating rate of 10 K/min in crimped aluminum pans. These data were measured with a standard TA Instruments 912 DSC as described in Ref. [120]. The melting shows clear double peaks and the temperature range is rather broad. The difference between onset of melting and the end of the peak is of the order of 10 to 25 K. The new results of DSC experiments on PE-III in uncrimped pans as a function of sample mass are shown in Fig. 5.2-2. The peak shape at the lowest mass of 24 micrograms has no double melting peak. The increase in mass gradually introduces two effects, first a broadening of the melting peak, then the development of shoulders and secondary peaks. At masses over 3 mg, the shapes shown in Fig. 5.2-1 are reached. None of these effects are visible in the second and third melting. The measurement curves of these runs are therefore omitted. However, a graphic representation of the temperatures of onset, peak, and end of the peak is shown

in Figs. 5.2-3A and B for the first melting and on second and third heating, after cooling from the melt at about 40 K/min. It is clearly visible that, in the first heating runs, the onset temperature varies only within the experimental repeatability. The peak temperature and the end of the peak are, however, much smaller for the 24 microgram sample, as can also be seen in Fig. 5.2-2. Its melting range is only about 3 K. In contrast, the second and third runs show a much lower onset of melting and little change in melting range with sample size, an indication of inherent broadness of melting. The melting peak areas are shown in Figs. 5.2-3C and D. They indicate a trend toward smaller values for smaller masses. The 100% value was taken from the heat of fusion of completely crystalline polyethylene (293 J/g) [34]. At the smaller masses, weighing errors start to be significant. Therefore, the absolute values for the transition enthalpies are less accurate for the smaller samples, and only the peak shapes should be used to discuss the melting kinetics.

In order to determine whether the differences between the smaller and larger sample are caused by insufficient heat conduction, a test was performed in which a sample of approximately 1 mg of PE IV fiber was packed into the sample pan with layers of powdered, anhydrous aluminum oxide. By utilizing this method, the thermal conduction to the top of the fiber sample is assured. Figure 5.2-4 is the result. Only one single peak is observed on both first and second heating. As for the small sample of PE III in Fig. 5.2-2, the melting peak on first heating is much narrower than in Fig. 5.2-1, and the second run corresponds to Fig. 5.2-3B.

The analysis of the melting behavior of UHMMPE fiber samples in Figs. 5.2-1 to 5.2-4 shows that sample preparation is crucial. Both the placement of single layers of fibers at the bottom of the pan and the filling of the spaces between the fibers with powdered alumina makes the double melting peaks disappear. This is a strong suggestion that the double melting peaks for UHMMPE gel-spun fibers are artifacts. The rather poor contact of the thin fibers with the pan, their unique contraction on melting, and their slow flow seem to provide not only the reason for an interrupted melting and broader melting peak but also the reproducible differences for the different types of fibers.

Further differences can be introduced by restraining the fibers. The differences between the melting curves in Figs. 5.2-1 and 5.2-2 for about equal masses are probably due to compression and partial fixing of the fibers after crimping of the pans in the runs shown in Fig. 5.2-1. Most examples in the literature were similarly crimped. It is well known that melting of fibers held at constant length have considerably sharper melting peaks [1].

The single, rather sharp melting peak of the fibers is much more in line with the structural picture developed earlier. The nanophase-separated, intermediate phase keeps its orientation because of its connection to the crystals by tie molecules. In turn, the tie molecules also cause the superheating of the crystals. In the beginning of melting, they hinder the molten molecules to reach a random-coil macroconformation and thus to gain a lesser amount of entropy, which in turn, causes the higher, local melting temperature. As soon as the

network of crystals collapses, however, the local melting temperature drops and the melting accelerates, *i.e.* the peak sharpens.

5.3 Shrinkage

Shrinkage is a structure-sensitive property. It needs, for its description, knowledge about the orientation frozen into the fiber and its relaxation mechanism. Shrinkage is caused mainly by randomization of strained, oriented, noncrystalline chains. The glass transition and fusion temperatures determine the onset of shrinkage and reveal the type of hindrance that keeps the orientation from relaxing.

One can distinguish at least three different stages of shrinkage. The first begins close to the glass transition temperature of the amorphous part. In the presence of rigid-amorphous fractions, there may be further shrinkage in the temperature range where the rigid-amorphous fraction becomes mobile (second stage). These glass transitions of rigid-amorphous material are often broad and not monotonous and may occur anywhere between T_g and T_m. The continuous rearrangement of molecules from a metastable highly oriented state into a thermodynamically favored crystalline state occurs simultaneously with the melting of crystalline regions of very small size. A randomization of the intermediate oriented fraction in the x-y plane due to higher mobility leads to a slow continuous shrinkage in the z-axis (fiber direction). Some of the crystalline

regions are so small that the destabilizing surface energy is greater than the stabilizing enthalpy of crystallization.

The third cause of the beginning of shrinkage is fusion of crystals. In the region of increased crystal melting, the material becomes too weak to support the forces necessary to measure the expansion, and catastrophic failure is the result. Before the failure of the sample, a shrinkage can be observed, due to the molecules achieving the liquid state and losing the anisotropic character. Complications are expected in this case, due to the broad and often bimodal crystallite size-distributions. To sort out the different, often overlapping mechanisms is only possible by combining several analysis techniques, such as DSC, NMR, and the structure analysis concentrated on in this research.

The shrinkage behavior of PE fibers was investigated using Thermal-mechanical analysis (TMA) at a heating rate of 10 K/min, hot stage microscopy with continuous heating rates of 2-5 K/min as well as the observation of a macroscopic fiber in a thermostated oil bath, where the temperature was increased in small steps.

5.3.1 TMA

Thermal-mechanical analysis (TMA) can be used to investigate the dimensional changes of the sample under investigation. The measurement can be performed in either the compression, the bending, or the extension mode. Importantly, the fibers can only be measured in the extension mode with a special fiber extension

measurement head. During linear heating, the main feature of a TMA analysis is shrinkage due to randomization of the chains.

Sample PE-I shows its shrinkage in a very narrow temperature range. This is the relaxation, probably first due to relaxation of rigid-amorphous [123], followed by the beginning of melting. A comparison with the heat capacity analysis shows that the onset of the shrinkage occurs after the onset of the isotropization of the intermediate non-crystalline material. It is probable that a considerable amount of cooperativity among the non-crystalline material is required for the shrinkage.

More information on the stages of the breakdown of the network of crystal, intermediate phase, and rigid-amorphous fraction and the subsequent relaxation of the oriented chain segments that gained mobility is needed. Presently, it is only possible to qualitatively assign release mechanisms for shrinkage and deduce from the magnitude of the observed shrinkage the existing strain. There is some hope that solid state NMR may yield further information on mobility and domain sizes of the various parts of the molecules.

The shrinkage curves for the samples of the present analysis are more similar: the fibers do not shrink at the bulk T_g but then start to shrink smoothly until melting. Based on the samples PE-I and PE-IV, one expects that the initial or all of the shrinkage is linked to mobilization of rigid-amorphous material.

Typical TMA curves on two single, gel-spun UHMMPE fibers are shown in Fig. 5.3-1 and 5.3-2 (PE I and PE IV). The reproducibility of single fiber TMA experiments for each of the samples can be seen within the figure. Each curve

corresponds to one experiment. All TMA shrinkage curves show a series of characteristic features. Until the melting region, only a small amount of shrinkage is observed. This is followed by a substantial shrinkage in the first melting region with a sharpness that mirrors the DSC melting peak. Next, one observes a plateau. Finally, the complete failure of the fiber is obvious as all crystals are molten, and viscous flow makes the fibers extend and ultimately fail.

The differences in the samples PE-I and PE-IV are significant for the case of single filament TMA measurements. Due to the insufficient control on the force acting on the individual fiber, it is however not possible to perform any quantitative calculations on expansivity. The temperatures determined in a TMA on the other hand, are significant and detected with good precision. In Fig. 5.3-3, two examples of the insufficient control on the force acting on the sample are given. Curve A represents a measurement on a single filament with the applied force being slightly larger than in the examples in Fig. 5.3-1 and 5.3-2. Curve B shows a measurement on a fiber bundle. The same temperature for maximum change in dimension is found in the latter case only. In the measurement with the excessive force on the fiber, a failure of irreproducible nature occurs. The fiber bundle experiment shows a shrinkage behavior much like the PE-I fibers in the single filament measurement. Due to the distribution of the forces on the individual filaments, the shrinkage behavior before melting cannot be seen. Due to the additional problem of aligning all 150 filaments in a strand and the possibility of slippage in the aluminum ball fixture, the fiber bundle measurement was not further pursued.

The results from the TMA experiments show distinct differences for the samples PE-I and PE IV. The high modulus fiber PE-I shows only a very small shrinkage until 410 K and catastrophic failure occurring at 428-429 K. Presently, there is no explanation for the peculiar peak shape between the initial shrinkage and the plateau.

The low modulus PE-IV on the other hand shows a broad shrinkage increase from 320 to 410 K with an "onset" of rapid shrinkage at 404 K. The plateau shrinkage values depend on the individual handling of the fiber during the preparation and cannot be used for comparison. The maximum shrinkage value for PE-IV was confirmed with a measurement of a strand of about 170 filaments. The shrinkage features before the steep increase at 404 K are lost, but the maximum shrinkage agrees with the measurement of a single fiber, when the force on the fiber was optimal.

5.3.2 Fiber Shrinkage in a Glass Capillary

To reduce the force on the fiber to zero, direct observation of a PE-I fiber in a glass capillary was done. No significant isothermal shrinkage was observed up to 417 K proving that most of the TMA experiments are dependent on the force applied. At 418.2 K, the fibers shrink, but the birefringence is not zero for the contracted fiber. Other researchers reported that under nonisothermal condition on heating at 10 K/min UHMMPE fibers shrink at about 428 K and initial stress develops at temperatures above 393 K [124].

5.3.3 Shrinkage Without Force in Microscope

The observation of fiber shrinkage on a microscopy slide in a hot-stage was done in order to observe the behavior of PE fibers from room temperature to 430 K. Fig. 5.4-1 gives the results of one such experiment with 60x magnification. Fig. 5.4-1A shows the arrangement of the individual PE-I fibers of approximately 1 mm length and 0.03 mm in diameter at room temperature. Fig. 5.4-1B shows the same fibers at the end-temperature of 430 K. The fibers shrink in a very narrow temperature range of 0.5 K. Before reaching this temperature, the shrinkage of the fibers is not noticeable. The one-stage shrinkage observed for PE-I reduces the fiber length by a ratio of approximately 14:1. This results in final end-to-end distances of 7% (min 6, max 14%) of the original length. In Fig. 5.4-2, the results of PE-III fibers are displayed in the same manner. The final longitudinal dimension corresponds to 14% (16,12,14,14,14,15%). The final diameter is 250% (275, 236 , 254, 256, 236, 254%) of the original diameter.

The findings of the thermo-optical observations confirm a one-stage shrinkage. The result is that at the temperature of 420 K, the fibers are not flowing significantly. Further studies with regard to the viscosity of the melt of high molar mass polyethylene might give insight into this phenomenon.

In summary, it can be said that the absence of a shrinkage prior to the temperature of melting in the DSC, is one more indication of the proposed fiber model, where the intermediate non-crystalline and the crystalline material form a two-phase nano-phase separated entity. In all shrinkage experiments without the application of an external force, the fibers shrink far less than what would be

needed to reverse the total extension of the fiber experienced during manufacturing. The maximum drawing of up to 200x in the manufacturing of fibers would correspond to a shrinkage of 99.5 % (!).

5.4 Optical Microscopy

Optical microscopy is considered a relatively useful means by which theories can be supported or discredited. The observation of the physical shape of a sample is unrefutable evidence and can be performed without great effort. A microscopy hot stage was used for the direct observation of fiber shrinkage without force. For the documentation of sample preparation and the analysis of sample shape after the DSC experiment, no special equipment other than the microscope is needed.

The optical microscopy was performed on the various fibers to directly observe the shrinkage effects without any forces on the fibers. The distance from control thermocouple to the position of the fiber did not allow for the perfect calibration of the temperature at which the shrinkage occurred. Direct observation of the heating process did however confirm that the shrinkage of the fiber was instantaneous. Moreover, the shrinkage in the individual fibers on the microscopy slide occurred at various instants. This effect was attributed to the various positions of the fibers which were due to thermal gradients on the slide.

5.4.1 Documentation of Sample Preparation

The analysis of multiple melting in DSC experiments required samples of rather small masses. In this part of the dissertation, the figures are an indication of the reasons for multiple melting at larger sample masses and show the amount of material typically used in the sub-milligram measurements. Fig. 5.4-3A&B represent the 25x magnification of a typical 1.5 mg sample of PE fibers with the polarization filter in two positions. The filter position (crossed polarization filters) in Fig. 5.4-3A enhances the visibility of the fibers giving the impression of a full sample pan. The illumination (parallel polarization filters) in Fig. 5.4-3B enhances the aluminum pan and shows the loose packing of the fibers. This loose packing and the various distances of the sample from the bottom of the pan are thought to be responsible for the multiple melting of PE fiber samples in standard DSC experiments.

The sub-milligram sample sizes are represented by the two pictures in Figs. 5.4-4A&B. The sample in Fig. 5.4-4A has a mass of less than 0.1 mg. Such samples are used for the analysis of the melting temperature for PE fiber samples. Fig. 5.4-4B shows a sample mass of about 0.5 mg. The picture illustrates that even at this relatively low mass not all of the individual fibers touch the aluminum pan. As a consequence, a minor effect on the shape of the melting peak is already expected at this sample mass.

Another sample of 1.5 mg was prepared to demonstrate the influence of the thermal resistance from the bottom of the pan to the fibers. Figures 5.4-5A&B show a 20x magnification of the preparation of the fiber sample. In Fig.

5.4-5A, the fibers and the bottom of the pan are still visible while Fig. 5.4-5B shows the final sample with all the fibers embedded and covered in anhydrous, aluminum oxide powder. The results of this experiment (Section 5.2) showed only one single peak, confirming that the heat transfer from the bottom of the pan to the top of the fiber sample is of prime importance to the generation of multiple melting peaks.

5.4.2 Observation of Fixed Length Shrinkage

The experiments performed under fixed length involved the use of a piece of aluminum as the central core of a one-layer fiber spool. A 20x magnification of one such experimental set-up is displayed in the top picture of Fig. 5.4-6 before the DSC experiment, and after the DSC experiment, in the bottom figure. The maximum temperature in this experiment was 440 K. Complete melting appears to have occurred.

5.5 Fiber X-ray Diffraction Method

5.5.1 Full-pattern X-ray Fiber Diffraction Refinement

The two-dimensional diffraction pattern of PE-III is shown in Fig. 5.5-1 (after corrections for absorption and polarization). The results of the full-pattern refinements are listed in Table 5.5-2. All structure and morphology parameters known to describe crystals have been included in the structure model. The

refined crystal structure model is, hence, the most complete one that has ever been made to describe the crystal structure of PE fibers. The comparison of the observed and calculated fiber diffraction intensities on the layer lines (00ℓ, ℓ = 0-4) of the four samples is given in Fig. 5.5-2.

The small peak at 2.20 nm^{-1} on the equator is the 010 reflection of the monoclinic phase (just before the much stronger orthorhombic 110 reflection, see Fig. 5.5-2D, for example; the monoclinic unit cell is: a = 0.809, b = 0.479, c = 2.53 nm, γ = 107.9° [10], in early analyses the monoclinic phase is sometimes described by its primitive triclinic unit cell [2]). Since there is much less monoclinic than orthorhombic PE, only the structure of the latter could be refined by the full-pattern method. More information about the monoclinic phase was gained from the powder patterns.

The positions of the calculated diffraction peaks in Fig. 5.5-2 agree well with the observations. The unit-cell parameters that are linked to the positions of the reflections are thus accurate. However, the intensity fitting is not always satisfactory. Only for sample PE-IV does most of the observed diffraction peaks agree with the calculation. For PE-I-III, some of the peaks deviate. For example, PE-I has a 25-30% lower calculated intensity for the strong 002 reflection. The fitting of this single peak could be improved by adjusting some of the crystal structure parameters, such as axial crystallite size. Nevertheless, the results of the full-pattern refinement must be judged by the overall fit and not any single reflection. It is not possible to improve the fitting of the 002 reflection by changing the values of the parameters without worsening the overall fit.

Introduction of an anisotropic temperature factor was attempted but could not significantly improve the fit. Neglecting the correction for the diffuse thermal scattering (TDS) [125] may cause lower calculated intensities at a high diffraction angle (θ) but may not be the main factor for a poorer fit at a low angle. The nearly perfect fitting for sample PE-IV also implies that the poorer fit of PE-I-III is due to structural differences and not instrument problems or omission of some correction within the calculation.

In the earlier study of PE-I, it was found that the fitting can be significantly improved by introducing major disorder to the crystal structure [23]. Such analysis assumes that the fiber consists of only two phases (crystalline and amorphous). In addition to the ideal orthorhombic position for the carbon atom, one had to assume three additional positions that were fractionally and randomly occupied by 20% of the carbon atoms. All these disorder positions were still observed in the (004) layers. The temperature factors of the hypothetical atoms (U = 0.002 nm^2) were considerably larger than those in the ideal positions (U^{11} = U^{22} = 0.001 nm^2, U^{33} = 0.0005 nm^2). The overall fitting of the intensities of the two-phase structure model (Fig. 1 in Ref. [23]) is better than that for the ordered crystal shown in Fig. 5.5-2A. In addition, this two-phase model was tested with the PE-III of the present study. The overall fitting, as well as the fitting of the 002 reflection, was also improved by using the disorder model.

The structure determined by x-ray diffraction is the position and time average over all crystals and noncrystalline material that scatters x-rays. For a fiber with multiple phases, an apparent disorder does not necessarily imply that

the structure of the crystalline phase is disordered. Importantly, the question to be resolved is whether there exist only disordered orthorhombic crystals, as assumed in Ref. [23], or the observed disorder results from the average of more than one oriented structure, as assumed in the present paper.

In the orthorhombic crystal, the carbon and hydrogen atoms are located on the z = 1/4 layers with spacings of $c/2$. As long as some disordered C and H atoms are found on (004) layers, regardless of their order in the lateral directions, their scattering contributes to the 00ℓ ($\ell = 2n$) reflections. Presence of the added intermediate phase with largely *trans*-conformations of closely similar CH_2-spacing to the crystal is the alternate explanation for the poor fit of the observed intensities of Fig. 5.5-2. If neighboring chains of the intermediate phase do not locate exactly on the same layer as the crystal, the averaging over all atoms of the intermediate phase is equivalent to atoms added on the (004) layer, but with a significant temperature factor along the fiber direction. The greater the deviations of the atomic positions from the (004) layers, the larger the temperature factor is, and the weaker the intensity contributed to the 00ℓ ($\ell = 2n$) reflections is. In the lateral direction, the *ab* plane of the crystal, the arrangement of the chains of the intermediate phase no longer have crystalline ordering, so that the atoms of the intermediate phase are not located coherently in the lateral directions, such as crystal direction [110]. Such a one-dimensional, oriented intermediate phase can contribute unevenly to different diffraction peaks and is easy to visualize. For example, the 002 peak may result from both the crystalline and the intermediate phase, while the 110 peak results only from the crystals.

The ratios of the integrated intensities of 002 and 110 for PE-I and PE-IV are 3.0 and 1.1, respectively, and characterize their structural differences.

The size of the crystals of sample PE-III had been determined previously [126,127]. The axial crystallite size of 5.8 nm of Table 2 agrees well with the value of 6 nm found in one of the previous studies [126]. Both values are obtained with the assumption that the broadening due to size and the distribution of the disorientation are Gaussian. Both these values are, however, significantly smaller in the third study (13.9 nm) [127]. The lateral crystallite size of 7.7 nm in Table 2 is smaller than in both previous papers. The crystallite sizes of this study, especially the axial sizes, are also smaller than reported in most earlier studies of other UHMMPE fibers.

The crystallite size which is estimated by x-ray diffraction is based on the width of diffraction peaks, using the Scherrer equation [125]. With the traditional evaluation method, the crystallite size in one direction is estimated based on the peak width of a single diffraction peak. For example, the axial size is usually estimated from the 002 peak. It has been reported, however, that the axial crystallite size of highly drawn PE estimated from the 002 reflection is larger than when estimated from the 004 reflection, which, in turn, is greater than that from 006 [128]. With the full-pattern method, the crystallite size is determined from the best overall fit of all peak widths and by separating the effects of paracrystallinity and disorientation on the peak widths [129]. These differences in data treatment may well explain the differences between the various reports. The influence of the presence of a considerable fraction of a highly oriented intermediate phase is

another possible source of error for the evaluation of size that will be discussed below.

The disorientation parameter measures the angular distribution of the crystallites with respect to the fiber axis. The distribution is assumed to be Gaussian [23]. The value of the disorientation for PE-III (1.15°) is smaller than that found before (2.1°) [126]. Again this discrepancy may be caused by the removal of the sharper background scattering and the inclusion of the paracrystallinity correction in the present study. The second-order polynomial used in Ref. [126] led probably to the removal of a flatter background.

5.5.2 Powder X-ray Diffraction

The powder diffraction of the unpressed PE-I sample is shown in Fig. 5.5-3. The room-temperature patterns of the two compressed samples (PE-IP1 and PE-IP2) are presented in Fig. 5.5-4. The small peak in Fig. 5.5-3, centered at about 2θ = 19.5°, is the 010 reflection of the monoclinic phase of PE [10,41,113]. The intensities of the monoclinic peaks are considerably larger in the compressed sample PE-IP1 (see Fig. 5.5-4). However, the increasing of the pressure from 0.1 GPa to 0.7 GPa and prolonging the compression time from 10 to 60 minutes does not bring any further increase (sample PE-IP2, shown in Fig. 5.5-4). Even with the uncompressed fiber, the monoclinic peak is more visible in the powder pattern than in the fiber pattern (compare Figs. 2 and 3). The powder intensity (I_p) at a given reciprocal distance r is the azimuthal average of the two-dimensional fiber intensities (I_f), and the relationship between I_p and I_f is given by:

$$I_p = \frac{1}{2\pi r}\int_0^{2\pi} I_f d\phi , \qquad (2)$$

and:

$$r = (s^2 + z^2)^{1/2} , \qquad (3)$$

where s and z are equatorial and meridional reciprocal distances, respectively. The powder diffraction intensities are (relatively) stronger for peaks that are closer to the reciprocal center (small r) and broader azimuthally. Moreover, the resolution of the powder diffraction is better than the fiber diffraction.

It was reported earlier [41] that the monoclinic peak starts decreasing in intensity at about 363 K. The shape of the orthorhombic peak 200 which overlaps the monoclinic peaks 200 and $\bar{2}10$ becomes more perfect (see Fig. 5.5-3) as the monoclinic peaks weaken. In addition, the perfection of the orthorhombic peak shape and their increase in intensity are due to the perfection of the crystals as temperature increases.

Figure 5.5-5 illustrates the powder patterns of PE-I on heating, melting, and after recrystallization. Optical microscopy revealed that the fibers undergo shrinkage at 418 K (curve A). Most of the orthorhombic diffraction has disappeared at this temperature and a weak, broad, hexagonal 100 reflection, centered at $2\theta = 20.5°$ appears, as the intensity of the amorphous halo has increased. At 423 K (curve B), the intensities of the orthorhombic 110 and 200 peaks have further decreased. At 429 K, only the amorphous halo remains

(curve C). The much stronger hexagonal diffraction that has been reported when heating constrained UHMMPE fibers [41] is, thus, not observed in this experiment without constraint. On slow cooling of the molten PE-I, only the orthorhombic diffraction returns, superimposed on a remaining amorphous halo (curve D). The mechanisms of these phase transformations are discussed below.

5.5.3 Small-angle X-ray Scattering

The SAXS patterns of samples PE-II, PE-III, and PE-IV are shown in Fig. 5.5-6. There are weak peaks at the positions equivalent to a long period about 35 nm for PE-II and PE-IV samples, in the typical range of long periods in PE fibers [26,130-133]. Sample PE-III shows practically no long period. Usually, the long period results from the alternating of lamellar crystals and noncrystalline domains [131]. The intensity of the SAXS peak of PE fibers usually decreases with an increase of draw ratio, while the long period stays approximately constant because an increasing draw ratio leads to an increase of extended chains as a result of the unfolding of lamellar crystals [131,134].

The SAXS patterns of PE-I and PE-V are shown in Fig. 5.5-7. There are two SAXS peaks for these fibers. They are located at long periods of about 6.0 and 4.2 nm in PE-I, and of about 5.0 and 2.5 nm in PE-V (the latter is the second order peak of the former). These long periods are extremely short for PE fibers. Such small values of long period have only once been reported before for a commercial high-modulus Tekmilon PE fiber [127,135] (made by Mitsui

Petrochemical Co., initial modulus 100 GPa, tensile strength 2.5 GPa) which may be similar to sample PE-V of this study (compare Fig. 5.5-7B and Figs. 1 and 2 of reference [133]). Five orders of the 5 nm SAXS peaks were observed for this fiber [135] with intensities of the odd order peaks being stronger than that of the even order peaks. It was suggested that the small values of the long period result from a shish-kebab structure [127]. This explanation was challenged since shish-kebab structures are not observed in high-draw-ratio PE fibers [135]. It was then proposed that the long period may result from an inclusion of crystalline calcium stearate (used as stabilizer);for the SAXS pattern of the fiber is similar to that of the stearate, and there is 0.076% of Ca, w/w in the Tekmilon PE fibers that could yield 1.3% stearate. It is, however, not clear why the small long period is not observed for any of the other PE fibers. They contain aluminum stearate and are also highly extended [135].

The SAXS pattern of PE-I (Fig. 5.5-7A) is different from that of PE-V (Fig. 5.5-7B). The intensity of the second SAXS peak of PE-I is stronger than the first peak. The position of the second peak, (4.2 nm) is not at half the value of the first (at 6.0 nm). Furthermore, the shape of the second peak is not symmetric, implying that the peak may result from an overlap of more than one peak. There may be at least two sets of long periods in PE-I. The causes for the SAXS peaks of PE-I and PE-V may be different. Consequently, the SAXS peaks of the PE-I fibers cannot be caused by added stearates since it was confirmed by the manufacturer that there is no calcium stearate in sample PE-I [136]. The stabilizer added is a mixture of Irganox® 1010 (CIBA-GEIGY) [2,2-bis[[3-[3,5-

bis(1,1-dimethylethyl)-4-hydroxy phenyl]-1-oxopropoxy]methyl]-1,3-propanoate propanediyl]3,5-bis(1,1-dimethylethyl)-4-hydroxybenzene] and Irgafos® 168 (CIBA-GEIGY) [2,4-bis(1,1-dimethylethyl) phenyl-phosphite (3:1)]. The longest dimension of the molecules of these antioxidants is shorter than 3 nm. Furthermore, SAXS experiments were performed with the pure stabilizer in a powdery state and showed no low-angle peak.

Figure 5.5-8 shows SAXS patterns of two annealed PE-I samples at 393 K (a) and 421 K (b) for 10 minutes with fixed ends. Their SAXS peaks appear still at the same positions, but the peaks are sharper. Annealing usually enhances the SAXS of semicrystalline fibers by perfection and further growth of the crystallites. Fast quenching by using liquid nitrogen or slow cooling does not make any significant difference on the SAXS patterns. If the SAXS peaks of PE-I fibers result from the alternative arrangement of small crystallites and amorphous phase along the fiber axis, such small crystallites should have melted during the annealing. The melting point of crystallites of a size smaller than 6.0 and even more so of 4.2 nm is less than 392 K [2], and crystallites that form on cooling are not likely to have such a small size [137]. It is interesting to note that for PE-IV a weak SAXS peak appears at 6 nm on annealing, although it had no such peak before annealing (Fig. 5.5-6).

Figure 5.5-9 shows the SAXS patterns from the pellets of randomly oriented short pieces of PE-I and the recrystallized PE-I and PE-V. The SAXS peaks can still be recognized with the randomly oriented PE-I and the recrystallized PE-V, although no SAXS peak exists for the recrystallized PE-I.

This indicates that the SAXS peaks of PE-I are specific to the fiber, while the SAXS peaks of the PE-VI are not necessarily specific to the fibrous state.

It was shown that the crystals of the fibers were orthorhombic with only small amounts of the monoclinic polymorph. The minimal contribution to small-angle X-ray diffraction peaks could only be interpreted as a very small fraction of lamellae of unique thicknesses. In addition to the crystals, an intermediate phase could be identified. The intermediate phase is highly oriented and between the mobility of crystalline and amorphous polyethylene. Finally, a small amount of random amorphous material was detected.

In the traditional analysis method, one makes use of a single point to represent a diffraction peak. In the full-pattern method, each reflection is treated as a complete two-dimensional peak. The positions, intensities, and two-dimensional profiles of the reflections are used to characterize the parameters of the crystal structure and its defects, as well as the crystallite morphology. Thus, difficulties such as overlap of reflections are resolved and permit an accurate description of the structure of the crystalline phase. More importantly, the full-pattern fitting of the crystalline diffraction makes it possible to also study the noncrystalline material. By subtraction of the crystal scattering from the total fiber-diffraction pattern, the remaining noncrystalline scattering pattern is found. It is not that of an isotropic, amorphous phase that would be expected from the two-phase model. This observation led to a second separation by removing all liquid-like scattering. The remaining diffraction pattern is that of the intermediate phase. Its molecules are partially oriented in direction of the fiber axis.

The full-pattern analysis of fiber X-ray experiments yields, thus, a quantitative structure resolution into crystals, oriented intermediate phase, and amorphous isotropic phase.

5.6 NMR

The ^{13}C CP-MAS NMR spectra of samples PE-I and PE-IV are shown in Fig. 5.6-10. Three components can be directly recognized. The major peak at 32.0 ppm has been assigned to the orthorhombic crystals [30]. The resonance at 33.3 ppm, about 1.5 ppm down-field, has been identified as the contribution from the monoclinic phase [138,139]. It is characteristic of all-*trans* chains with parallel zig-zag planes. The amorphous resonance phase appears at 30.2 ppm, but it is very weak for sample PE-I. A three-peak fitting of the ^{13}C CP-MAS spectrum for PE-I is illustrated in Fig. 5.6-1.

Spin-lattice relaxation times T_1 were determined for PE-I and PE-IV. The peak at 32.0 ppm has two components of largely different mobility [25,30]. It is, therefore, not suitable to assign this peak solely to the orthorhombic phase. Only the part of lesser mobility results from the orthorhombic phase. The higher-mobility part is contributed by the intermediate phase with a similar chain conformation. The mass fractions for two phases could be separated by fitting the relaxation time T_1 by a sum of two exponentials as discussed in Ref. [25]. The mass fractions of all four components are given in Table 3 and their

relaxation times, in Table 5.6-4. A T_1 analysis of the monoclinic peak is not possible because of the small mass fraction.

Multiple-temperature ^{13}C NMR CP-MAS spectra of PE-I are shown in Fig. 5.6-2. The monoclinic resonance at 33.3 ppm becomes weaker at 363 K, while the orthorhombic peak (32.0 ppm) still exists with an up-field shift of 0.2 ppm due to an intermolecular packing change with temperature. At 423 K, a strong, sharp peak appears at 29.3 ppm due to melting. It is interesting to see that there is still a peak at 31.5 ppm (corresponding to an all-*trans* chain) at 423 K. The intensity of this peak is comparable to the isotropic peak. At 433 K, only the isotropic peak remains.

As it has been reported previously [140,141], the relaxation times of the intermediate phase may be further separated into two or more components. For example, 80% of the intermediate phase of the PE-I fiber has a T_1 of 61.4 s and the remaining 20% have a T_1 of 2.3 s. It is, however, difficult to fix the number of components based on fitting of the relaxation decay curves alone. More components naturally lead to better fitting. In addition, each component may also have a distribution of relaxation times, further complicating the analysis. From the NMR experiment one can, however, conclude with certainty that the peak found at the position of the orthorhombic crystalline phase has at least two oriented components with different relaxation times. The details of the structures of these components, and their arrangement in the fiber can only be understood by combining the NMR results with those from the other techniques.

5.7 Density

The densities of the four UHMMPE fiber samples (ρ) are listed in Table 1, together with the mechanical properties, provided by the supplier of the samples. The crystallinity, also listed in Table 1, is computed from the standard two-phase model [2]:

$$w_c = \frac{\rho_c}{\rho}\left(\frac{\rho - \rho_a}{\rho_c - \rho_a}\right), \qquad (4)$$

in which the crystal density ρ_c and the amorphous density ρ_a are treated as constants (crystal density 0.997 Mg/m^3, amorphous density 0.854 Mg/m^3) [2]. As expected, the density crystallinities do not correlate with the mechanical and thermal properties of the fibers. The main reason for this disagreement is the incorrect assumption that all of the noncrystalline material of the PE fiber is amorphous. It is well known that the density of the noncrystalline material of PE changes with the processing history [142].

Chapter 6

Discussion

The discussion of the experimental results focuses on a new model for the phase behavior of gel-spun UHMMPE fibers. The combination of the thermal analysis, x-ray scattering, and NMR data shows conclusive evidence for a phase structure with a minimum of three phases. The crystalline phase with three dimensional long range order, an intermediate, oriented, mobile phase and a small amount of amorphous material are nano-phase separated to form one of the strongest and most versatile fibers.

The discussion will offer a general assessment of the two-phase model, the improvements by the three-phase descriptions, and some remaining open questions. First, the limits of the two phase model are briefly summarized. This is followed with analyses of the crystal structure parameters, crystallinities, orientation functions, fractions of taut tie molecules, and SAXS results. Then a new fiber-structure model is proposed and some structure-property relations are presented.

6.1 Heat Capacity of Fibers

The heat capacities of the fibers show a glass transition between 180 and 290 K, and a region of increased heat capacity prior to melting which is reversible. This reversible increase in heat capacity may be due to the fact, that the large number

of non-crystalline but oriented molecules have a higher mobility, yet are not free to rotate about their entire axis. The motion has to be of an oscillatory nature, which is associated with an increase in heat capacity due to large amplitude vibrational motion. Measurements of heat capacity on drawn and undrawn PE fiber samples were recommended already by Peterlin [32] in 1965 in order to understand the energetic origin of the discrepancies in properties of drawn from undrawn PE samples.

The increase in heat capacity of the fibers in the temperature range of 175 to 400 K, going ultimately beyond the extrapolated liquid/melt PE heat capacity is an indication that the events occur reversibly. Whether this is due to a latent heat effect, occurring reversibly, or a gain in heat capacity is not easy to determine. However, it is clear that no non-reversible effects such as annealing to larger crystals can happen. If this were the case, the perfected crystals would have a higher melting point, which in turn would lead to an overall decrease of the heat capacity in the following experiments on the same sample. No such effect was observed however.

The possibility of a reversible melting (local melting of a crystal) and recrystallization of the very same, randomized PE material into a crystal with the identical properties is however questionable. At this moment, it looks as if the intermediate non-crystalline fraction of the gel-spun UHMMPE fiber had a continuous gain in mobility in the range of 200 to 300 K similarly to the amorphous PE but with much smaller amplitude. The end of this increase at 300 K is followed by an increase in heat capacity similar to the increase in heat

capacity of the crystal. At 370 K the increase in heat capacity for the intermediate non-crystalline material is again larger than the increase in heat capacity for the fully crystalline, thereby indicating an early disordering for the intermediate fraction.

With these findings a glass transition as well as a heat of disordering for the intermediate non-crystalline fraction have to be assumed. The glass transition corresponds cooperative gain in mobility of the $(-CH_2)$- beads in the plane perpendicular to the fiber axis. Since the order in the fiber axis is only partially destroyed, the disordering of the intermediate non-crystalline fraction needs to be associated with an entropy, and hence enthalpy, of isotropization. For this reason, any report of a crystallinity value for the UHMMPE fibers is questionable. The heat of isotropization of the mesophase must be established first.

6.2 Melting

The sharpness of melting has been explored with the use of heating rates of 10 K/min for the very small samples. The experiments indicate a very sharp melting at 416 ±1 K for the onset and a peak width of about 2 K at half of the peak height (FWHM) for all the sub-microgram samples. The sharpness of this transition is contrary to most of the published data on the first order phase transition of UHMMPE fibers. However, it does correspond well with the concept of the melting of a metastable state. The oriented intermediate material is held only by

the "hard segments" of the crystallites. As soon as these crystallites melt, the release of the stored energy further contributes to the collapse of the system. It should be noted that the onset of isotropization occurs above the equilibrium melting point of the extended chain polyethylene crystal. The influence of superheating has to be investigated for a definitive answer. In addition, the persistence of birefringence in the fiber and the detection of residual order by x-ray measurements beyond this transition requires further work.

6.3 Fiber structure

Many of the seven methods of fiber analysis and a considerable number of reports in the literature are in agreement with the existence of two crystalline phases (orthorhombic and monoclinic) and two noncrystalline phases (intermediate and amorphous) in the UHMMPE fibers at room temperature. The division between the crystalline and noncrystalline phases rests with the criterion of three-dimensional ordering. In this discussion, an attempt is made to reach a unique structure model for UHMMPE fibers that is in accord with all measurements.

6.3.1 Orthorhombic crystals

The orthorhombic crystals are the major component for all analyzed samples (see Table 3). The structure and the morphology of this phase is accurately determined by the full-pattern fiber x-ray diffraction method (see Table 2). There

are two basic macroconformations for the orthorhombic crystals, one is the folded-chain, the other the extended-chain macroconformation [2]. For high-modulus fibers most of the orthorhombic crystals need to be in the extended-chain macroconformation. The appearance of the weak SAXS peak of a regular long-period of 35 nm indicates that there may still be some fraction of folded-chain crystals in samples PE-II and PE-IV.

The orthorhombic crystals show small changes with processing history (Table 1). A similar change in crystal parameters with processing was also discovered in PET fibers [14,17,129], . The crystals were not grown under equilibrium conditions and remain metastable. The strains that keep the crystals metastable should ultimately be assessable by the variation in lattice parameters. It is interesting that the most perfect crystal (PE-IV) does not yield a better fiber when considering the mechanical properties. The crystals of PE-IV are more closely packed (smaller unit-cell volume, Table 1) and have a much lower mobility (Table 4) than those of sample PE-I. Nevertheless, the mechanical properties of PE-IV are worse than those of the PE-I fibers (see Table 1). It may even be generally valid for this type of PE fibers that the better mechanical properties are obtained from less perfect crystals. The reason behind this correlation is that one has to apply more external stress to reach a higher draw ratio, and a higher draw ratio leads to less perfect crystals.

The mass fraction of the orthorhombic phase can be estimated from the ratio of the integrated intensities of the crystalline diffraction pattern and the total observed fiber pattern. The intensity ratios for samples PE-I and PE-IV lead to

67% and 75% crystals, respectively, this is the same magnitude as found by NMR, but in reverse order (see Table 3). The crystallinities calculated from the fiber densities (Table 1) and the heats of fusion are, however, distinctly higher. They are based on the two-phase model and signify a higher density and lower enthalpy of the intermediate phase than the amorphous phase.

Despite the possibility of tracing the fiber processing history through differences in the orthorhombic crystal structure, fiber properties do not parallel the crystal structure. This lack of functional relationship of orthorhombic crystal structure and two-phase crystallinity with fiber properties has been the biggest hindrance in the application of x-ray diffraction and many of the other analytic techniques when applied to fiber characterization and quality control.

6.3.2 Monoclinic Crystalline Phase

The amount of monoclinic crystals is much smaller than the amount of orthorhombic crystals (Table 3). The monoclinic structure is, however, not distributed as a thin layer on or between the surfaces of orthorhombic crystallites. This would cause broader monoclinic reflections than observed. The powder diffraction and solid state NMR show that the intensity of the monoclinic signals in the original fibers decreases above 360 K (Figs. 5.5-3 and 5.6-3). This heating behavior agrees with the earlier reports [10,41,143]. Once the monoclinic crystals disappears, either by annealing at 421 K or by complete melting of the fiber, they cannot be brought back by recrystallization. It is clear that the monoclinic phase of PE is not thermodynamically stable. Calculations

based on intermolecular energetics also suggest less stability of the monoclinic phase at almost the same packing density as the orthorhombic crystals [2], although opposite results were also reported [144].

Since the amorphous phase signals in both, powder x-ray diffraction and solid state NMR do not show an observable increase on disappearance of the monoclinic phase, and no endotherm is visible by DSC (Fig. 5.2-1), the monoclinic phase appears not to melt. Usually it is assumed that the monoclinic domains transform to the orthorhombic phase by rotation of the chains [10,143]. The disappearance does however correspond to the onset of the isotropization at about 370 K of the intermediate phase as determined from the precision heat capacity data.

Even though the monoclinic crystalline phase is not stable, it is often detected in PE fibers. Compression of the UHMMPE fibers laterally, furthermore, increases the mass fraction of the monoclinic phase (see Figs. 5.5-3 and 5.5-4). The transformation of the orthorhombic to monoclinic phase by lateral pressure to the molecular axis has been observed frequently [10,113,114,143-147]. The compression experiment of this study shows that only a limited fraction of the fiber can transform. The mass fraction of the monoclinic phase is approximately doubled after the compression. Also it is reported that even higher pressures cause only partial conversion of the orthorhombic phase [144]. It is not fully clear which part of the fiber transforms into the monoclinic phase. In the present examples, the ultimate mass fraction of the monoclinic phase is about 20-25%, *i.e.* it reaches the combined initial monoclinic and intermediate phase fraction. A

further study of the initial and compressed samples by multiple-temperature powder x-ray diffraction, and solid state NMR is necessary to find the influence of the intermediate phase in the transformation to and from the monoclinic phase.

6.3.3 Intermediate Phase

To clarify the nature of the intermediate phase, it is necessary to summarize the structural features obtained from the various experiments: 1.) The molecular chains of the intermediate phase have a *trans-conformation* and are oriented preferentially parallel to the fiber axis. 2.) Since the observed x-ray scattering (Figs. 5.5-2) and the NMR signal (Fig. 5.6-2) cannot be produced by isolated chains, its chains must be collected in domains *(micro- or nano-phases)*. 3.) The *axial distances* between layers of neighboring C-atoms of the intermediate phase are sufficiently similar to the crystal to cause the overlap with the 002 crystal diffraction. 4.) The *lateral packing*, on the other hand, is not that of a crystal. A reliable full intermediate phase diffraction pattern as could be established for PET [17] was, however, not obtained because of the additional presence of the monoclinic crystals. 5.) The *mobility* of the chains in the intermediate phase is much higher than in the orthorhombic crystals but less than in the amorphous phase (see Table 4). 6.) A possible *heat of fusion* of the intermediate phase must be rather small. The weight fractions of monoclinic and orthorhombic crystals are expected to be equal to the crystallinity by DSC. With the need for a transition enthalpy for the intermediate non-crystalline fraction, the entire concept of fiber crystallinity needs further analysis. This is especially true since a

compensation of endothermic effects expected from randomizing trans chains (intramolecular heat of fusion) and exothermic strains necessary to maintain a mobile, metastable state may cancel each other out.

The concept of the intermediate phase is different from that of a taut tie-molecule, TTM, although both contain oriented, noncrystalline chains. The main difference is that the intermediate phase is an assembly with coherent axial atomic positions, while TTMs are believed to consist of individual, uncorrelated chains. The mass fraction of the former can be determined by x-ray structure analysis by the full-pattern method and solid state NMR, while the mass fraction of the latter has only been derived from the calculation of mechanical properties. The intermediate phase contributes significantly to some of the crystal diffraction, while scattering of a TTM could not contribute to any sharp diffraction peak.

The structure of the intermediate phase of the UHMMPE fibers is somewhat different from that of the earlier analyzed, less drawn PET fibers [14,17]. In contrast to PE, the intermediate phase of PET is far from fully oriented parallel to the fiber axis, and its orientation increases with draw ratio. In fact, the degree of orientation was the major factor determining modulus and tensile strength of the PET fiber [14] . The phenylene rings of the neighboring chains of the intermediate phase of PET fibers were orienting parallel to each other. It was thus possible to produce also strong equatorial scattering peaks. The planes of the neighboring chains of the intermediate phase of PE fibers seem not to be parallel to each other nor do they have a regular spacing, so that there are no visible equatorial scattering peaks.

Since the polymer chains of the intermediate phase can orient well along the fiber axis, the intermediate phase may be considered to be a disordered crystal with large atomic temperature factors. This was the reason for the significant improvement in fitting of the x-ray pattern with the earlier disorder model in PE-I [23]. The large temperature factor does, however, not only result from the positional disorder, assumed before, but also from the higher mobility of the atoms in the intermediate phase found by NMR. Due to the fact that all the experiments were performed at room temperature, where the glass transition of the intermediate fraction is already complete and the introduction of gauche defects dominates the increase in heat capacity, further x-ray diffraction and NMR studies in the low temperature range (preferably below 200 K) are recommended.

In the light of the additional experiments, the new multi-phase model is capable of a better explanation of the fiber properties. The mass fraction of the intermediate phase is difficult to estimate by x-ray diffraction. The sums of the fractions of the intermediate phase, the monoclinic phase, and the amorphous phase are 25 and 33% for samples PE-I and PE-VI, respectively, agreeing approximately with solid state NMR (see Table 3). Strong intermediate phase scattering peaks are, however, only observed with PE-I. This suggests that the intermediate phase in sample PE-I is better oriented. The mass fraction of the intermediate phase could, thus, not be separated from the fiber diffraction data of this study. It should also be pointed out that the separation made between crystalline and the intermediate phases is somewhat different for the two

methods. The x-ray diffraction is based on three-dimensional ordering, while NMR is based on mobility. If the mobility of some of the intermediate phase as defined by x-ray becomes as low as in the orthorhombic phase, the intermediate phase appears crystalline in NMR, and *vice versa*. The estimate of the true mass fraction of the intermediate phase is thus still in doubt. At the moment the use of the heat capacity data for the quantification of the different mass fractions is not possible since neither the heat of isotropization nor an increase in heat capacity due to the mesophase glass transition has been established.

Additional information can often be derived from the Bragg peaks of SAXS that develop when there are regularly alternating domains of higher and lower electron density. This *long period* is assumed to be the sum of the lengths of these two domains. For PE-III there is no low-angle peak (see Fig. 5.5-6), *i.e.* the electron density shows no regular fluctuations. For PE-I and PE-V, the weak low angle spacing (see Fig. 5.5-7) is less than the axial coherence length of the orthorhombic crystals (see Table 2). For these fibers, the usual assumption that the low angle spacing indicates regular, alternating orthorhombic crystalline and amorphous phases can not be valid. Other density- fluctuations must cause the scattering. An estimate of the amount of material in the sample that contributes to the small angle peaks is only about 1% (by evaluation of the invariant integral [148]). For PE-II and PE-IV, the low angle spacings of about 35 nm are sufficiently above L_3 (see Table 2) not in contradiction to regular interruptions of orthorhombic crystals by the amorphous phase (see Table 2 and Fig. 5.5-6), but the amount of material contributing to the low-angle pattern is only 10%, *i.e.* this

structure feature could also arise from the monoclinic phase (see Table 3). The correlation of the 1% material contributing to the small angle peaks, and the maximum of 3% amorphous detected from NMR experiments needs to be investigated.

A long period of several hundred nm was observed for fibers similar to PE-I and PE-III [126,149] and other high-modulus PE fibers [126]. This long period may be related to the length of the intermediate phase.

Overall, the SAXS patterns of the fibers are, at present, less informative than for bulk samples. Due to the high draw-ratio in the present samples the regular alternation of dense crystals and of the less dense amorphous phase is lost. The remaining pattern may be processing dependent, but it is not fully resolved in that which component of the fiber gives rise to which SAXS peak.

6.3.4 Amorphous Phase

With respect to the x-ray diffraction technique, the amorphous phase is defined as an assembly of randomly oriented chains. None of the four UHMMPE samples which are studied by the full-pattern method show any significant intensity of the amorphous halo at room temperature (see Fig. 5.5.1). This agrees with the small fractions of the amorphous phase determined by solid state NMR (see Table 3). The 3% amorphous phase found in PE-I may be mainly located on the surface of the fiber or in sites of defects. For PE-IV, some of the 10% amorphous phase may form amorphous domains between the (not as well) oriented intermediate phase, reducing the mechanical properties of the fiber.

The interpretation of the fiber heat capacity measurements supports the evidence of negligible amorphous contribution. For PE-IV / PE-VI, the distinction between the glass transition of the intermediate and of a truly amorphous material is however questionable.

The amorphous phase defined by solid state NMR and x-ray analysis is different from the amorphous phase calculated from density using the two-phase model. For example, the mass fraction of the amorphous phase based on fiber density of PE-I is much higher, about 20%. The over-estimate is caused by ignoring the presence of the intermediate phase.

6.3.5 Fiber Structure Model

Based on the analysis of the structures of the various phases and the experience with the much less drawn PET [14], a structure model for the polyethylene fibers is proposed in an attempt to reconcile the experimental results. The schematic of this structure model is shown in Fig.6.1-1. In PET, the C-domain represents most of the crystalline phase, periodically interrupted by amorphous area A. The interface between C and A contains all chain folds, chain ends, and tie molecules, and the amorphous area is, in total, less oriented than the intermediate phase. Area B is representative of the intermediate phase, which is held in its metastable state by connections to the crystals in phase C and additional, imbedded crystals. Some amorphous inclusions are also in area B, but without regular spacing. Because the whole structure is kept in the metastable state by the crystals, the other phases (nanophases) can be

considered to be three-dimensional defects (also called amorphous defects in unoriented systems) [2]. The geometry of partition of the fiber shown in Fig. 6.1-1 is chosen for the estimation of mechanical properties and needs further information for the expansion to fiber dimensions. Also the mass fractions are at present only approximate.

In the gel-spun UHMMPE fibers the overall orientation is considerably higher than in melt-spun fibers. The amount of chain folding is much less, but some of the regular stacking of A/B remains. Phase A is more oriented than for PET but still less oriented than B. The very small amount of truly random PE detected by NMR is distributed between A and B. It is not clear at present where the monoclinic crystals are located (B or C, or both). The axial length and perfection of the B area may span several A/B sequences and depend on the original amount of entanglement and processing condition. The lateral packing of the intermediate phase in B is largely incoherent, but crystals with coherent lateral packing exist in the overall area B to maintain the metastable structure. The intermediate phase has, as in PET, a mesophase structure.

6.3.6 Mechanical Properties

The mechanical properties of PE fibers can be discussed on hand of the structure model shown in Fig. 6.1-1 and are described by the scheme of Takayanagi [22,23]. The modulus of the fiber is given by:

$$E_{fib} = w_B E_B + \frac{w_C + w_A}{\frac{w_C}{E_C} + \frac{w_A}{E_A}} \quad (5)$$

with w representing the weight fractions and E the moduli of the appropriate domains A, B, and C. The modulus of the B-domains can be approximately represented by:

$$E_B = E_{cryst} f_{int}, \quad (6)$$

where f_{int} is the orientation function of the B-domain, and E_{cryst} is the PE crystal modulus, approximating the modulus of the fully oriented intermediate phase in the present case. The modulus of the domain A, can also be approximated by:

$$E_A = E_{cryst} f_A (\Delta x_{max} - \Delta x), \quad (7)$$

where f_A is the orientation function over the chains in the A-domain, Δx is the fiber elongation, and Δx_{max} is the maximum elongation of the domain A at break.

Since the intermediate phase of PE-I sample is highly oriented, f_{int} may be close to 1. The f_A of PE-I is also expected to be high since there is almost no randomly oriented amorphous phase in the domain A. This makes the initial modulus of PE-I fiber (179 GPa) close to the theoretical limit of the crystal that is reported to fall between 210 and 350 GPa [86-90]. The orientation of the intermediate phase of PE-IV is lower than that of PE-I, and it also contains more

amorphous phase which reduces the orientation (lower value of f_A). The initial modulus of PE-IV (59 GPa) is thus much lower.

Even though the initial modulus of PE-I approaches the maximum possible, the tensile strength of the fiber (3.9 GPa) is much less than the theoretical strength of about 35 GPa [91,92]. The Δx_{max} of the A-domain of high f_A may not be reached simultaneously by the whole domain which leads to sequential breaking of chains. After elongation beyond Δx_{max}, the B-domain becomes the major load-bearing component in the fiber. The tensile strength is, therefore, determined largely by the B-domain. For PE-I the mass fraction of the B-domain is only about 13%, resulting in the much weaker fiber. The tensile strength of the B-domain was shown when analyzing PET [25] to depend also on the orientation. The better the initial orientation, the greater is the number of the fully extended chain molecules at break. As is discussed above, the intensity ratio of the central layer of 002 and 110 diffraction peaks of the WAXS pattern can be used to approximate the average orientation function of the B-domain. For the fibers of this study, the order of the intensity ratios is 3.0, 1.4, and 1.1 for PE-I, PE-III, and PE-IV. This agrees with the order of the corresponding tenacities (see Table 1). The intensity ratio for PE-V is 1.4, similar to that of PE-III. The fiber tensile strength of PE-V is, thus, expected to be also similar to that of PE-III.

Importantly, a small and well oriented A-domain is, therefore, necessary in order for a fiber to have a high initial modulus. It is reported that on annealing with fixed ends at temperatures close to the first endotherm the initial modulus

decreases, but the tensile strength stays almost constant [93]. Annealing at such temperatures can increase the size and reduce the orientation of the A-domain by melting and recrystallization, avoiding strained A-domains. This would explain the decrease of the initial modulus, and as long as the mass fraction and orientation of the B-domain is not affected, the fiber tensile strength can stay constant.

The splitting of the 002 diffraction peak after certain percentage of strain [7,8] can also be explained by the proposed structure model. In the initial stage the stress applied on both C-domain and B-domain is the same, which results in one 002 diffraction peaks. As the fiber elongates, E_A starts to decrease and the B-domain becomes the primary load-bearing component. The strain of the B-domain becomes greater than the strain of the C-domain, which leads to larger (004) distances of the B-domain than in the C-domain. This results in the splitting of the 002 diffraction peak. A similar mechanism can also be used to interpret the two load-bearing components detected by spectroscopic studies [5-7]. The polymer chains of the B-domain have bigger molecular strain, while the polymer chains of the C-domain have a smaller strain. Since the lateral diffractions 110 and 200 result mainly from the C-domain, and since the deformation of domain C is less than that of the domain B, the lengths of crystal *a* and *b* axes do not change much on increasing fiber deformation.

6.4 The Model of Takayanagi

The model of Takayanagi uses the taut tie-molecule concept and requires only that there are noncrystalline, interfibrillar chains with some preferential order in direction of the fiber axis. Our new, intermediate phase is defined as just such noncrystalline material and avoids the inconsistencies of requiring an amorphous phase with orientation.

The structure of the intermediate phase is not the same as that assumed for the taut tie molecules. The orientation functions of the intermediate phases of the four analyzed samples are considerably smaller than those of the crystalline phases (*i.e.* the molecules are far from taut). The mean-square cosines of the angles between the chains of the intermediate phase and the fiber axis, $\langle\cos^2\phi\rangle$, are 0.64-0.70. There should also be some isotropic (amorphous) material between the intermediate phase domains of different orientations to permit space-filling packing. Similar to the average orientation function of the fiber, an average orientation function of the intermediate phase is defined by:

$$f_{av,in} = IIF_{in} \times f_{in} . \qquad \textbf{(8)}$$

The length of the molecules of the intermediate phase is probably also of importance for the evaluation of the ultimate strength, but is not considered in Eq. (8).

** ** ** **

The new, three-phase structure analysis can detect differences not seen by the two-phase model. The ultimate goal is to combine all the information, from manufacturer and polymer physicists, to finally understand all the steps in the processing-structure-property relationship.

Chapter 7

Conclusion

At room temperature, the UHMMPE fibers consist of orthorhombic and some monoclinic crystals, intermediate and amorphous phases. In the melting range, the hexagonal phase of PE may become of importance. The orthorhombic crystal parameters give an indication of fiber processing history. The intermediate phase has crystalline ordering along the fiber axis, but not laterally. It is held in its metastable mesophase structure by lateral attachment to stacks of crystals (A/C) and imbedded, uncorrelated crystals. The mobility of the chains of the intermediate phase is higher than that of the orthorhombic crystals by about one order of magnitude, and lower than that of the amorphous phase, also by about one order of magnitude. Under pressure more monoclinic crystals are formed, perhaps from the intermediate phase. On annealing above 360 K, the monoclinic phase converts to orthorhombic. This transition occurs at the same temperature at which the onset of isotropization can be seen in the heat capacity. The thermal analysis of shrinkage, heat capacity, and melting transition confirms the nano-phase separated nature of the UHMMPE fibers. Only a nano-phase separated structure breaks down simultaneously in both the crystalline and the non-crystalline phase. This property is due to the connectivity of macromolecules crossing the phase boundaries.

In combination with the NMR and x-ray results, the determination of heat capacities, melting behavior, and the fiber shrinkage allows to arrive at an overall model for the UHMMPE fibers.

Chapter 8

Proposed Continuation Of The Research

The results presented in this thesis indicate that a new model needs to be developed to replace the determination of crystallinity from the equilibrium melting of polyethylene. Therefore, the determination of the theoretical enthalpy of transition for the mesophase isotropization should be undertaken.

Since heat capacity measurements of the UHMMPE fibers have been shown to be measurable with sufficient precision. The next step has to be the application of this knowledge towards the ultimate goal of establishing the processing - structure - property relationship. To achieve this goal, a closer collaboration between manufacturers, textile science, materials science and basic polymer physics is required.

References

References

1. Wunderlich B. Macromolecular Physics, Volume 3: Crystal Melting. New York: Academic Press; 1980;
2. Wunderlich B. Macromolecular Physics, Volume 1: Crystal Structure, Morphology, Defects. New York: Academic Press; 1980;
3. Wunderlich B. Macromolecular Physics, Volume 2: Nucleation, Crystallization, Annealing. New York: Academic Press; 1976;
4. Polymer Science and Engineering, The shifting Research Frontiers. Washington, D.C. National Academy Press; 1994;
5. Hearle JWS. Polymers and their properties Volume 1: Fundamentals of structure and mechanics. New York: Wiley; 1982; 1p.
6. Morris PJT. Polymer Pioneers. Philadelphia: The Beckman Center for the History of Chemistry; 1989;
7. Natta G, Corradini P. J Polymer Sci 1956;20:251
8. Smith, P., Lemstra, P.J., and Pennings, A.J. inventors. GERMANY. 30 04 699. 1980;
9. Prevorsek DC. Preparation, Structure, Properties and Applications of Gel-spun Ultrastrong Polyethylene Fibers. Trends in Polymer Science 1995;3(1):4-11.

10. Seto T, Hara T, Tanaka K. Phase transformation and deformation processes in oriented polyethylene. Japanese Journal of Applied Physics 1968;7:(1)31-42.

11. Keller A. A unifying scheme for polymer crystallization with wider implications for phase transformations. NATO-ASI Series C: Mathematical and Physical Sciences 1993;405:1-16.

12. Murthy NS, Correale ST, Kavesh S. Structural changes prior to melting in extended chain polyethylene fibers. Polymer Communications 1990;31:(2)50-2.

13. Wunderlich B, Möller M, Grebowicz J, et al. Conformational Motion and Disorder in Low and High Molecular Mass Crystals. Adv Polymer Sci 1988;87:

14. Fu Y, Annis B, Boller A, et al. Analysis of Structure and Properties of Poly(ethylene terephthalate) Fibers. J Polymer Sci , Part B: Polymer Physics 1994;32:2289-306.

15. Fu Y, Busing WR, Jin Y, et al. Poly(ethylene terephthalate) Fibers 1. Crystal Structure and Morphology Studies with Full-pattern X-ray Diffraction Refinement. Macromolecules 1993;26:2187-93.

16. Bunn CW. Trans Faraday Soc 1939;35:482

17. Fu Y, Busing WR, Jin Y, et al. Structure Analysis of the Noncrystalline Material in Poly(ethylene terephthalate) Fibers. Macromol Chem Phys 1994;195:803-22.

18. Immirizi A, Iannelli P. Macromolecules 1988;21:768

19. Iannelli P, Immirizi A. Macromolecules 1989;22:196

20. Iannelli P, Immirizi A. Macromolecules 1989;22:200

21. American Crystallographic Association; 1991 Jul; Toledo, OH. 1991; Full Pattern Rietveld x-ray.

22. Iannelli P. Macromolecules 1993;26:2303

23. Busing WR. X-ray diffraction study of disorder in Allied Spectra 1000 polyethylene fibers. Macromolecules 1990;23:4608-10.

24. Kavesh S, Schultz JM. Lamellar and interlamellar structure in melt-crystallized polyethylene.
1. Degree of crystallinity, atomic positions, particle size, and lattice disorder of the first and second kinds. J Polym Sci A-2 1970;8:243-76.

25. Chen W, Fu Y, Wunderlich B, et al. The morphology of gel-spun polyethylene fibers, investigated by solid state ^{13}C NMR. J Polym Sci , B, Polym Phys 1994;32:2661-6.

26. Zubov YA, Chvalun SN, Ozerin AN, et al. Structural features of highly oriented polyethylene. Polymer Science USSR 1984;26:(8)1979-87.

27. Chvalun SN, Shchirets VS, Zubov YA, et al. Some aspects of one-dimensional diffraction in oriented polyethylene. Polymer Science USSR 1986;28:(1)19-26.

28. Tzou D, Huang T, Abhiraman AS, et al. Two-dimensional ^{13}C NMR studies of the morphology and orientational order in gel-spun ultrahigh molecualr wight polyethylene fibers. Polymer 1992;33:(2)426-8.

29. Kauffman JS, Dybowski C. Determination of transition temperatures and crystalline content of linear high-molecular-weight polyethylene by proton NMR spectroscopy. J Polym Sci , B, Polym Phys 1989;27:2203-9.

30. Cheng J, Fone M, Reddy VN, et al. Identification and quantitative analysis of the intermediate phase in linear high density polyethylene. J Polymer Sci , Part B: Polymer Physics 1994;32:2683-92.

31. Kashiwabara H, Shimada S, Hori Y, et al. ESR Application to Polymer Physics
Molecular Motion in Solid Matrix in which Free Radicals are trapped. Advances in Polymer Science 1987;82:141-206.

32. Peterlin A, Meinel G. Heat content of amorphous regions of drawn linear polyethylene. Polymer Letters 1965;B3:783

33. Arakawa T, Wunderlich B. Thermodynamic Properties of Extended Chain Polymethylene Single Crystals. J Polymer Sci , Part C 1967;16:653-8.

34. Wunderlich B, Czornyj G. A study of equilibrium melting of polyethylene. Macromolecules 1977;10:906-13.

35. Dorset DL, Hu H, Jäger J. Continuous diffuse scattering from polymethylene chains --- an electron diffraction study of crystalline disorder. Acta Cryst 1991;A47:543-9.

36. Jin Y, Wunderlich B. The Heat Capacity of n-Paraffins and Polyethylene. J Phys Chem 1991;95:9000-7.

37. Dosiére, M. editor. The morphology and growth of paraffin crystals with different structures. Kluwer Academic; 1992 Jul 07; AA Dordrecht, The Netherlands. 1993; 345 p.

38. Ungar G, Keller A. Effect of radiation on the crystals of polyethylene and paraffins:

1.Formation of the hexagonal lattice and the destruction of crystallinity in polyethylene. Polymer 1980;21:(11)1273-7.

39. Noid DW, Sumpter BG, Wunderlich B. Molecular Dynamics Simulation of the Condis State of Polyethylene. Macromolecules 1990;23:664-9.

40. Bastiaansen CWM, Lemstra PJ. Melting behavior of gelspun/drawn polyolefins. Makromol Chem ,Macromol Symp 1989;28:73-84.

41. Pennings AJ, Zwijnenburg A. Longitudinal growth of polymer crystals from flowing solutions

VI. Melting behavior of continuous fibrillar polyethylene crystals. Journal of Polymer Science Polymer Physics Edition 1979;17:1011-32.

42. Van Mele B, Verdonck E. Physico-chemical characterization of the fibre/matrix interaction in polyethylene fibre/epoxy matrix composites. Part 1. Characterization with DSC. Composite Interfaces 1995;3:(2)83-100.

43. Kanamoto T, Hoshiba T, Yoshimura T, et al. Melting behavior of super-drawn polyethylene with limiting mechanical properties. Rept Progr Polym Phys Japan 1985;28:227-30.

44. Prevorsek DC, Kip BJ, van Eijk MCP, et al. Molecular deformation of high-modulus polyethylene fibers studied by micro-Raman spectroscopy. Chemtracts - Macromolecular Chemistry 1991;2:282-6.

45. Moonen JAHM, Roovers WAC, Meier RJ, et al. Crystal and molecular deformation in strained high-performance polyethylene fibers studied by wide-angle x-ray scattering and Raman spectroscopy. J Polym Sci , B, Polym Phys 1992;30:361-72.

46. Kip BJ, van Eijk MCP, Meier RJ. Molecular deformation of high-modulus polyethylene fibers studied by micro-Raman spectroscopy. J Polym Sci , B, Polym Phys 1991;29:99-108.

47. Prasad K, Grubb DT. Direct observation of taut tie molecules in high-strength polyethylene fibers by Raman spectroscopy. J Polym Sci , B, Polym Phys 1989;27:381-403.

48. Hattery GR, Hillman MED. ; Baer E, Moet A, editors.High Performance Polymers. Munich: Hanser, 1991;High Performance Organic Fibers for Polymeric Composites. p. 255-78.

49. Barham PJ, Arridge RGC. A fiber composite model of highly oriented polyethylene. Journal of Polymer Science, Polymer Physics Edition 1977;15:1177-88.

50. Dijkstra DJ, Pennings AJ. The role of taut tie molecules on the mechanical properties of gel-spun UHMWPE fibers. Polymer Bulletin 1988;19:73-80.

51. Dijkstra DJ, Pennings AJ. Annealing of gel-spun hot-drawn ultra-high molecular weight polyethylene fibres. Polymer Bulletin 1988;19:481-6.

52. Gibson AG, Davies GR, Ward IM. Dynamic mechanical behavior and longitudinal crystal thickness measurements on ultra-high modulus linear polyethylene: a quantitative model for the elastic modulus. Polymer 1978;16:(6)683-93.

53. Peterlin A. Molecular Model of Drawing Polyethylene and Polypropylene Molecular Model of Drawing Polyethylene and Polypropylene. Journal of Materials Science 1971;6:490-508.

54. Takayanagi M, Imada K, Kajiyama T. Mechanical properties and fine structure of drawn polymers. J Polymer Sci , Part C 1966;15:263-81.

55. Rossignol JM, Séguéla R, Rietsch F. A mechanical model for fibers of linear polyethylenes over a wide range of crystallinities. Polymer 1990;31:1449-55.

56. Wunderlich B. Thermal Analysis. Boston: Academic Press; 1990;

57. Ehrenfest P. "Phase transition types: First, second, third, ... order transition". Proc Acad Sci , Amsterdam 1933;36:153

58. Wunderlich B, Grebowicz J. Thermotropic Mesophases and Mesophase Transitions of Linear, Flexible Macromolecules. Adv Polymer Sci 1984;60/61:1-59.

59. Grey GW. Molecular Structure and the Properties of Liquid Crystals. New York: Academic Press; 1962;

60. Sherwood Ne. The Plastically Crystalline State. Chichester: Wiley; 1979;

61. Tammann G. Der Glaszustand. Leipzig: Leopold Voss; 1933;

62. Wunderlich B. Glass transition of partially ordered macromolecules. Progr Colloid Polym Sci 1994;96:22-8.

63. Vorlaender D. Trans Faraday Soc 1933;29:207

64. Tsuji K, Sorai M, Seki S. Bull Chem Soc ,Japan 1971;44:1452

65. Sorai M, Seki S. Mol Cryst Liq Cryst 1973;23:299

66. Sorai M, Suga H, Yoshioka SH, et al. Mol Cryst Liq Cryst 1980;59:33

67. Sorai M, Suga H, Yoshioka SH, et al. Mol Cryst Liq Cryst 1981;73:47

68. Sorai M, Suga H, Yoshioka SH, et al. Mol Cryst Liq Cryst 1982;84:39

69. Adachi K, Suga H, Seki S. Bull Chem Soc ,Japan 1968;41:1073

70. Adachi K, Suga H, Seki S. Bull Chem Soc ,Japan 1970;43:1916

71. Adachi K, Suga H, Seki S. Bull Chem Soc ,Japan 1971;44:78

72. Haida O, Suga H, Seki S. Chem Letters 1973;79

73. Aglan H, Baer E, Hattery GR, et al. Moet A and Baer E, editors.High Performance Polymers: Structure, Properties, Composites, Fibers. Munich: Hanser; 1991; 1p.

74. Smith, P. and Lemstra, P.J. inventors. US Patent. 4 422 993. 1983;

75. Kavesh, S. and Prevorsek, D.C. inventors. US. 4 413 110. 1983;

76. Archer DG. Thermodynamic properties of synthetic sapphire (α-Al_2O_3), standard reference material 720 and the effect of temperature scale differences on the thermodynamic properties. J Phys Chem Ref Data 1993;22:1441

77. Ditmars DA, Ishihara S, Chang SS, et al. Enthalpy and Heat-Capacity Standard Reference Material: Synthetic Sapphire (α-Al_2O_3) from 10 to 2250 K. J Res Nat Bur Stand (U S) 1982;87:(2)159-63.

78. Cammenga HK, Eysel W, Gmelin E, et al. The temperature calibration of scanning calorimeters
Part 2. Calibration substances. Thermochim Acta 1993;219:333-42.

79. Höhne GWH. Remarks on the calibration of differential scanning calorimeters. J Thermal Anal 1991;37:1987-2000.

80. Höhne GWH, Glöggler E. some peculiarities of the DSC-2/-7 (Perkin Elmer) and their influence on accuracy and precision of the measurements. Thermochim Acta 1989;151:295-304.

81. Höhne GWH, Cammenga HK, Eysel W, et al. The temperature calibration of scanning calorimeters. Thermochim Acta 1990;160:1-12.

82. Wiedemann H, Van Tets A. Thermoanalytical investigations on melting and freezing processes.
Calorimetric calibration of DTA apparatus with metal standards.
Thermochim Acta 1970;1:159-72.

83. Leslie TM. Temperature calibration of a power compensation DSC on cooling. Thermochim Acta 1990;166:309-17.

84. Höhne GWH, Schawe JEK, Schick C. Temperature calibration on cooling using liquid crystal phase transitions. Thermochim Acta 1996;221:129-37.

85. Höhne GWH. Problems with the calibration of differential temperature scanning calorimeters. Thermochim Acta 1983;69:175-97.

86. Vold MJ. Differential thermal analysis. Analytical Chemistry 1949;21:(6)683-8.

87. Boller A and Wunderlich B. The calibration of a modulated differential scanning calorimeter.[Unpublished] 1995;

88. Boller A, Okazaki I, Ishikiriyama K, et al. Determination of Cell Asymmetry in Temperature-Modulated Differential Scanning Calorimetry. J Thermal Anal 1996;submitted:

89. Veeman WS, Menger EM, Ritchey W, et al. Macromolecules 1979;12:924

90. Becker ED. High Resolution NMR. 2nd ed. New York: Academic Press; 1980;

91. Goldman M, Shen L. Phys Rev 1962;128:2024

92. Tekely P, Canet D, Delpuech JJ. Mol Phys 1989;67:81

93. Hosemann R, Bachi SN. Direct Analysis of Diffraction by Matter. New York: Interscience; 1962;

94. Wignall GD, Lin JS, Spooner S. J Appl Cryst 1990;23:241

95. Method of Test for Densities of Plastics by Density Gradient Technique. 1964; D 1505-63T. American Society for Testing of Materials.

96. Gaur U, Wunderlich B. Heat capacity and other thermodynamic properties of linear macromolecules
II. Polyethylene. J Phys Chem Ref Data 1981;10:(1)119-52.

97. Cheban YV, Lau S, Wunderlich B. Analysis of the Contribution of Skeletal Vibrations to the Heat Capacity of Linear Macromolecules. Colloid Polymer Sci 1982;260:(1)9-19.

98. Grebowicz J, Suzuki H, Wunderlich B. Heat Capacities of Polyethylene and Linear, aliphatic Polyoxides. Polymer 1985;26:561-8.

99. Wunderlich B. Heat Capacity Measurements for the Characterization of Two-Phase Polymers. J Thermal Anal 1985;30:1217-21.

100. Bu HS, Cheng SZD, Wunderlich B. Study of the Skeletal Vibrations Used to Compute Heat Capacities of Solid Macromolecules. J Phys Chem 1987;91:4179-88.

101. Pan R, Varma-Nair M, Wunderlich B. A Computation Scheme to Evaluate Debye and Tarasov Equations For Heat Capacity Computation without Numerical Integration. J Thermal Anal 1990;36:145-69.

102. Tucker JE, Reese W. Heat capacity of polyethylene from 2.5 to 30 K. J Chem Phys 1967;46:(4)1388-97.

103. Wunderlich B. Specific Heat of Polyethylene Single Crystals. J Phys Chem 1965;69:2078-81.

104. Opella SJ, Frey MH, J Am Chem Soc, 1979;101:5854

105. Wunderlich B, Sullivan P, Arakawa T, et al. Thermodynamics of crystalline linear high polymers.

III. Thermal breakdown of the crystalline lattice of polyethylene. J Polymer Sci , Part A 1963;1:3581-96.

106. Wunderlich B, Arakawa T. Polyethylene crystallized from the melt under elevated pressure. J Polymer Sci , Part A 1964;2:3697-706.

107. Geil PH, Anderson FR, Wunderlich B, et al. Morphology of Polyethylene Crystallized from the Melt under Pressure. J Polymer Sci , Part A 1964;2:3707

108. Arakawa T, Wunderlich B. Thermodynamics of Crystalline Linear High Polymers.

V. Extended-Chain Copolymers of Polyethylene. J Polymer Sci , Part A-2 1966;4:53-62.

109. Hellmuth E, Wunderlich B. Superheating of Linear High-Polymer Polyethylene Crystals Superheating of Linear High-Polymer Polyethylene Crystals. Journal of Applied Physics 1965;36(10):3039-44.

110. Bassett DC, Turner B. On the phenomenology of chain-extended crystallization in polyethylene. unknown 1974;29:925-55.

111. Yasuniva M, Yamaguchi M, Nakamura A, et al. Melting and crystallization of solution crystallized ultra-high molecular weight polyethylene under high pressure. Polymer Journal 1990;22:(5)411-5.

112. Smith P, Lemstra PJ. Ultra-high strength polyethylene filaments by solution spinning/drawing. Journal of Materials Science 1980;15:505-14.

113. Hsieh Y, Ju J. Melting behavior of ultra-high modulus and molecular weight polyethylene (UHMWPE) fibers. Journal of Applied Polymer Science 1994;53:347-54.

114. Yemni T, McCullough RL. Energetics of phase transformations in polyethylene. Journal of Polymer Science Polymer Physics Edition 1973;11:1358-411.

115. Woo MW, Wong P, Tang Y, et al. Melting behavior and thermal properties of high density polyethylene. Polymer Engineering and Science 1995;35:(2)151-6.

116. Göritz D, Kiss M. Temperature-induced crystallization of oriented polyethylene. Polymer 1986;27:817-20.

117. Economy J, Andreopoulos AG. Morphological modification of UHMPE fibers. Polymers for Advanced Technologies 1994;5:349-57.

118. Clough SB. High temperature x-ray diffraction from drawn and stress-crystallized polyethlyene. Polymer Letters 1970;8:519-23.

119. Ungar G. Effect of radiation on the crystals of polyethylene and paraffins: 2.Phase separation in *'gamma'* irradiated paraffins. Polymer 1980;21:(11)1278-83.

120. Fu Y, Chen W, Pyda M, Londono D, Annis B, Boller A, Habenschuss A, Cheng J, Wunderlich B. Structure-property analysis for gel-spun ultrahigh molecular mass polyethylene fibers. J Macromol Sci -Phys 1996;B35(1):37-87.

121. Hoogsteen W, ten Brinke G, Pennings AJ. DSC experiments on gel-spun polyethylene fibers DSC experiments on gel-spun polyethylene fibers. Colloid & Polymer Science 1988;266:1003-13.

122. Smook J, Pennings AJ. Influence of draw ratio on morphological and structural changes in hot-drawing of UHMW polyethylene fibers as revealed by DSC. Colloid and Polymer Science 1984;262:712-22.

123. Suzuki H, Grebowicz J, Wunderlich B. Heat Capacity of Semicrystalline, Linear Poly(oxymethylene) and Poly(oxyethylene). Makromolekulare Chemie 1985;186:1109-19.

124. Saraf AW, Desai P, Abhiraman AS. Morphology and near T_m behavior of high performance ultrahigh molecular weigth polyethylene fibers. J Appl Sci : Appl Polym Symp 1991;47:67-86.

125. Warren BE. X-ray diffraction. Reading, MA: Addison-Wesley; 1969; 252p.

126. Grubb DT, Prasad K. High-modulus polyethylene fiber structure as shown by x-ray diffraction. Macromolecules 1992;25:4575-82.

127. Hofmann D, Schulz E. Investigations on supermolecular structure of gel-spun / hot-drawn high-modulus polyethylene fibers. Polymer 1989;30:(11)1964-8.

128. Azriel AY, Vasil'ev VA, Kazaryan LG. X-ray meridional scattering in drawn polyethylene.
Account of matching orientation of crystallites along fibril. Polymer Science USSR 1989;31:(11)2646-52.

129. Adams WW, Kumar S, Martin DC, et al. Lattice imaging of poly(*p*-phenylene benzobisoxazole) fiber. Polymer Communications 1989;30:(9)285-7.

130. Zubov YA, Chvalun SN, Selikhova VI, et al. The structure of highly oriented high modulus polyethylene. Polymer Engineering and Science 1992;32:(17)1316-24.

131. van Aerle NAJM, Braam AWM. A structural study on solid state drawing of solution-crystallized ultra-high molecular weight polyethylene. Journal of Materials Science 1988;23:4429-36.

132. Chvalun SN, Sinevich YA, Konstantinopolskaya MB, et al. A comparative study of structural processes in the deformation of single-crystal mats and bulk specimens of polyethylene. Polymer Science USSR 1988;30:(9)2091-100.

133. van Hutten PF, Koning CE, Pennings AJ. The plastic deformation of ultra-high molecular weight polyethylene. Journal of Materials Science 1985;20:1556-70.

134. Clements J, Ward IM. Superheating effects on the melting of ultra-high modulus linear polyethylene. Polymer 1982;23:(6)935-6.

135. Moonen JAHM. Investigations on supermolecular structure of gel-spun/hot-drawn high-modulus polyethylene fibers. Polymer 1991;32:(17)3262-3.

136. Kavesh, S.Fu, Y. 1994; Dr. S. Kavesh, Central Research, Allied-Signal Inc., personal communication, February 1994.

137. Martinez-Salazar J, Barham PJ, Keller A. Studies on polyethylene crystallized at unusually high supercooling: Fold length, habit, growth rate, epitaxy. J Polym Sci , B, Polym Phys 1984;22:1085-96.

138. VanderHart DL, Khoury F. Polymer 1984;25:1589

139. VanderHart DL. J Magn Reson 1981;44:117

140. Kaji A, Ohta Y, Yasuda H, et al. Polymer 1990;22:455

141. Kaji A, Ohta Y, Yasuda H, et al. Polymer 1990;22:893

142. Adams WW, Briber RM, Sherman ES, et al. Microstructure of high modulus solid state extruded polyethylene: 2. X-ray scattering studies of 12, 24 and 36 extrusion draw ratio. Polymer 1985;26:17-26

143. Takahashi Y, Ishida T, Furusaka M. J Polymer Sci , Polymer Phys Ed 1988;26:2267

144. Tamni T, McCullough RL. J Polymer Sci , Polymer Phys Ed 1976;17:131

145. Miyaji H, Asahi T, Miyamoto Y, et al. J Polymer Sci , Polymer Phys Ed 1987;25:159

146. Kiho H, Peterlin A, Geil PH. Polymer deformation: IV. Twinning and phase transformation of polyethylene single crystals as a function of stretching direction. Journal of Applied Physics 1964;35:(5)1599-605.

147. Bevis M, Crellin EB. The geometry of twinning and phase transformations in crystalline polyethylene. Polymer 1971;12:666-84.

148. Matyi RJ, Crist B, Jr. J Polymer Sci , Polymer Phys Ed 1978;16:1329

149. Prevorsek DC, Chin HB, Kwon YD, et al. J Appl Sci : Appl Polym Symp 1991;47:45

Appendices

Appendix A:

Figures

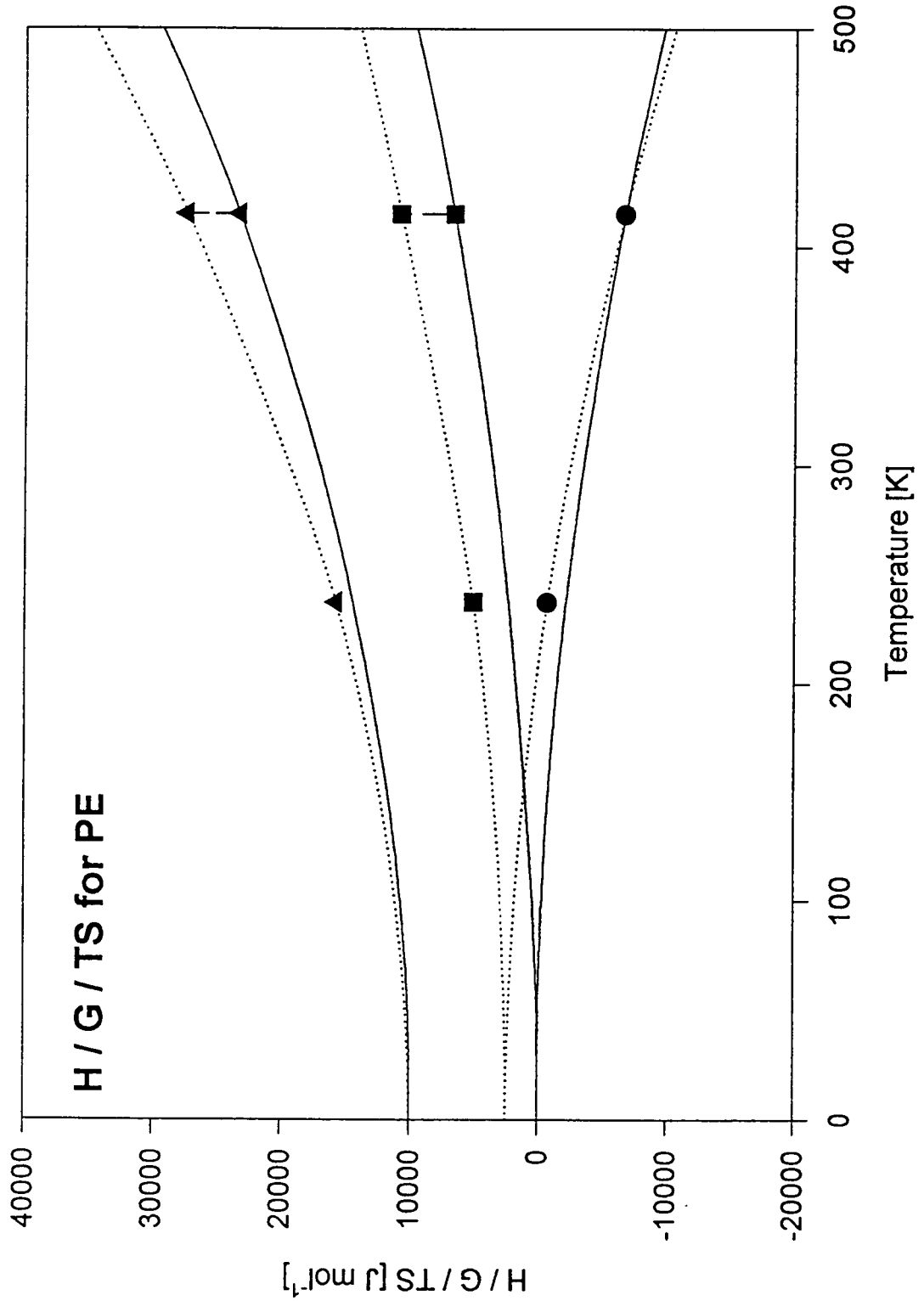

Fig. 3.1-1 Thermodynamic functions of amorphous and crystalline PE (dashed line amorphous, solid line crystalline).

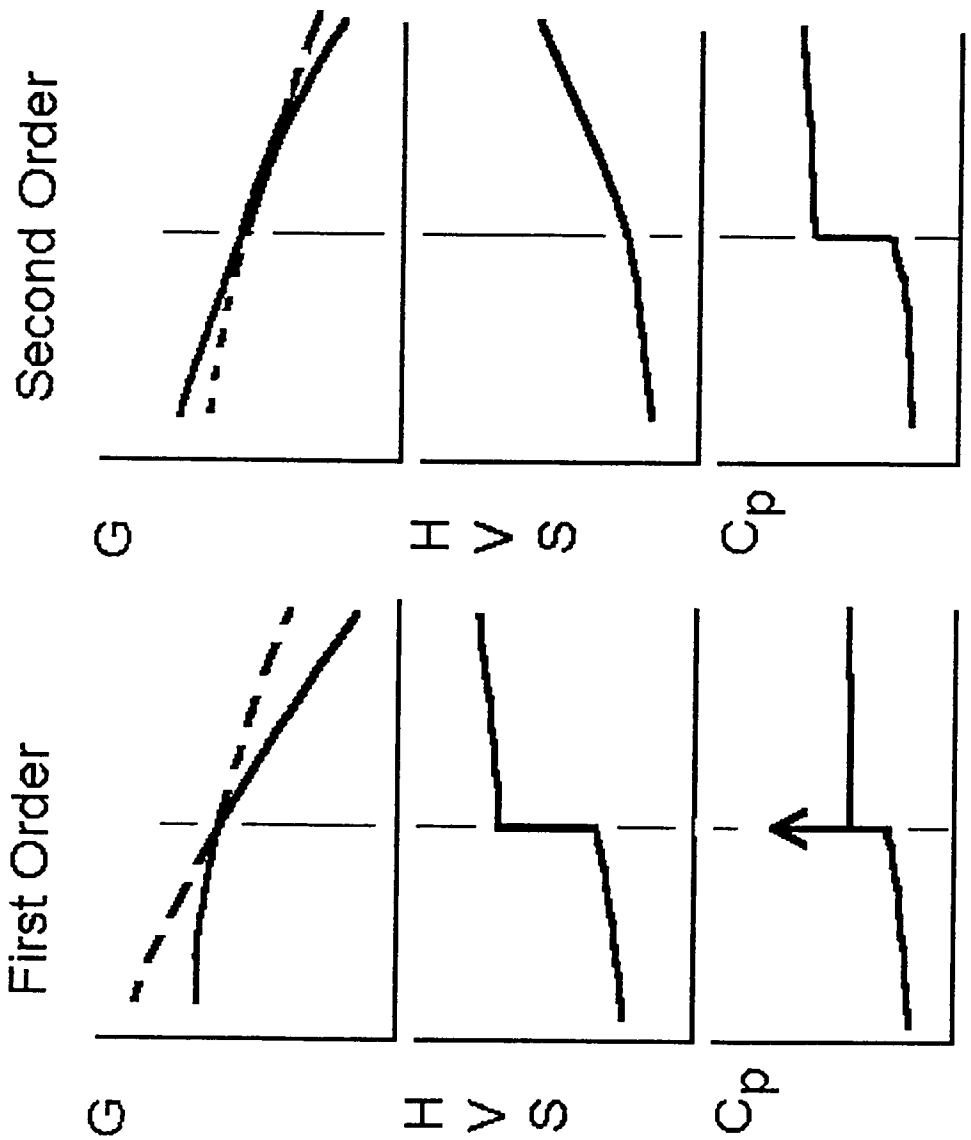

Fig. 3.1-2 Schematic drawing of the changes in G,S, and Cp during phase transition according to [57]. Left: First-order transition. Right: Second-order transition.

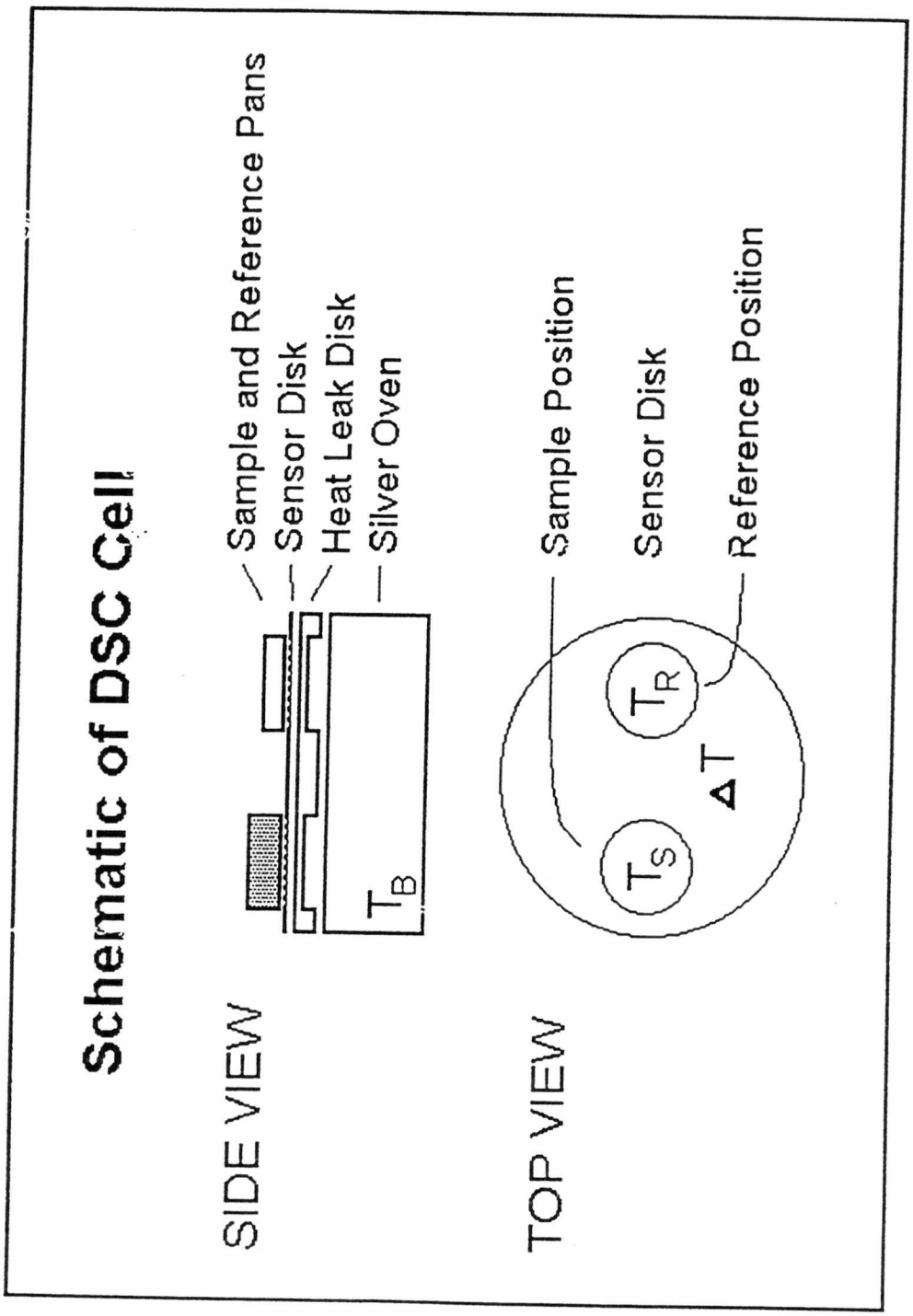

Fig. 3.2-1 DSC cell schematic (side and top view).

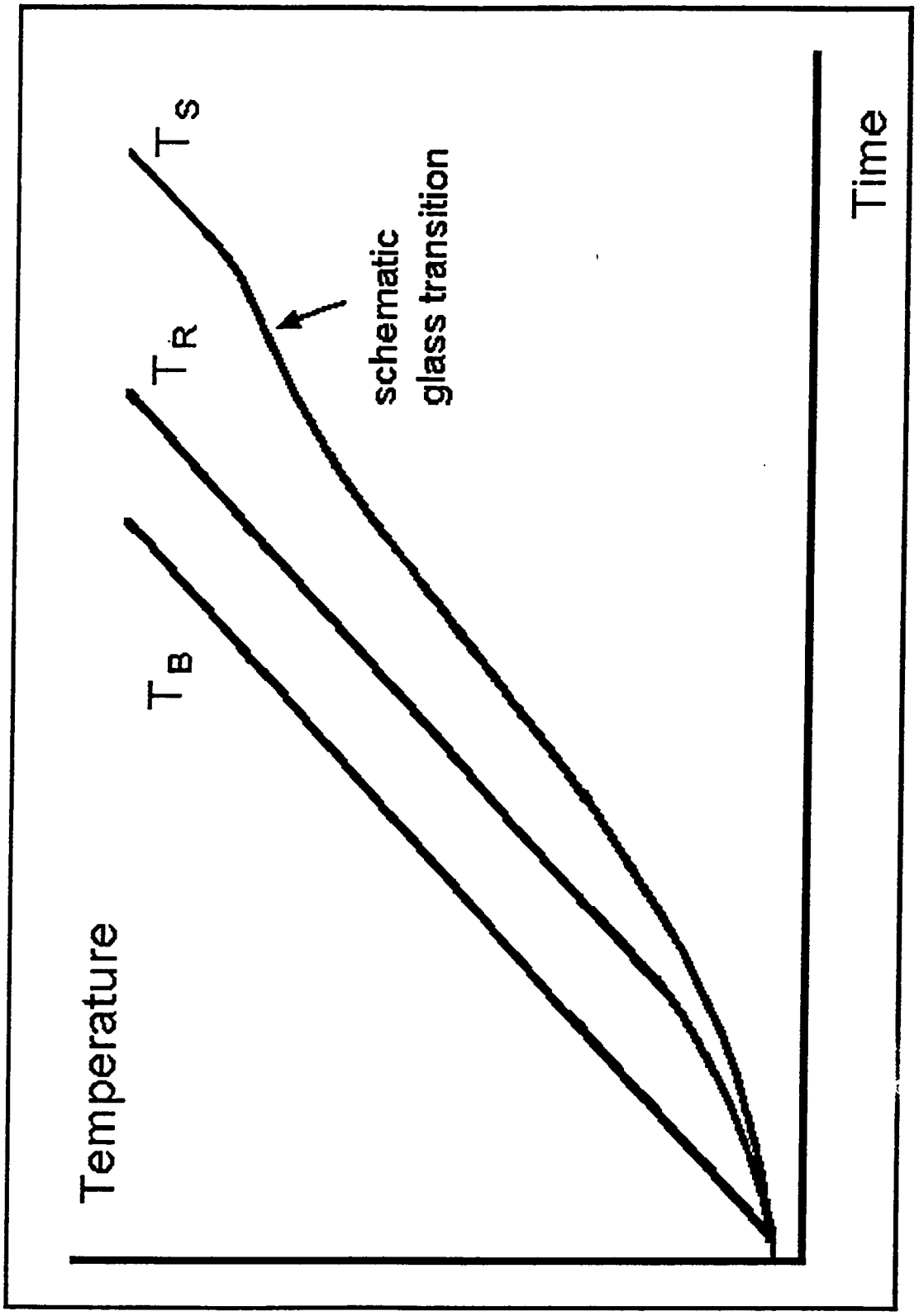

Fig. 3.2-2 Temperature profiles for block, sample and reference temperature.

Principle of DSC

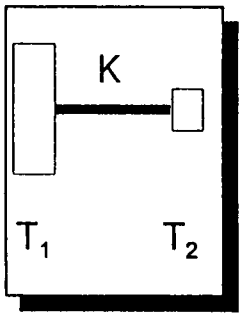

$$\frac{dQ}{dt} = K[T_1(t) - T_2(t)]$$

$$\frac{dQ}{dt} = \frac{dQ}{dT}\frac{dT}{dt} = C_p \times q$$

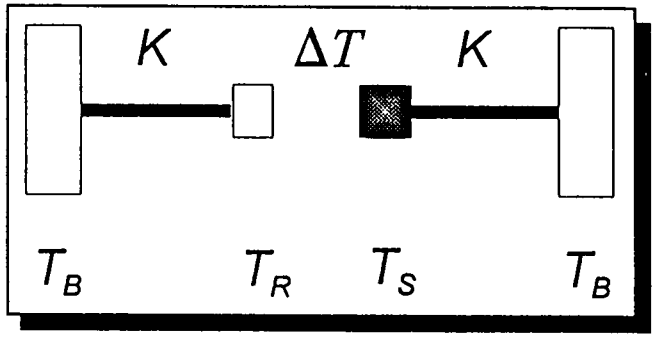

$$\Delta T = \frac{q\,\Delta C_p}{K_T}$$

$$\frac{dQ}{dt} = HF = \frac{q\,\Delta C_p}{K_{HF}}$$

$$\frac{dQ_R}{dt} = K[T_B(t) - T_R(t)] \qquad \frac{dQ_S}{dt} = K[T_B(t) - T_S(t)]$$

Fig. 3.2-3 Basic Calculations for the calculation of heat capacity.

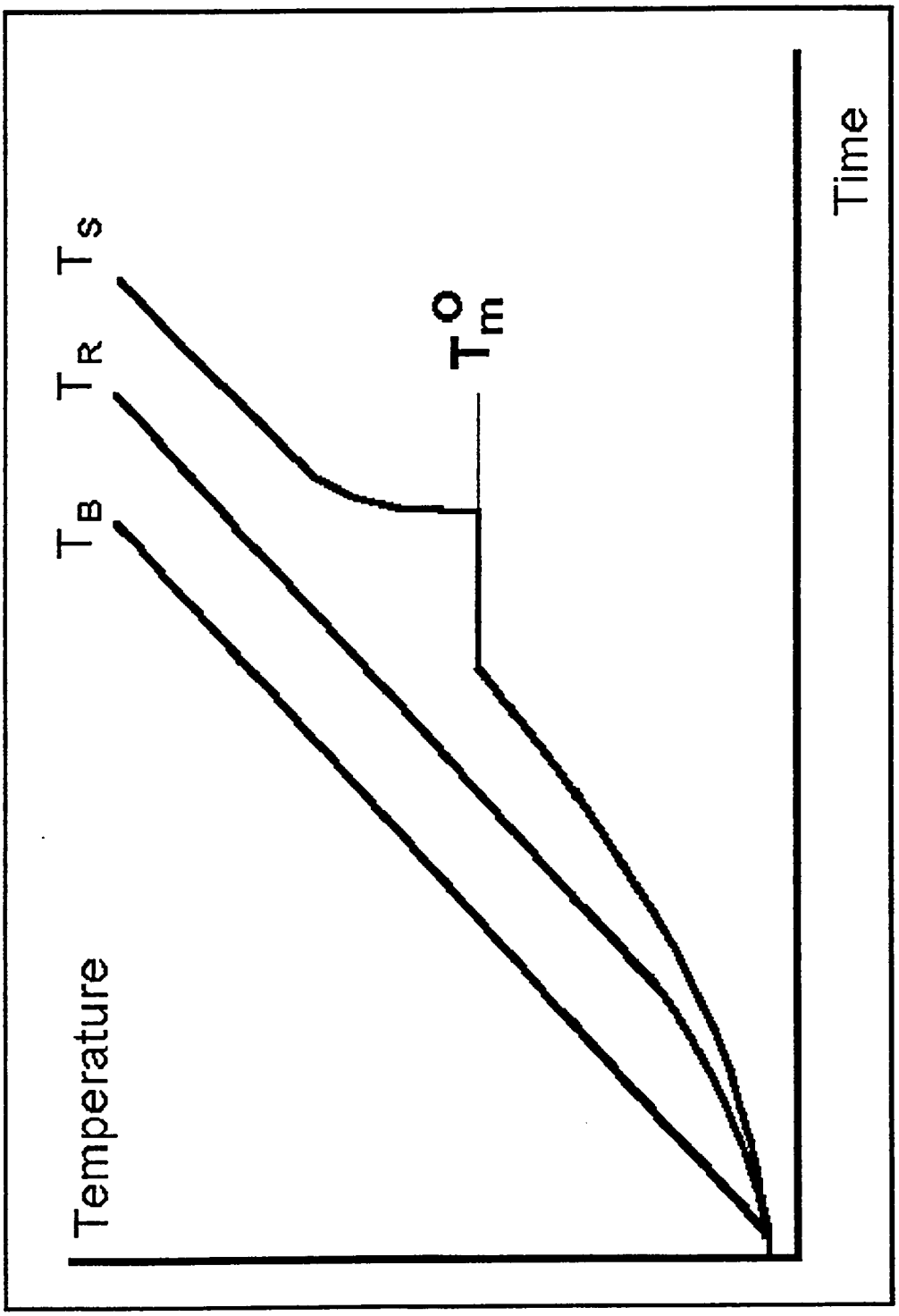

Fig. 3.2-4 Temperature profiles on heating with a melting transition.

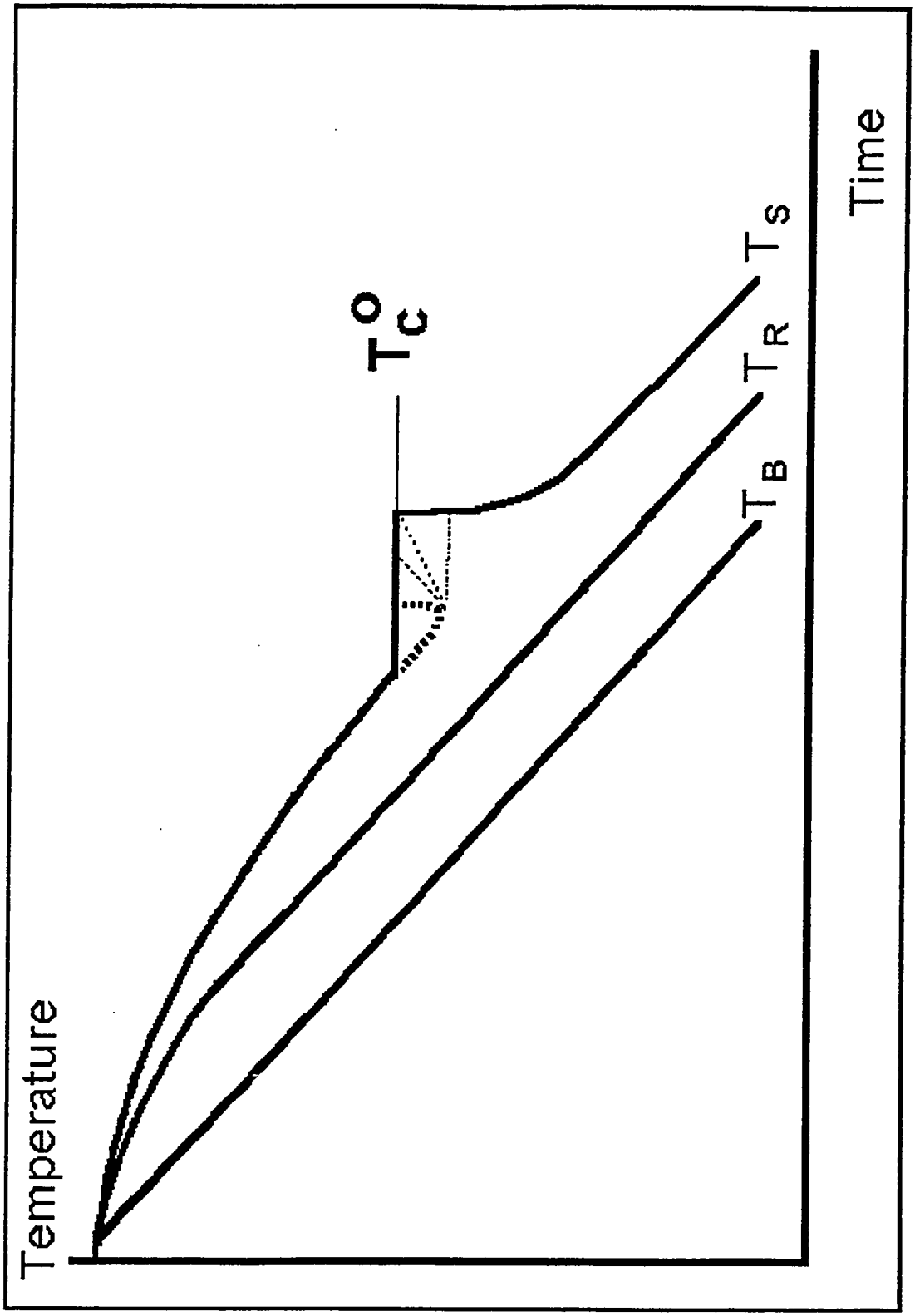

Fig. 3.2-5 Temperature profiles on cooling with crystallization.

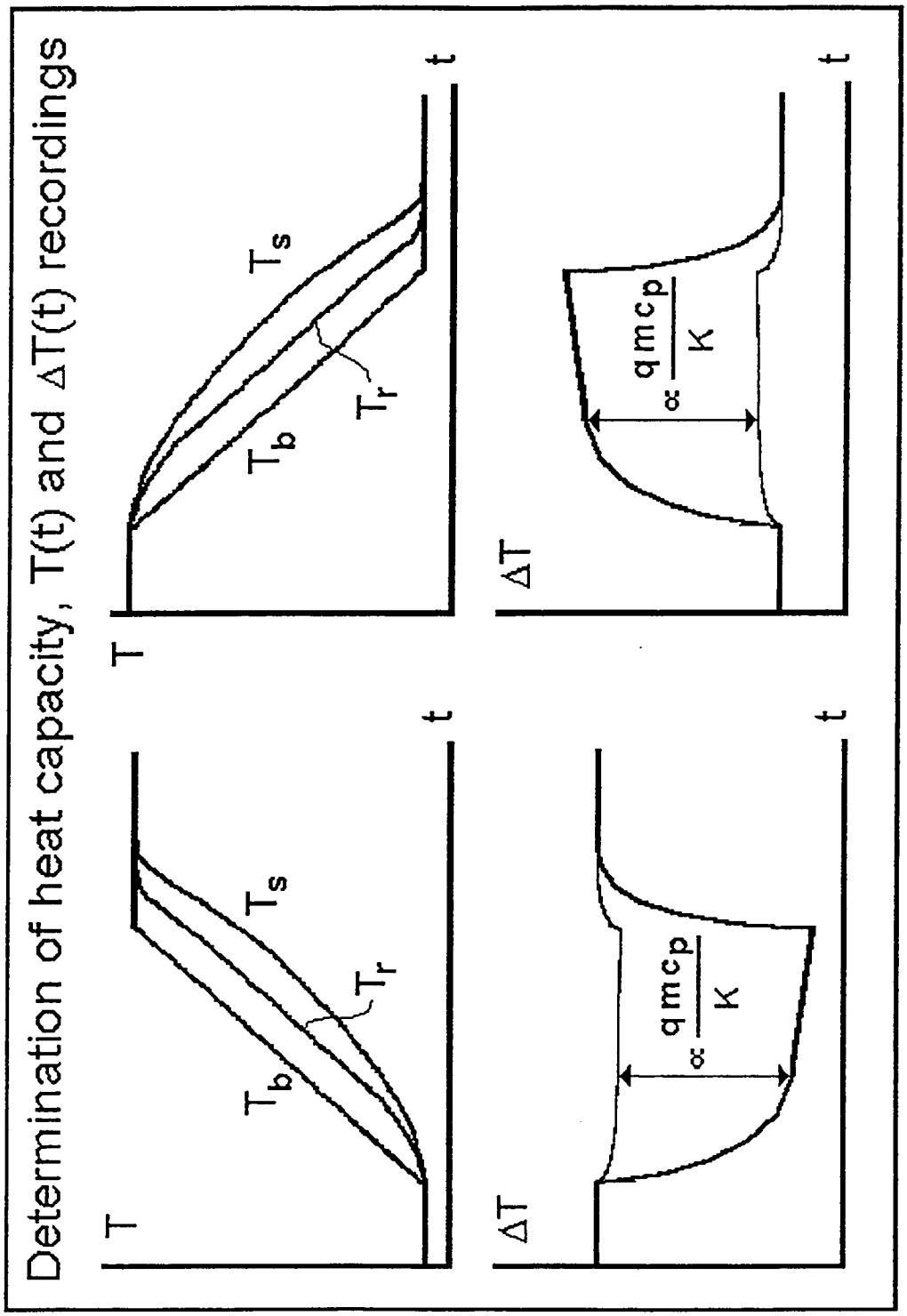

Fig. 3.2-6 Temperature profiles with the corresponding ΔT signals, used for the heat capacity determination. The thin line in the bottom graphs correspond to the measurement of the empty pan on the sample side.

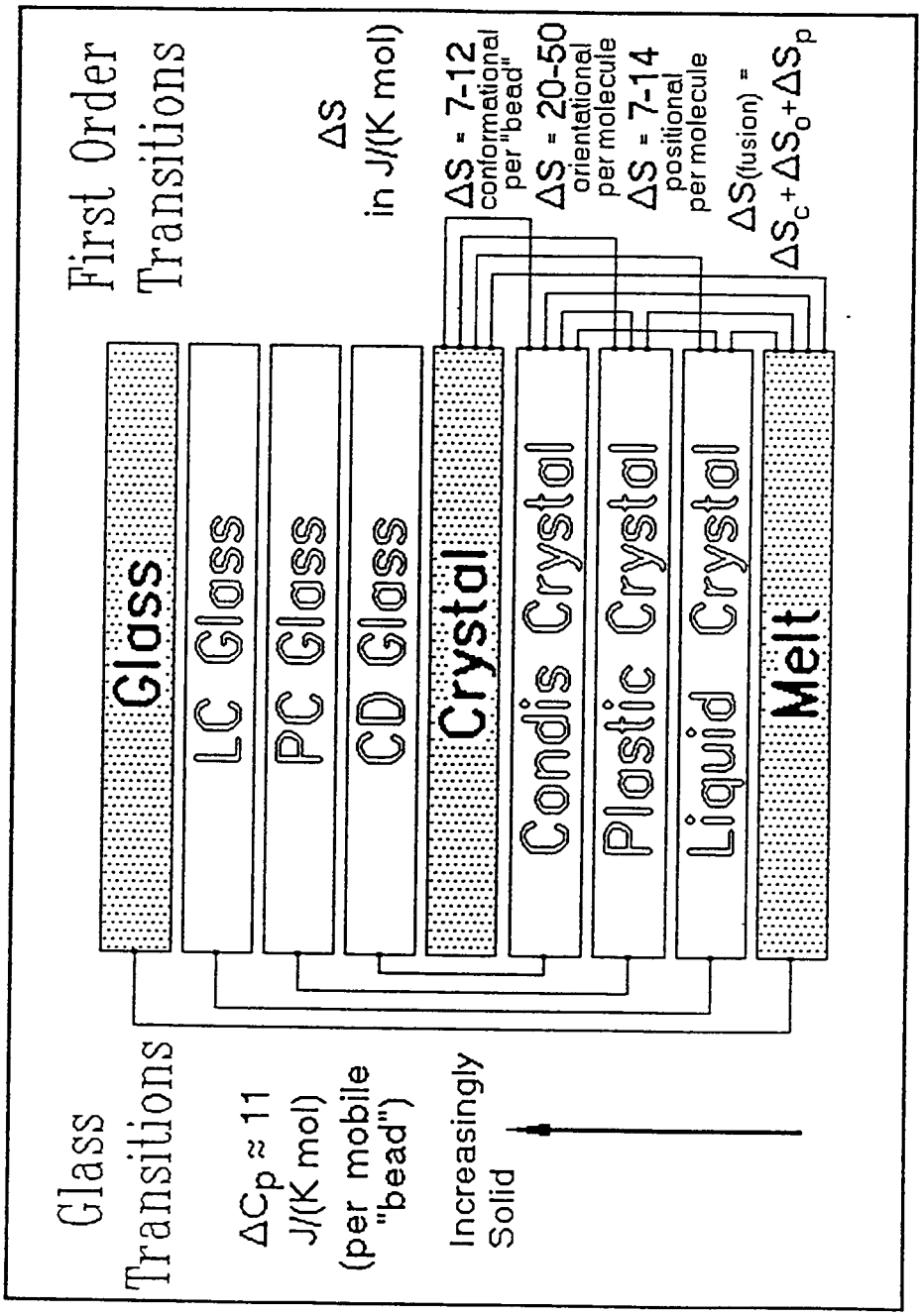

Fig. 3.3-1 Schematic of the transition regions for the classical condensed phases (dotted areas and full lettering) and the mesophases. Glass transitions and observed first-order transitions are indicated by the connecting lines. The empirically observed approximate entropies and heat capacities are listed. Drawn after [56].

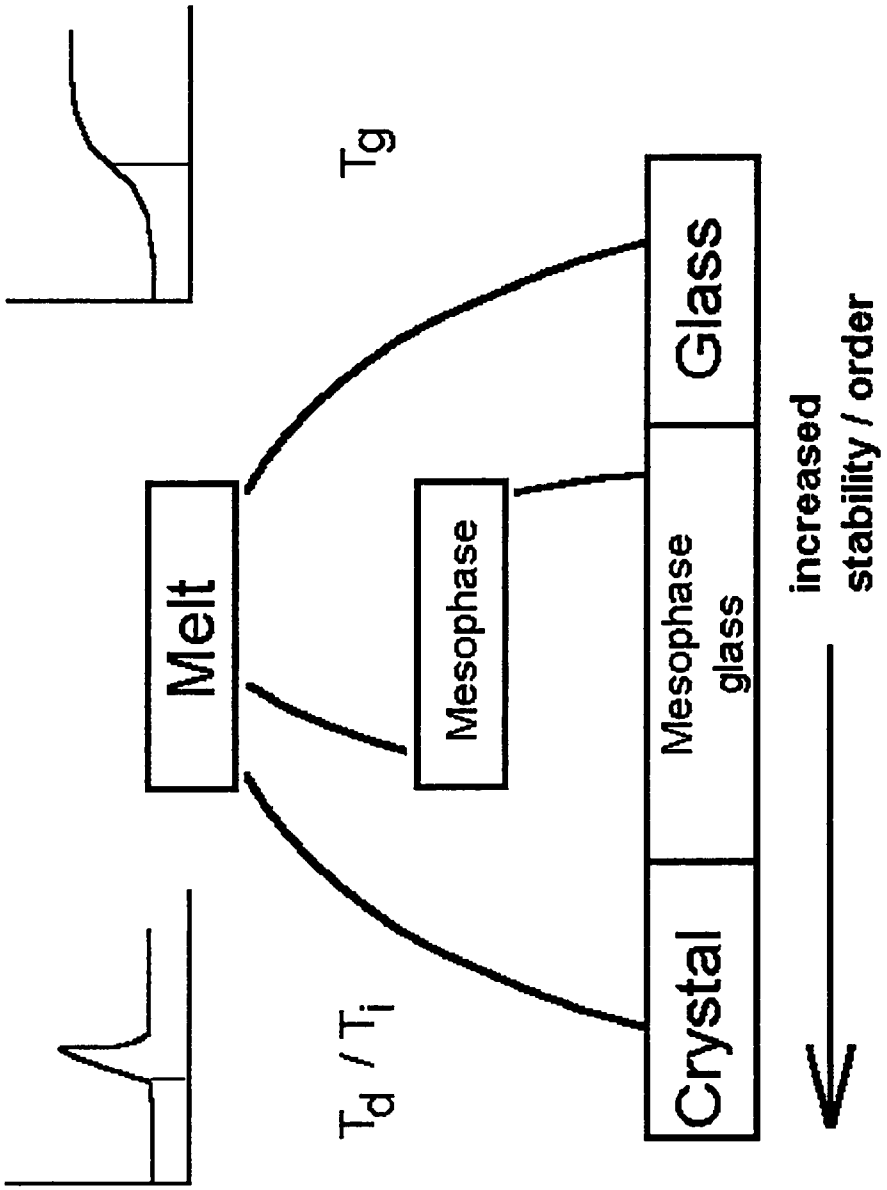

Fig. 3.3-2 Simplified schematic of the transition regions for the classical condensed phases and only one mesophase.

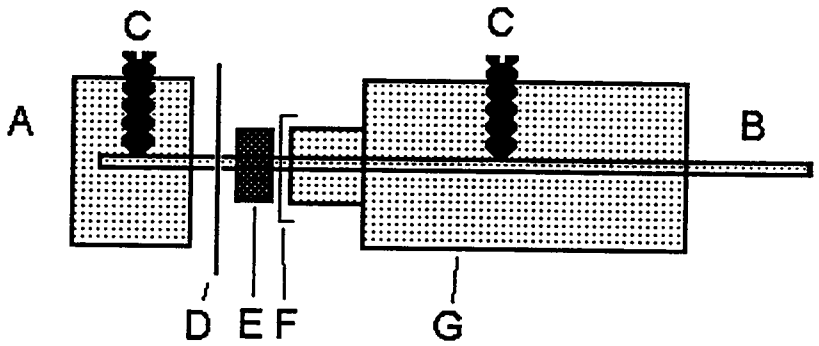

Fig. 4.1-1 Schematic of the fiber winding tool.

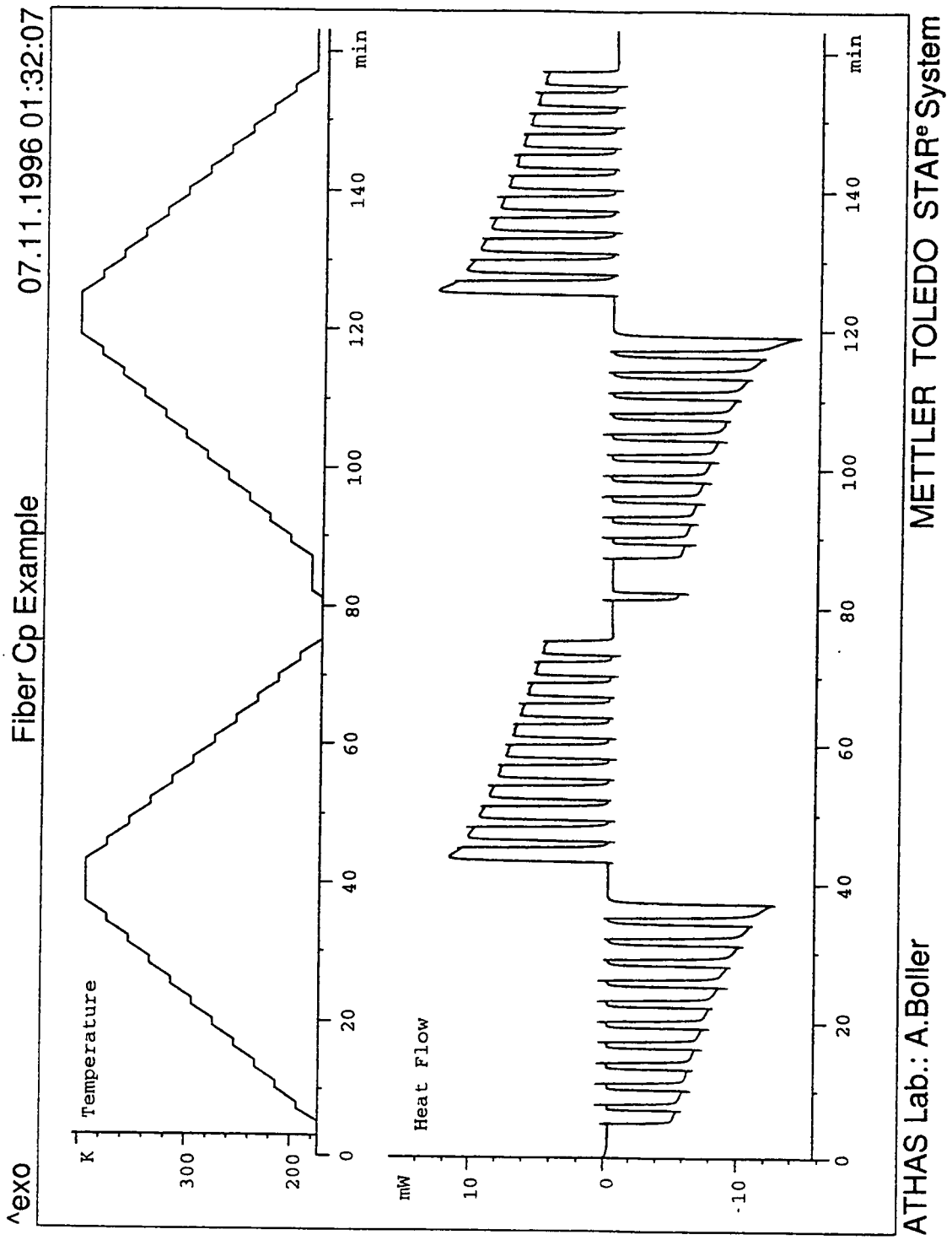

Fig. 4.2-1 Temperature profile and the resulting heat flow for one of the fiber spool samples.

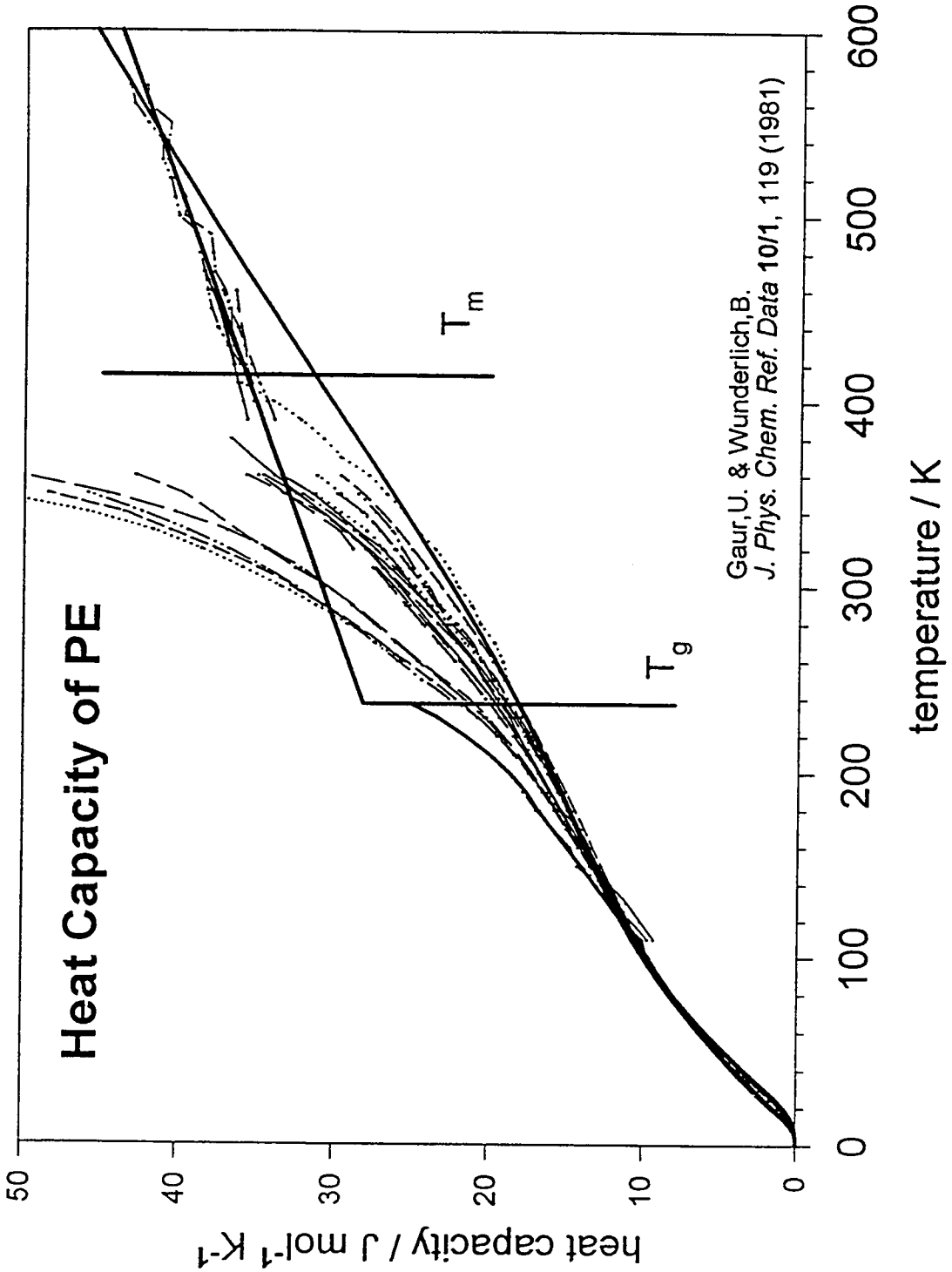

Fig. 5.1-1 Collection of all the reanalyzed heat capacity data [96] with the ATHAS databank values (heavy lines) and the transition temperatures (vertical lines)

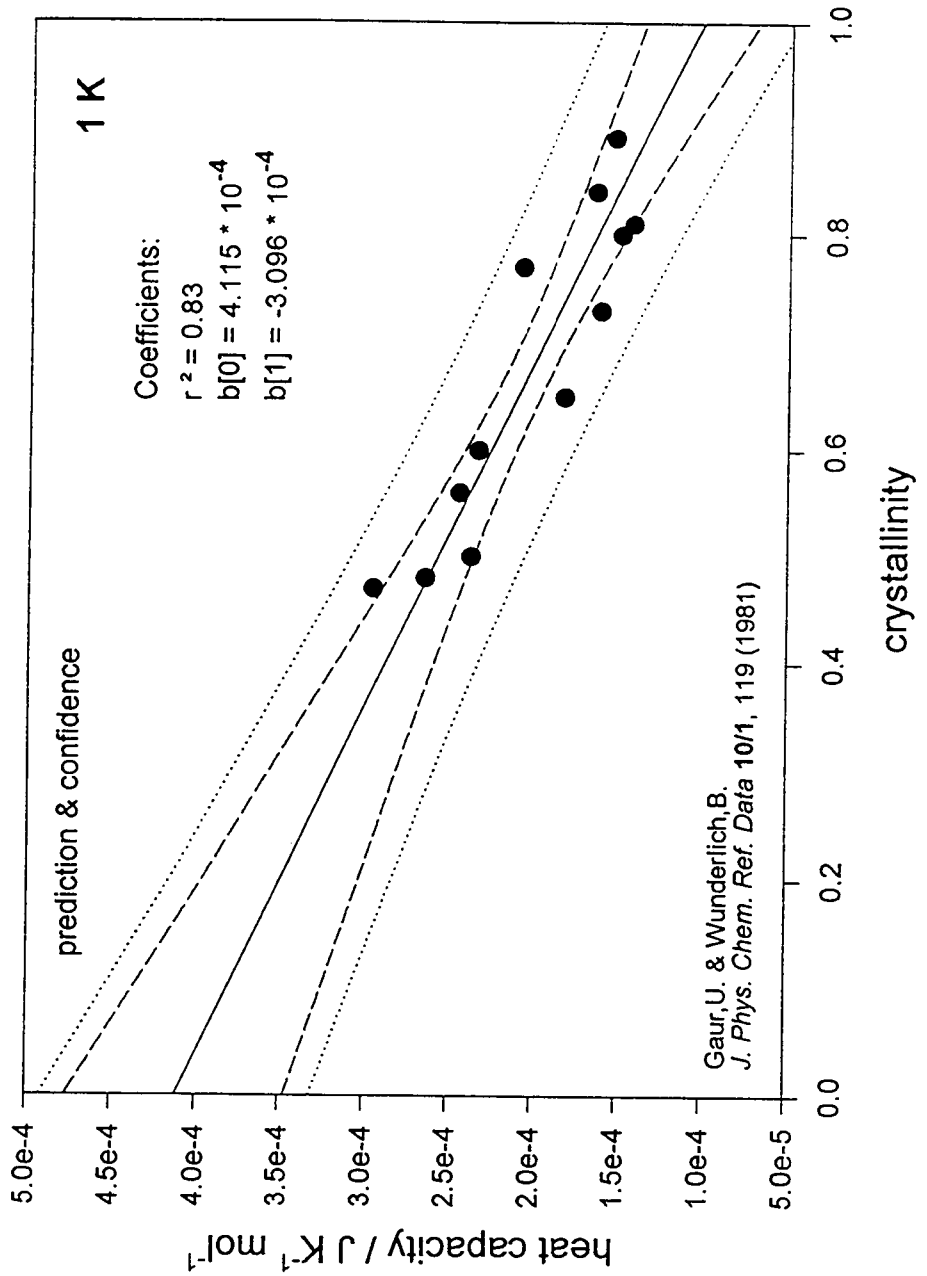

Fig. 5.1-2A Heat capacity vs crystallinity data at 1 K.

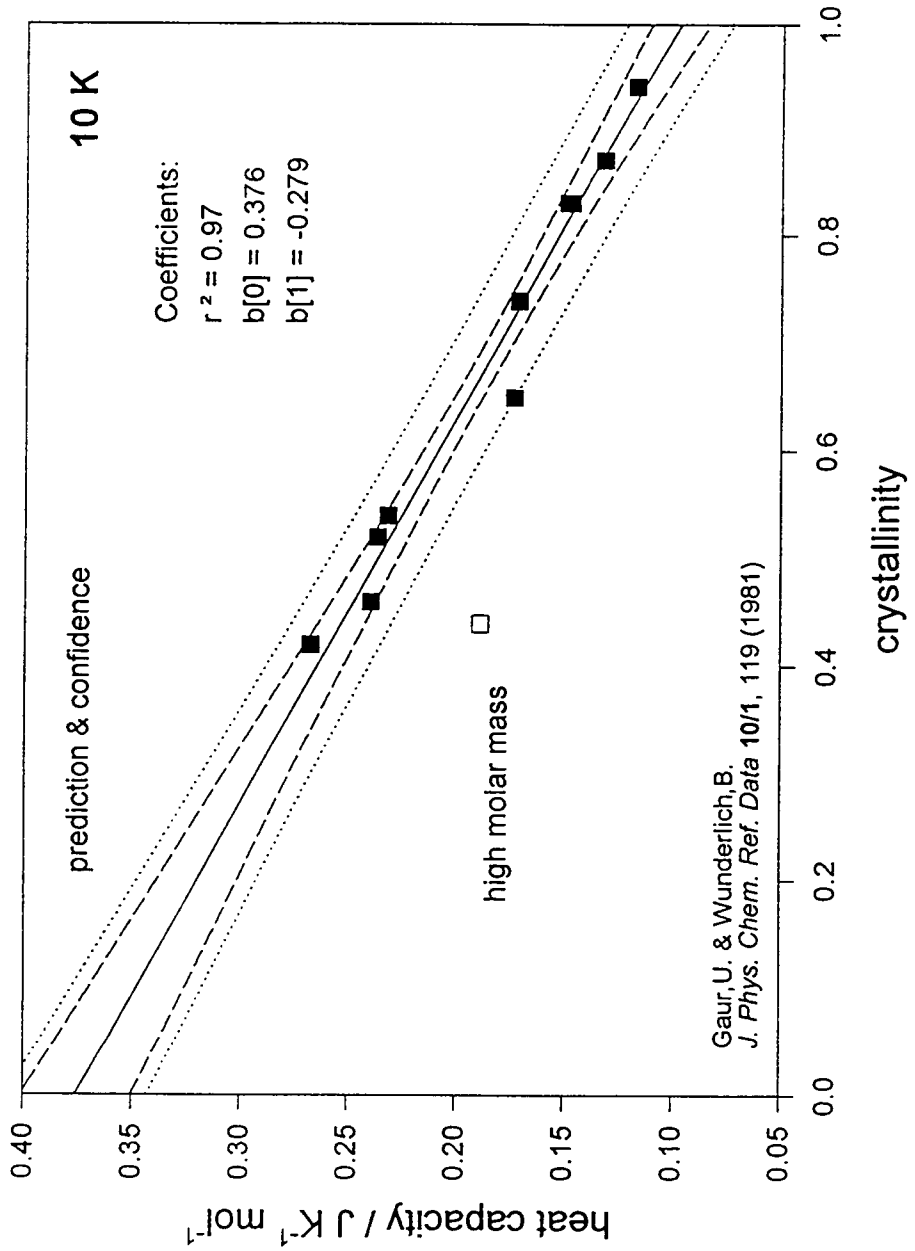

Fig. 5.1-2B Heat capacity vs crystallinity data at 10 K.

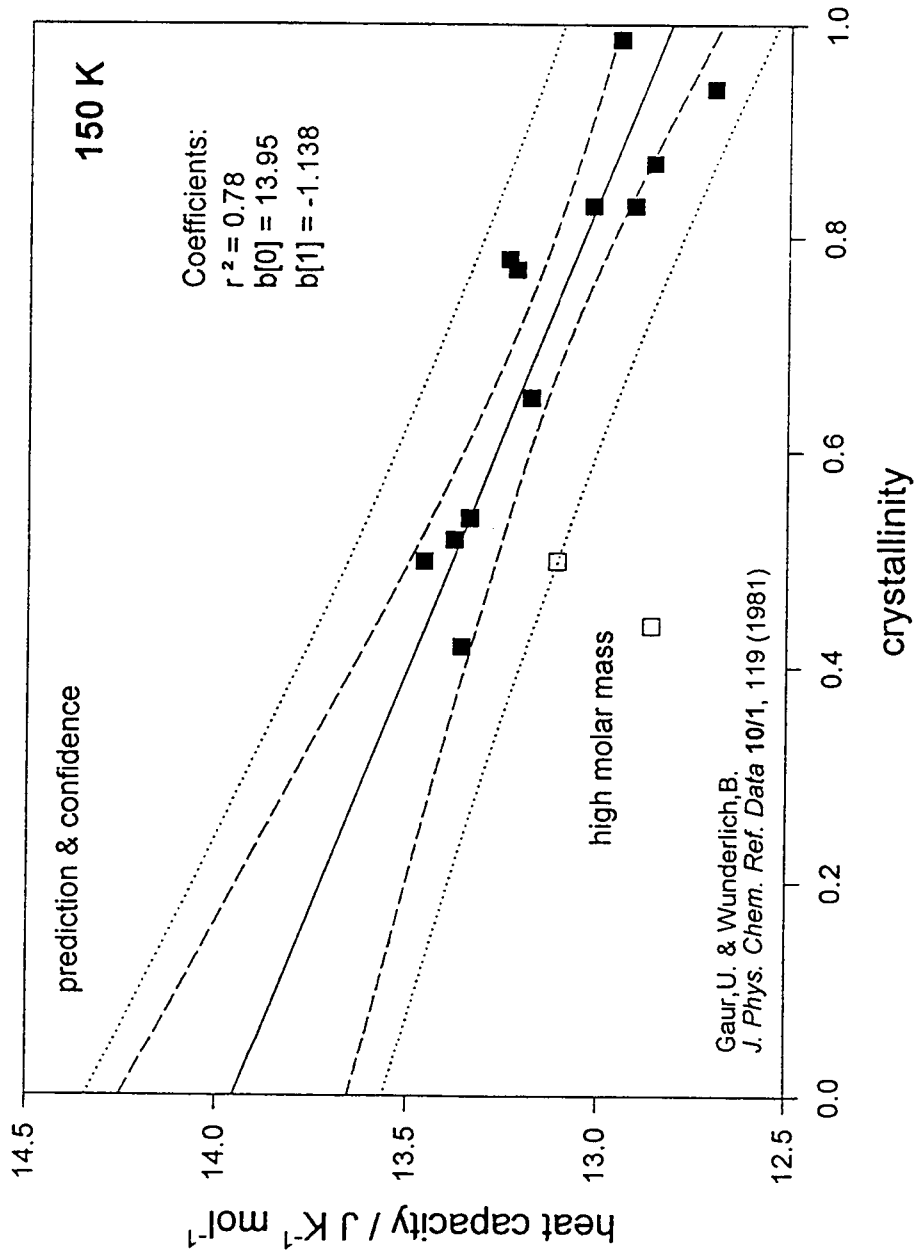

Fig. 5.1-2C Heat capacity vs crystallinity data at 150 K.

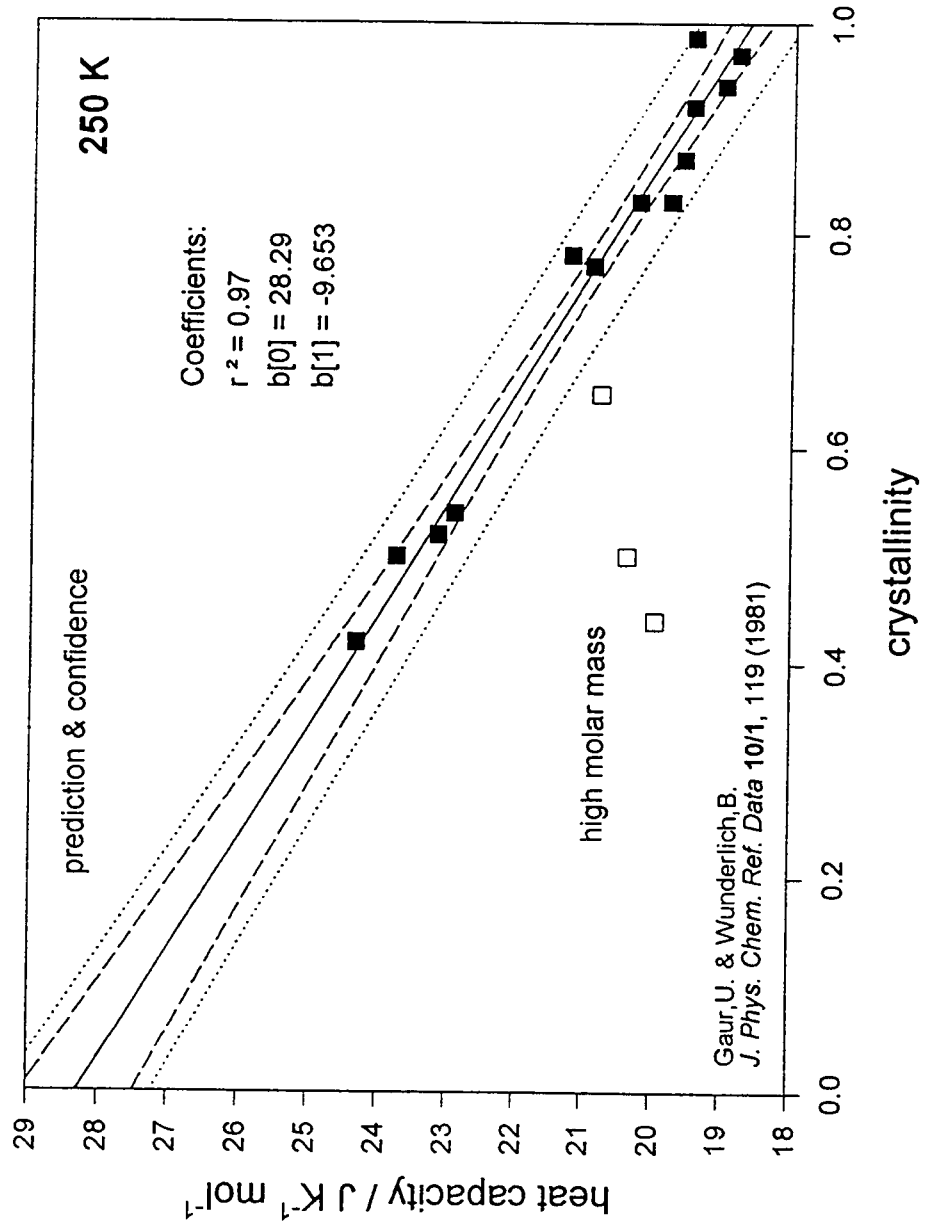

Fig. 5.1-2D Heat capacity vs crystallinity data at 250 K.

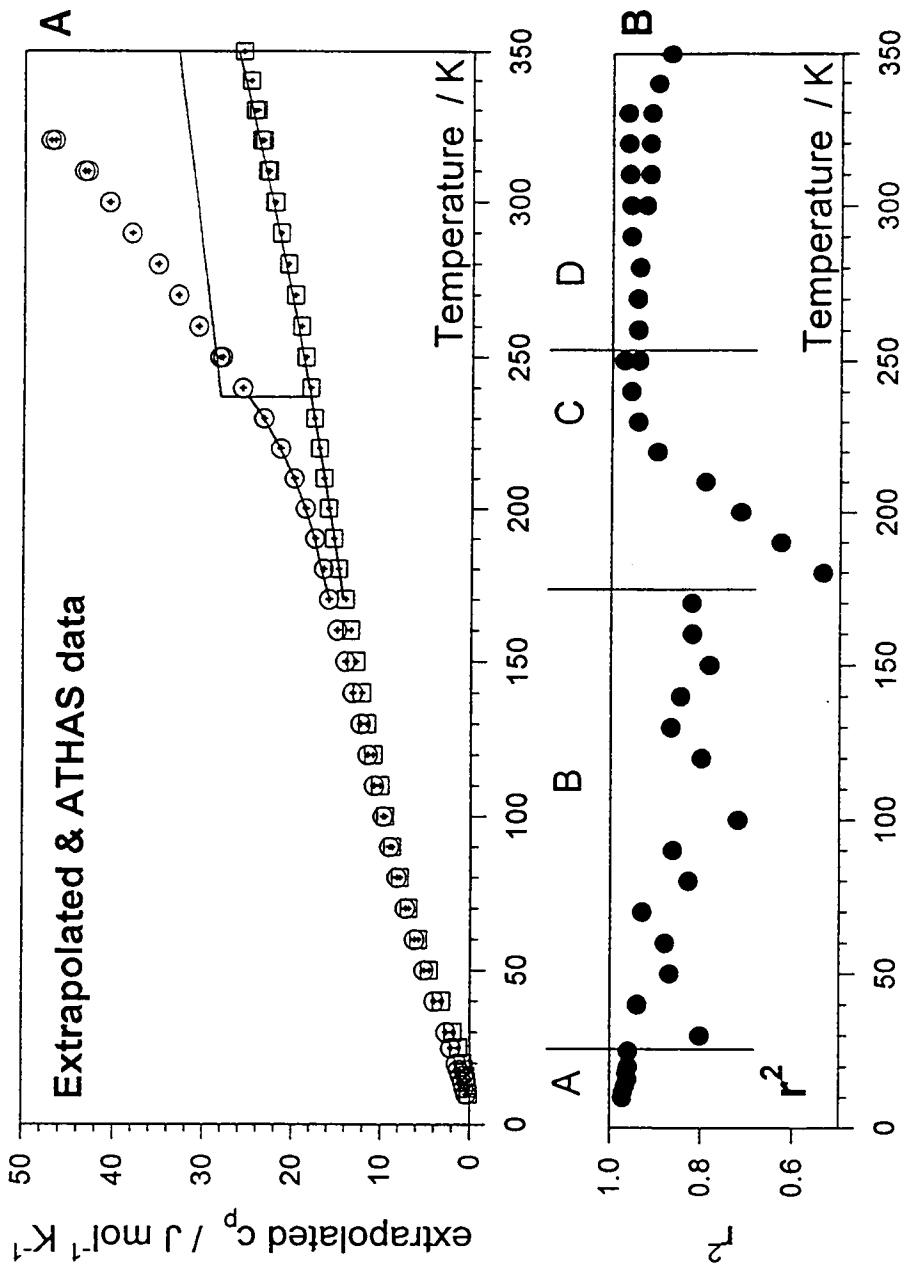

Fig. 5.1-3 A) Extrapolated crystalline and amorphous heat capacities, B) r^2 values of the linear fit with distinct features in the glass transition range.

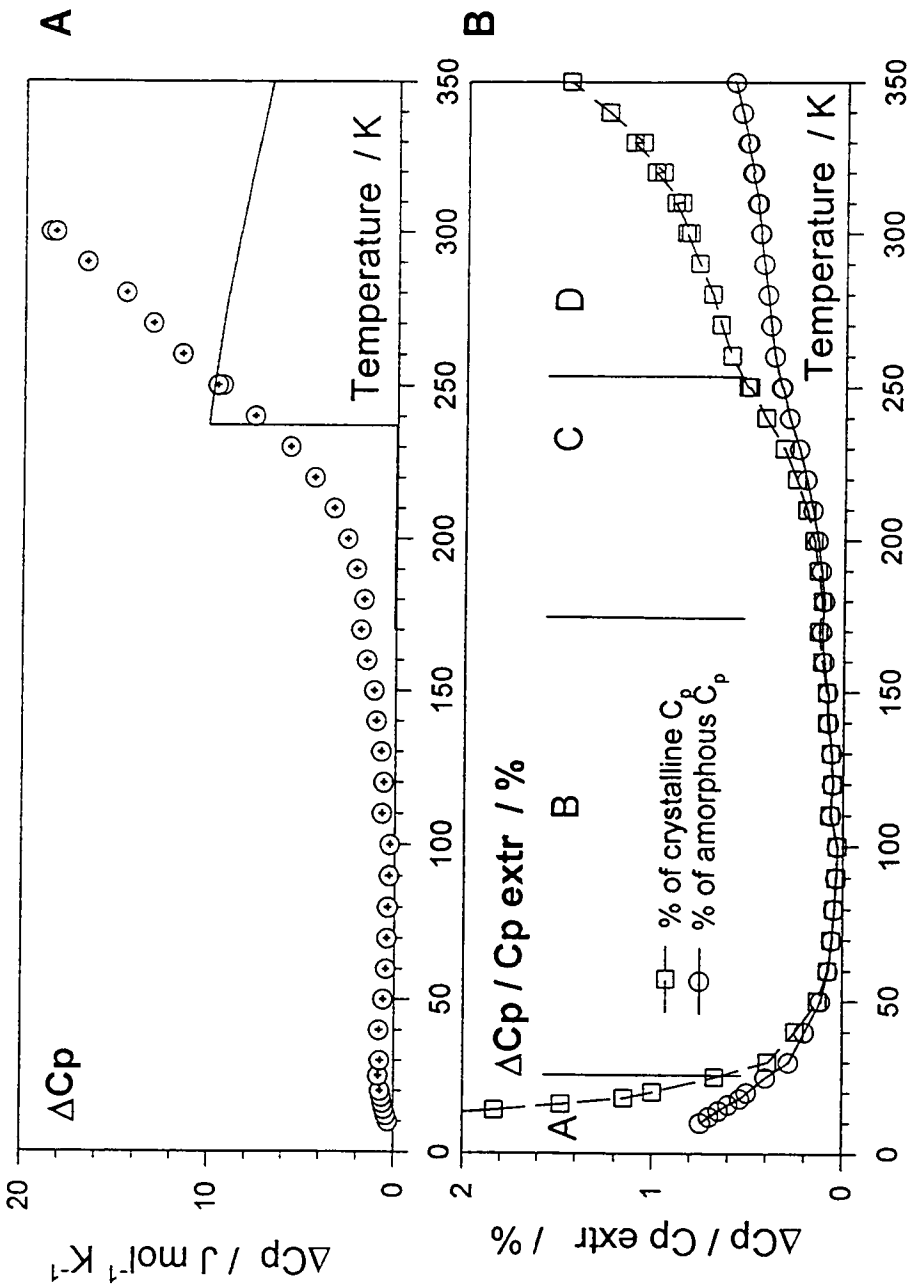

Fig. 5.1-4 A) Differences between the extrapolated heat capacity values. B) same differences as in A as percentage of the extrapolated crystalline and amorphous heat capacities.

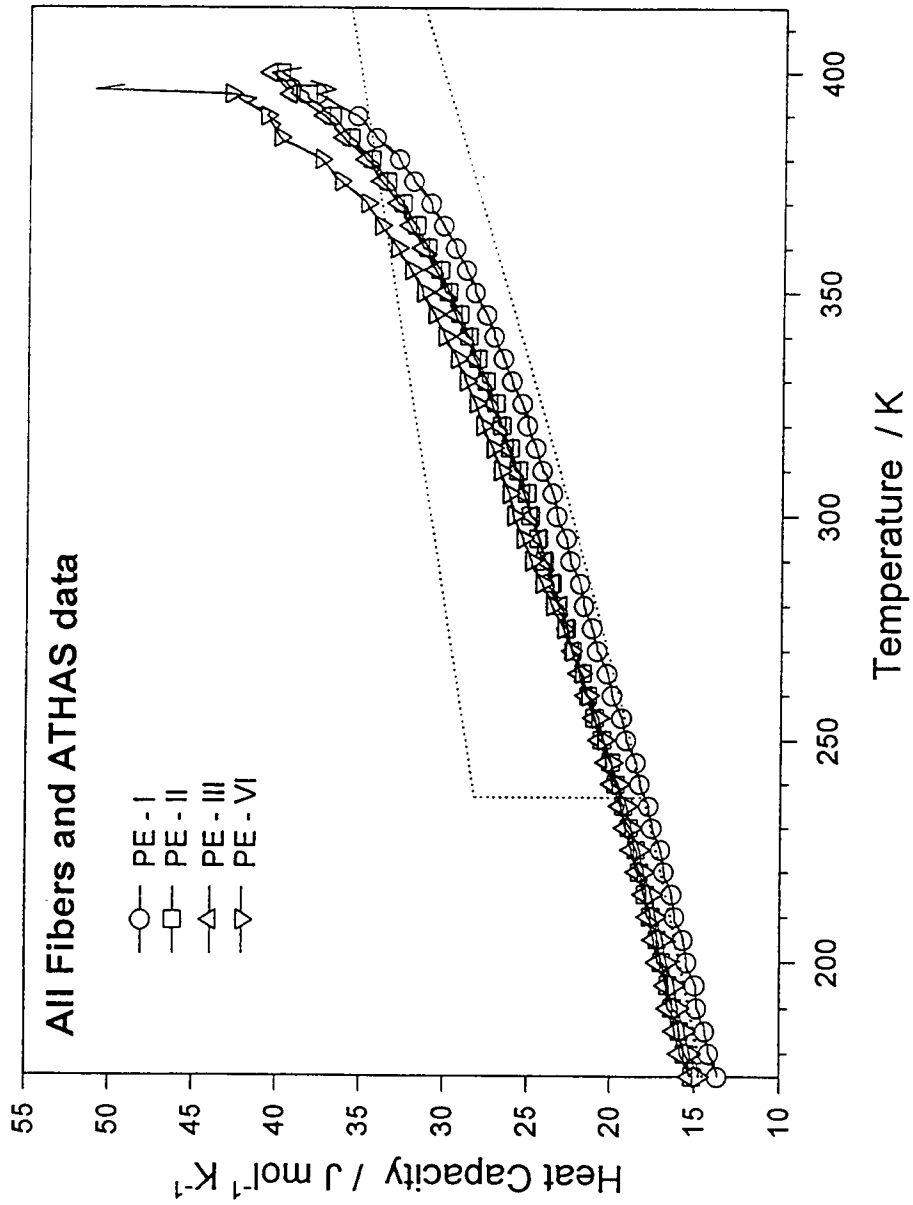

Fig. 5.1-5 Fiber heat capacities, averaged over 15-20 experiments.

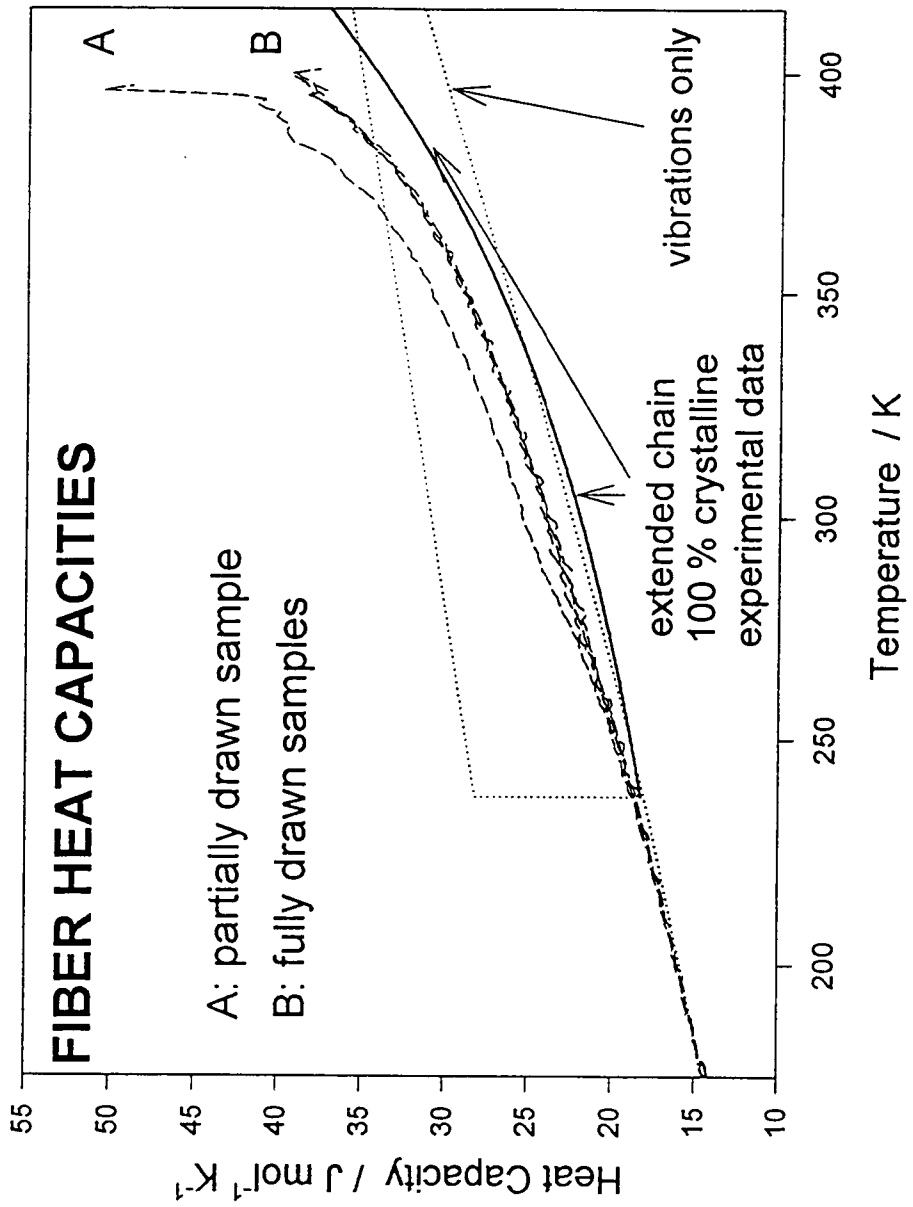

Fig. 5.1-6 Fiber heat capacities adjusted to the vibration-only heat capacity at 180 K together with the experimental 100% crystalline extended chain PE [33]. Amorphous (dashed line) and the vibrations only heat capacity (solid line) are included for comparison.

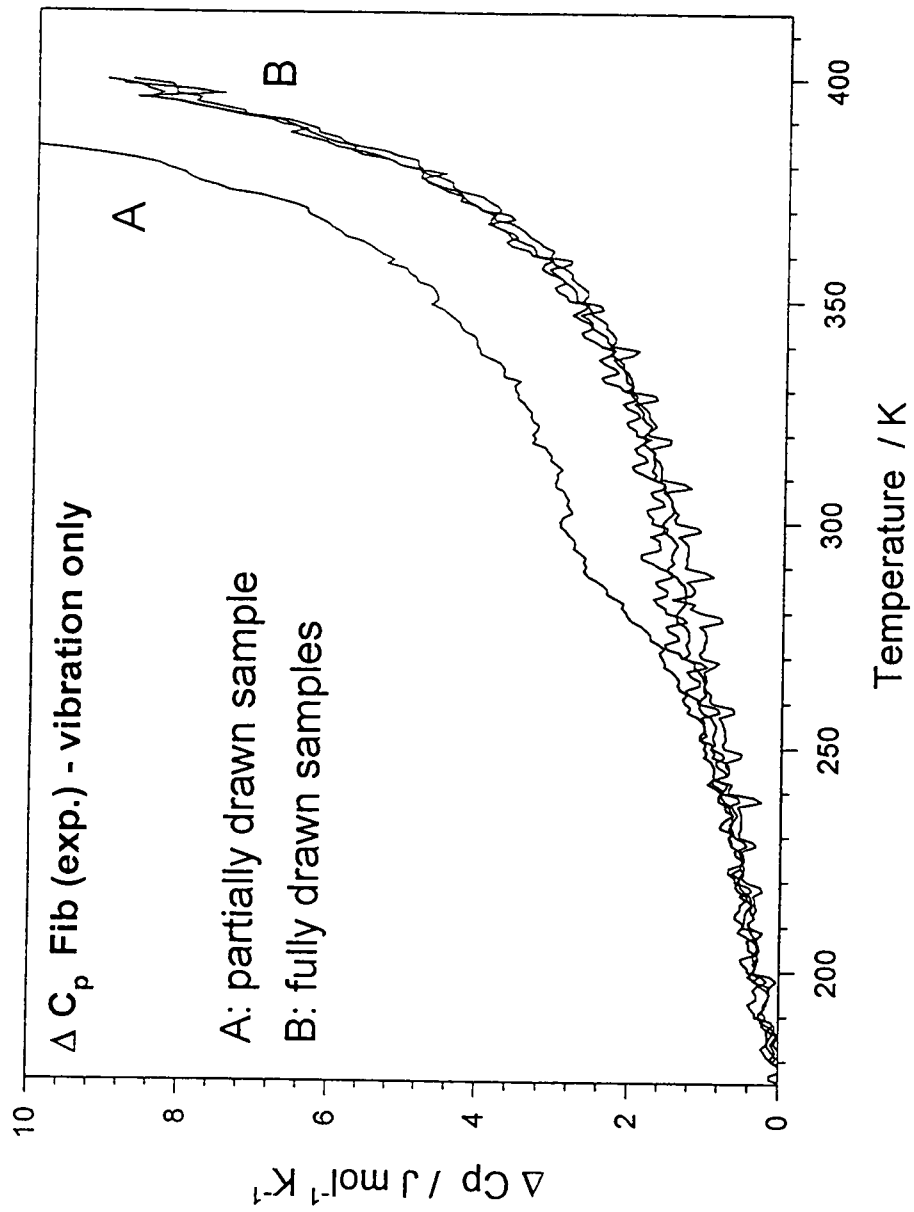

Fig. 5.1-7 Heat capacity differences with the vibrations only heat capacity as reference state.

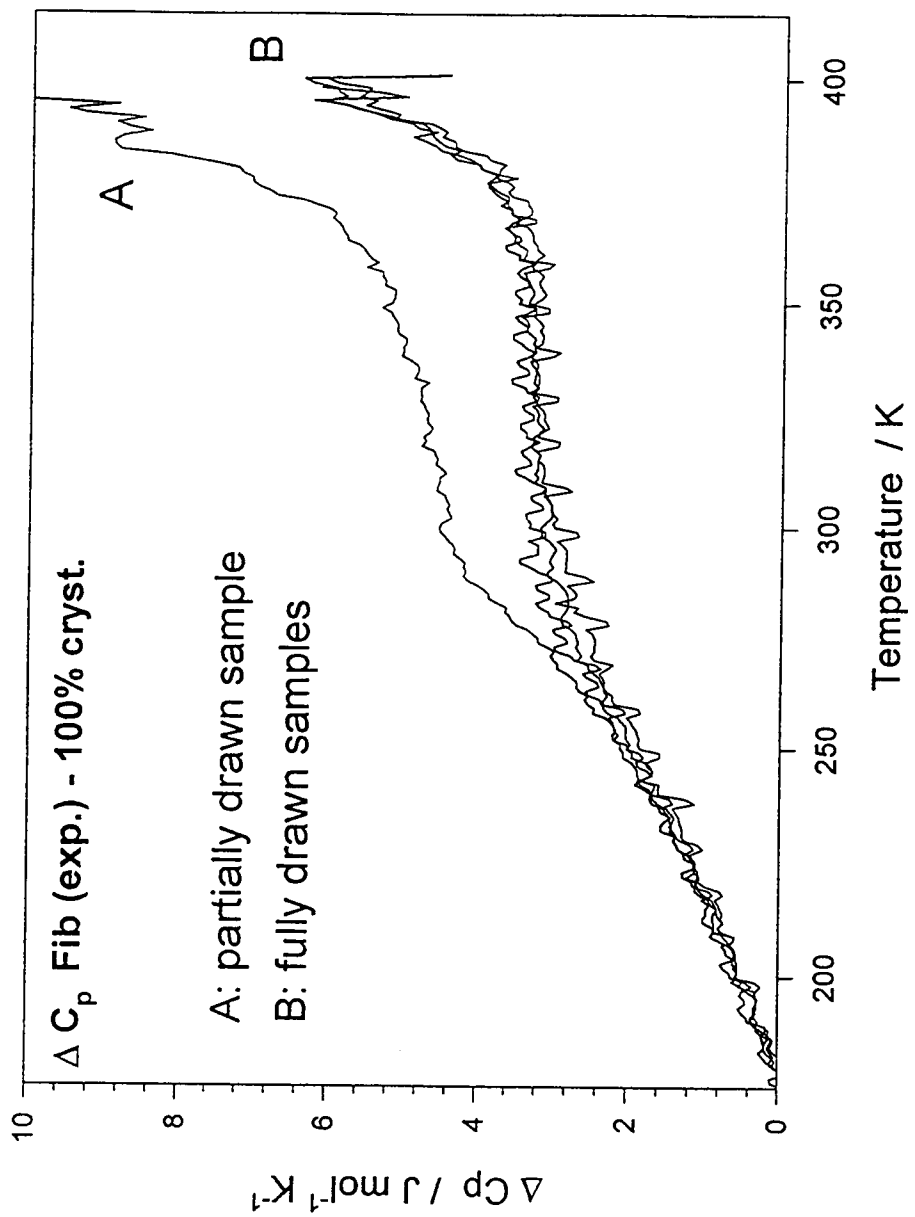

Fig. 5.1-8 Heat capacity differences with the experimental 100% crystalline extended chain PE [33] as reference state.

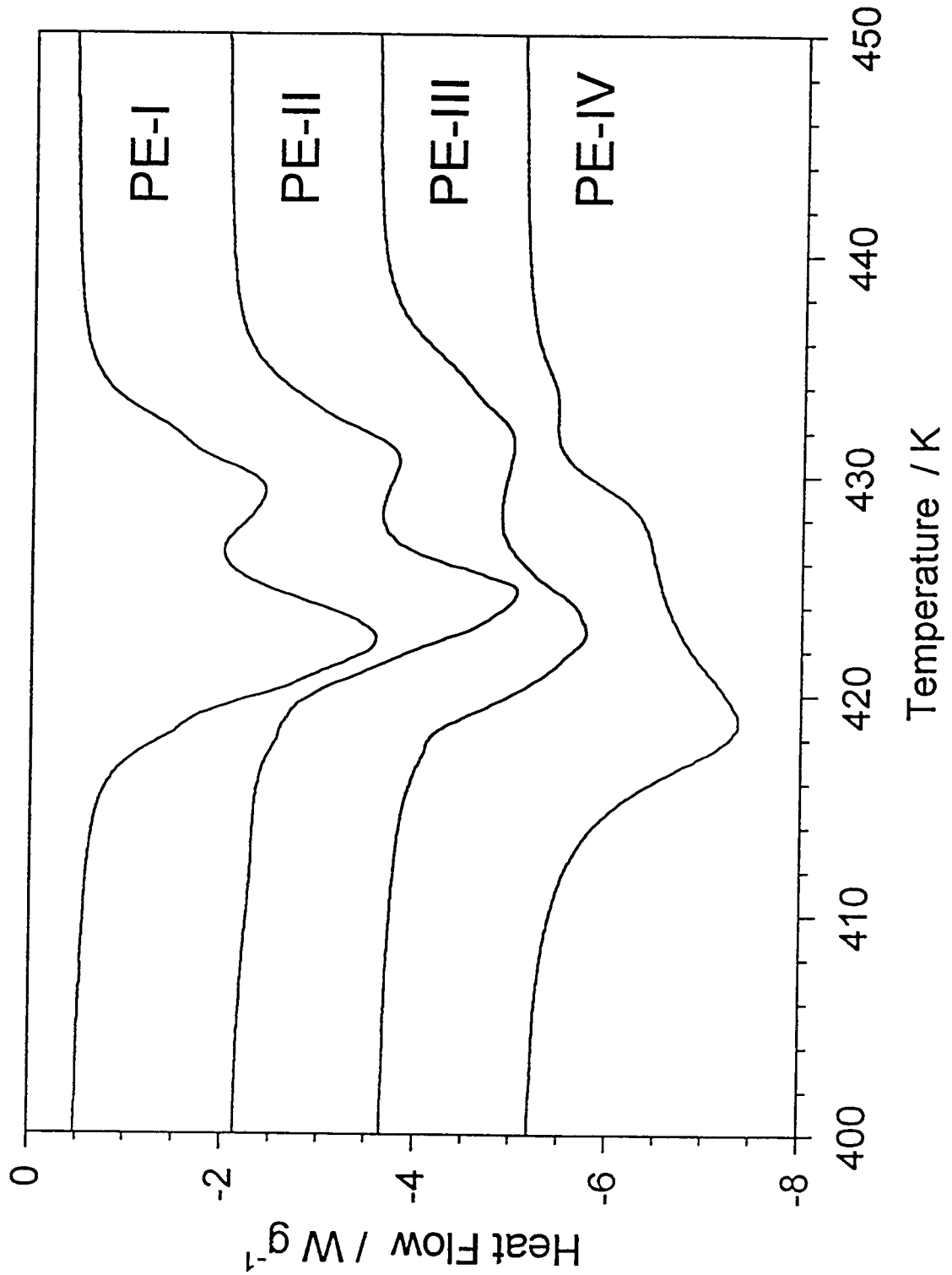

Fig. 5.2-1 Melting behavior of PE-I - IV in crimped aluminum pans heated at 10 K/min.

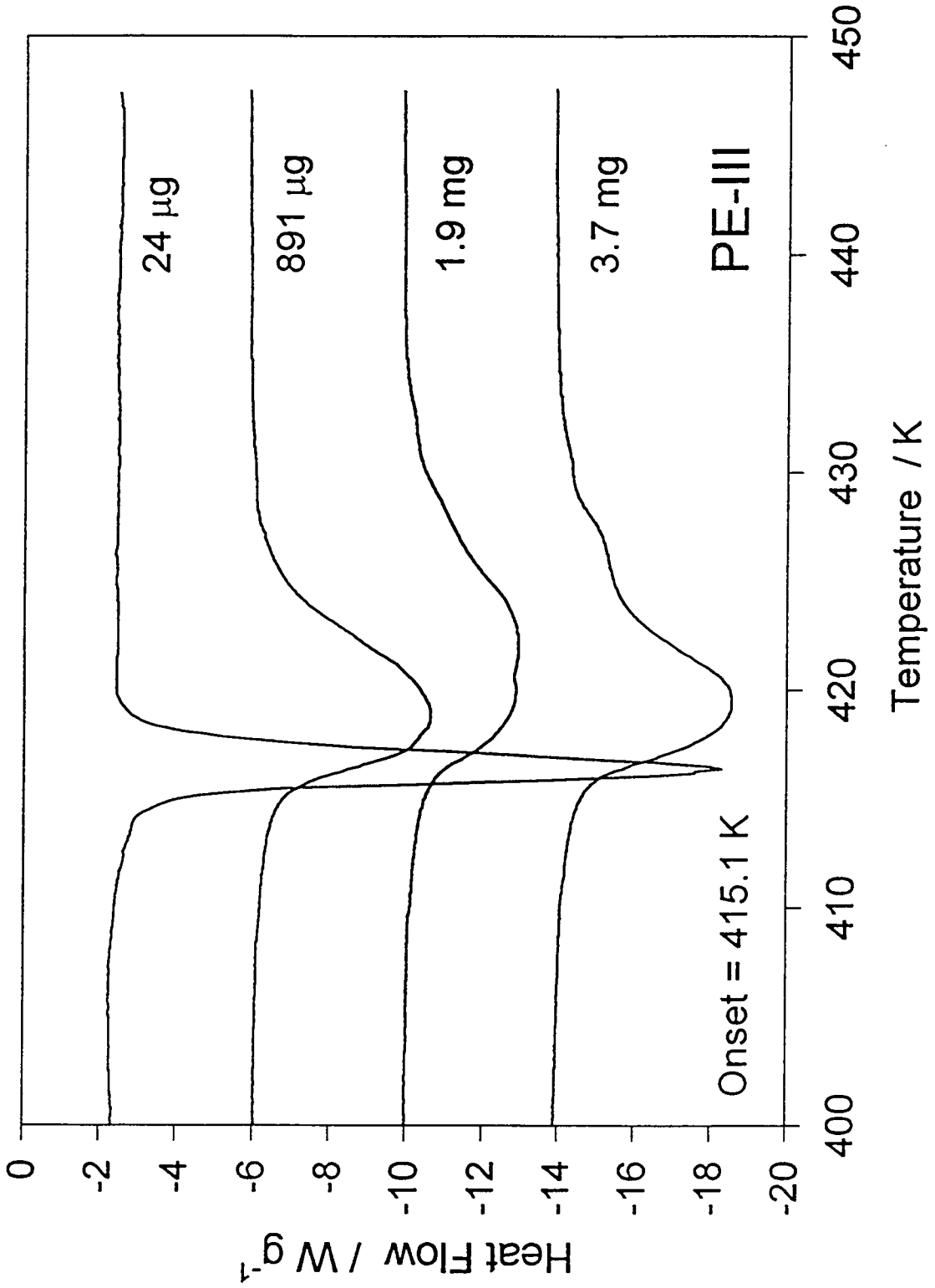

Fig. 5.2-2 Melting behavior of PE-III as a function of mass.

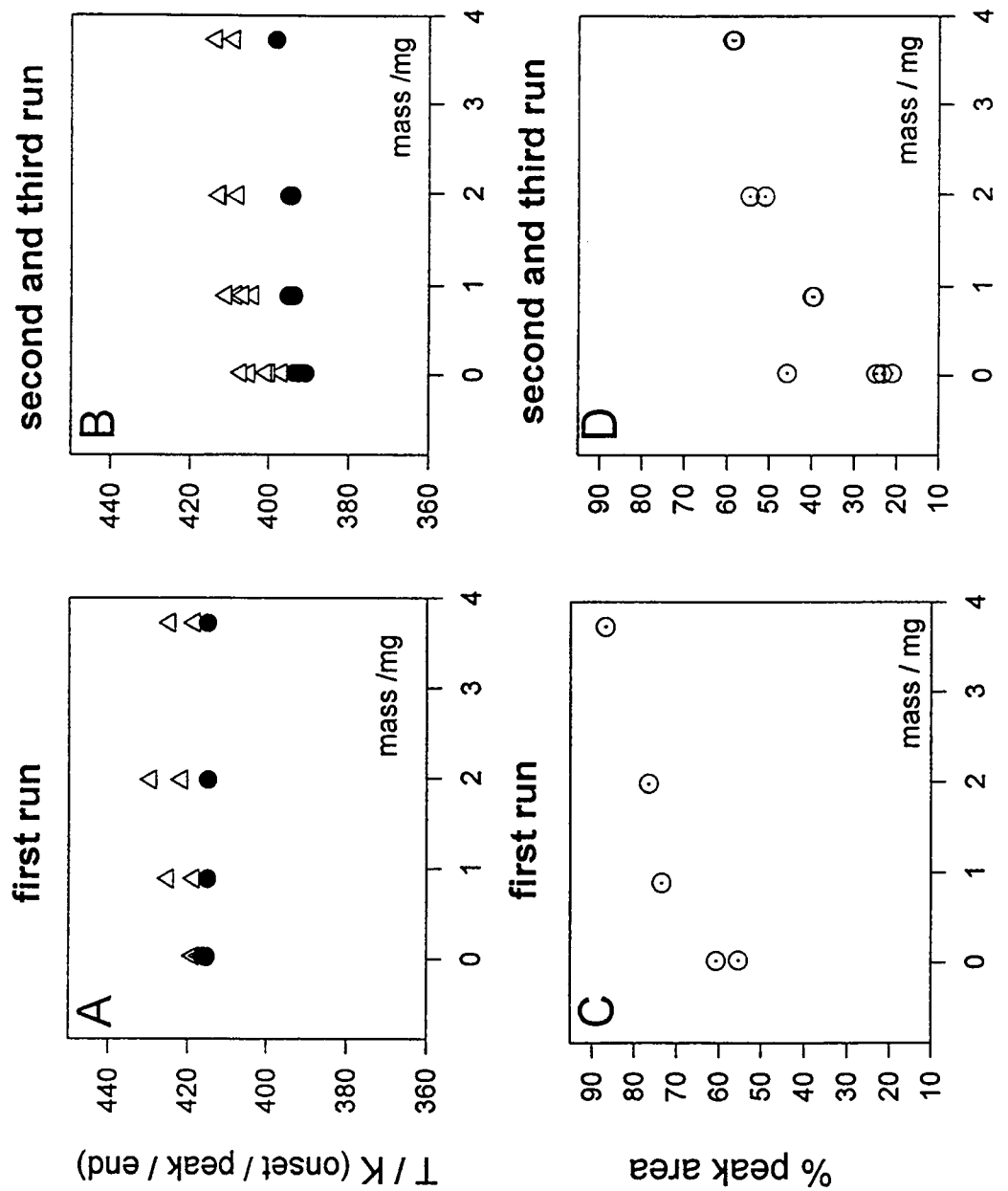

Fig. 5.2-3 Graphic representation of the variation of the temperatures at onset, peak and peak end) for PE-III as a function of mass in the first run (A) and consecutive second and third run (B). Peak areas as a percentage of a theoretical 100% crystalline PE sample in the first run (C) and consecutive second and third runs (D) (A&B solid symbol is onset)

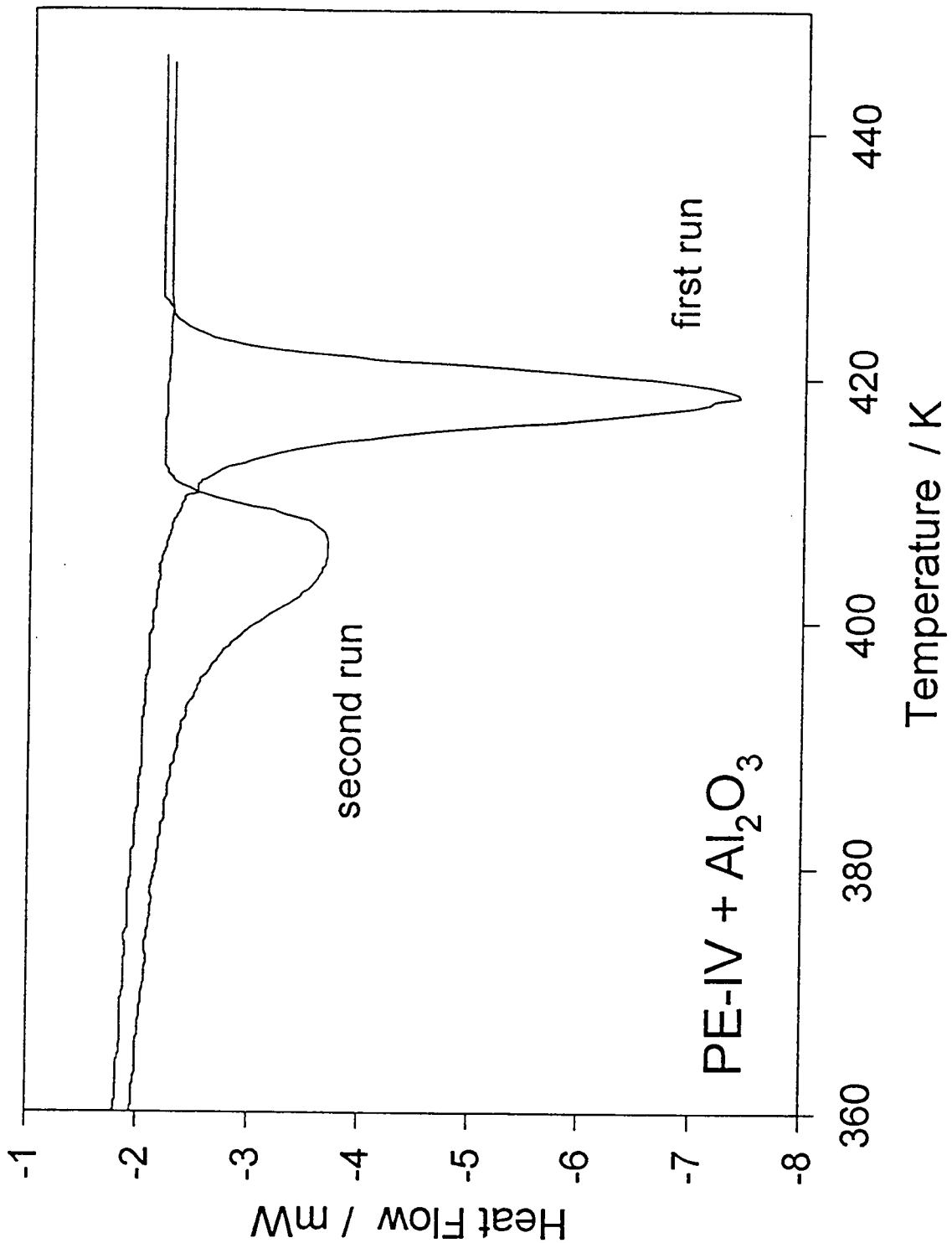

Fig. 5.2-4 Melting behavior of PE-IV (low modulus experimental fiber) with the addition of anhydrous aluminum oxide to facilitate thermal conduction.

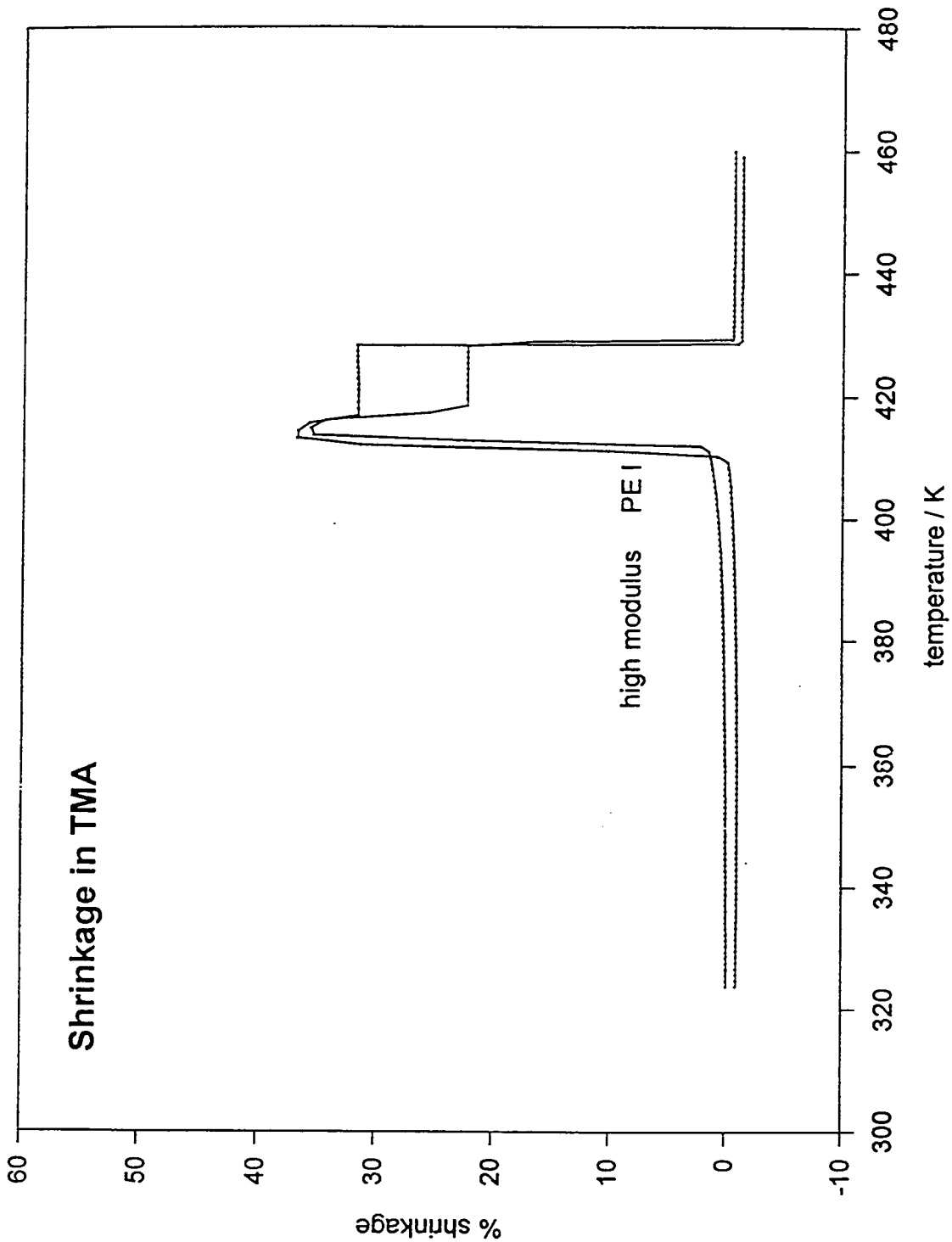

Fig. 5.3-1 Shrinkage of PE-I single filaments measured in a TMA at a heating rate of 10 K/min. Results of two experiments.

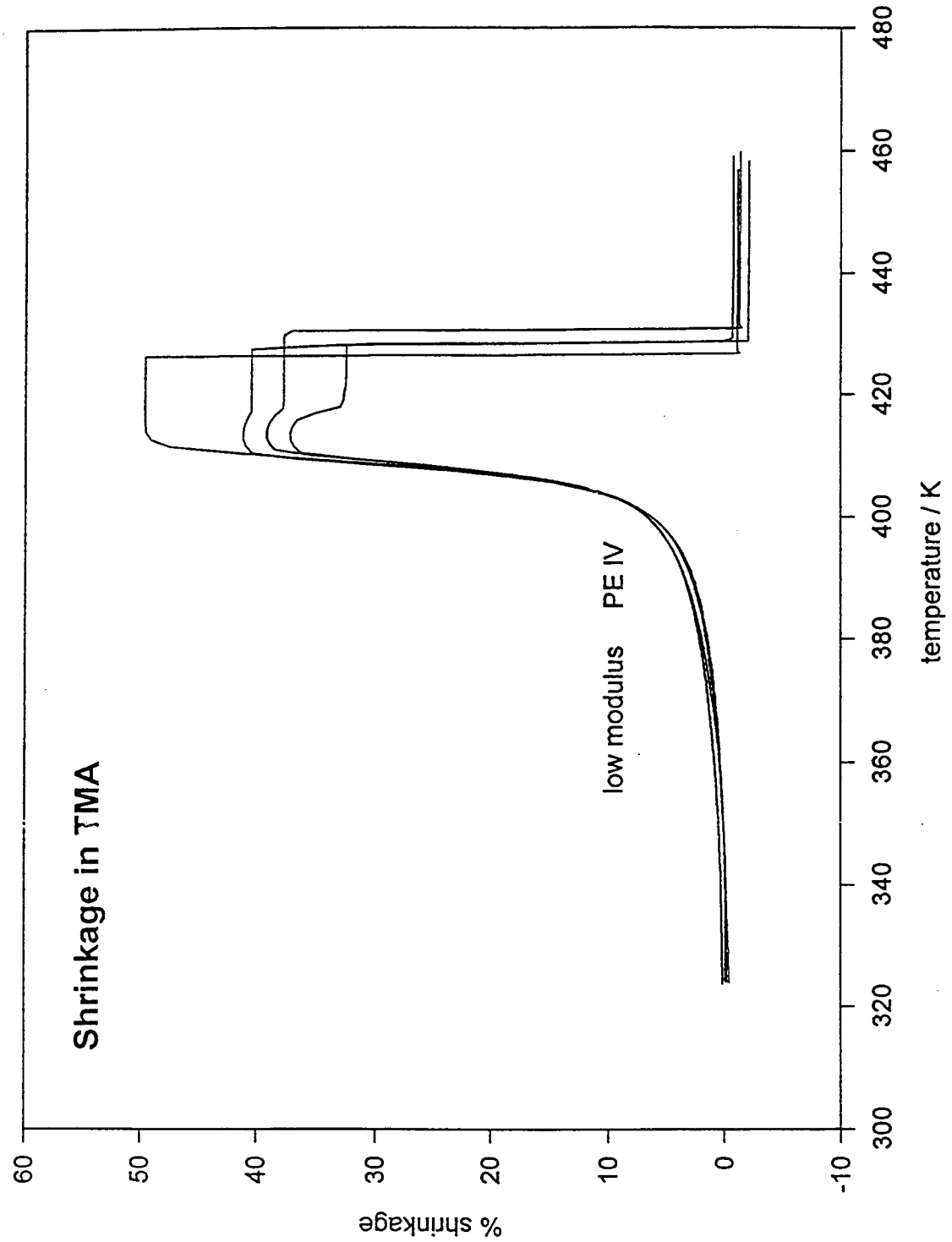

Fig. 5.3-2 Shrinkage of PE-IV single filaments measured in a TMA at a heating rate of 10 K/min. Results of four experiments.

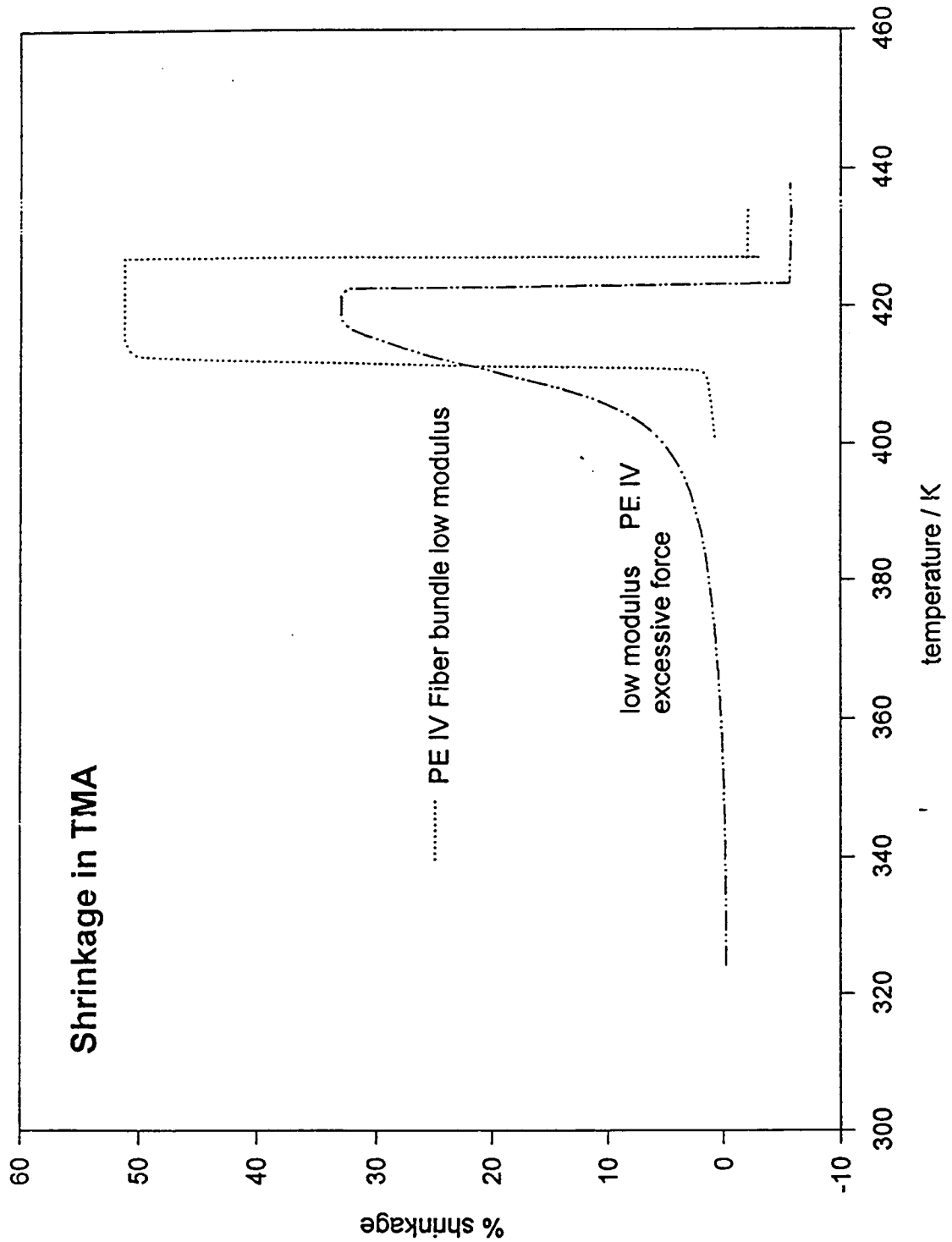

Fig. 5.3-3 Shrinkage of PE-IV filaments measured in a TMA at a heating rate of 10 K/min. Dotted line for fiber bundle, dash-dotted line for single filament (excessive force in experimental set-up).

Fig. 5.4-1 PE-I fibers (60x) before (A) and after (B) shrinkage.

A

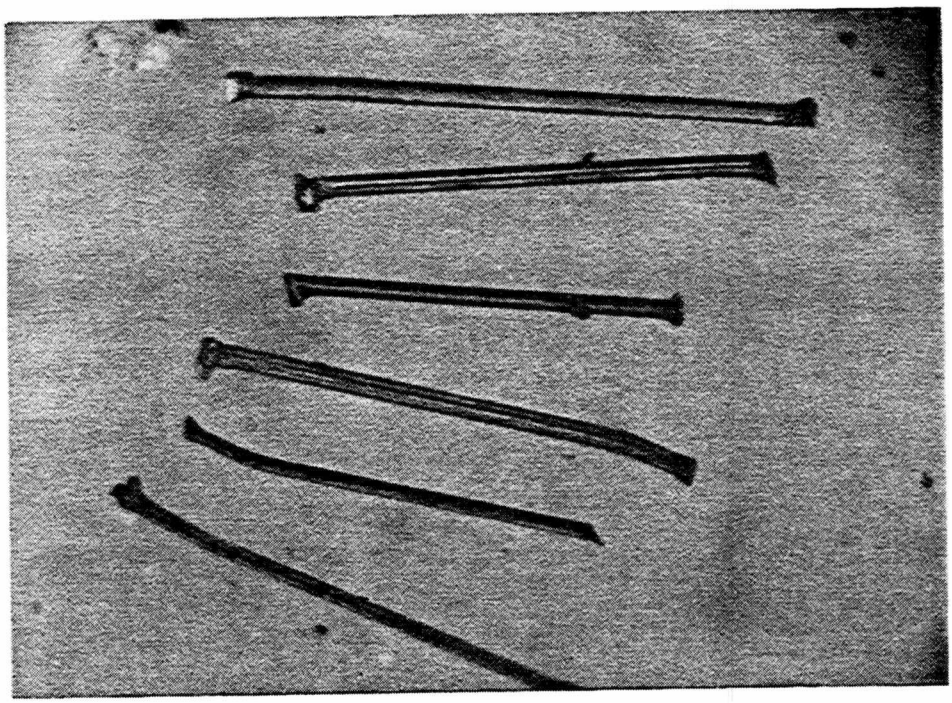

B

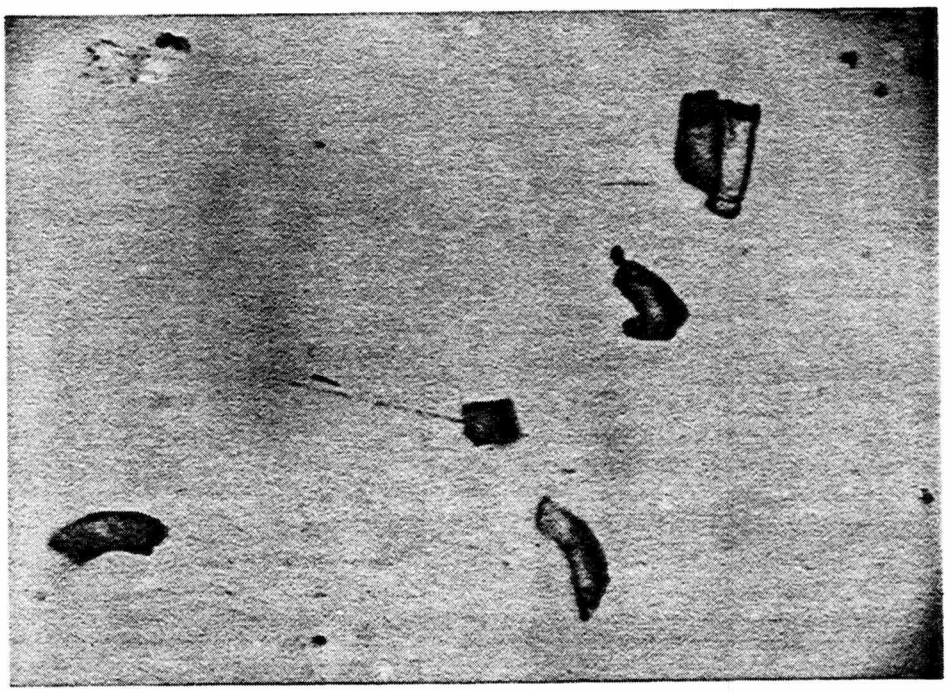

Fig. 5.4-1

Fig. 5.4-2 PE-III fibers (60x) before (A) and after (B) shrinkage.

A

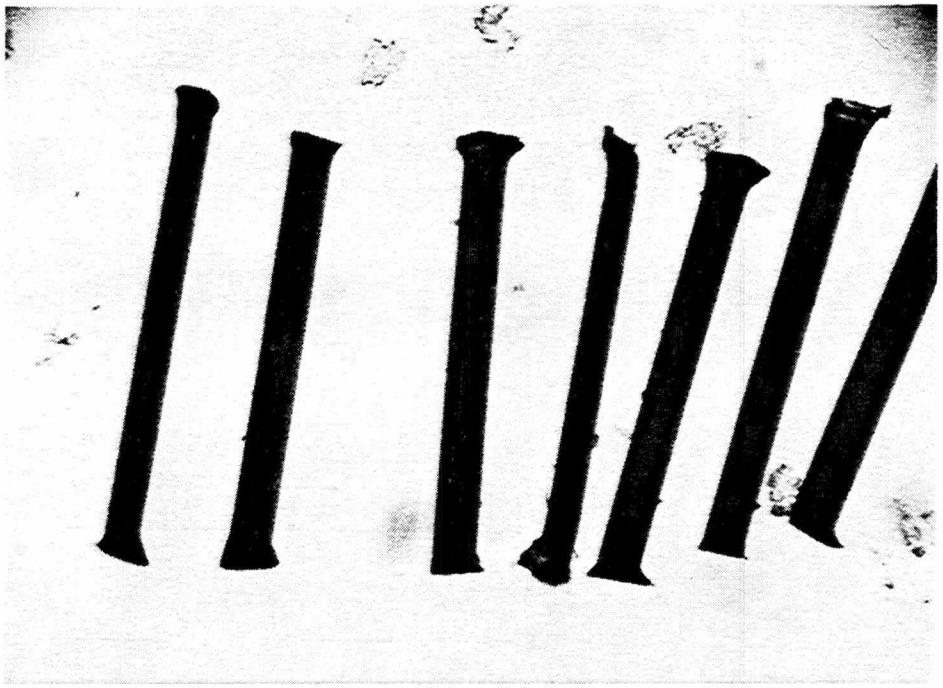

B

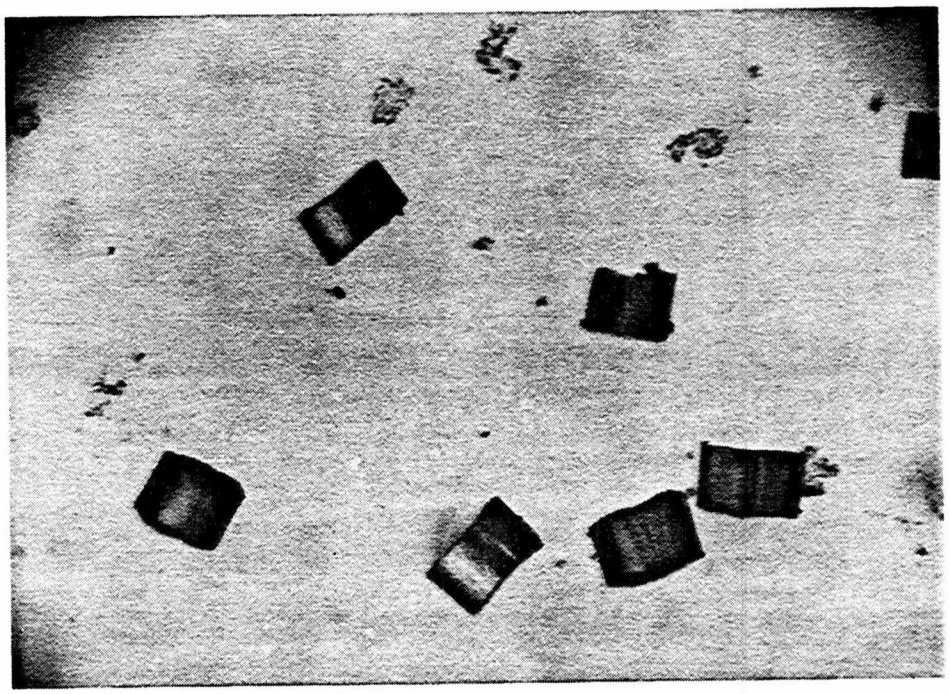

Fig. 5.4-2

Fig. 5.4-3 Sample preparation documentation for 1.5 mg sample (25x). (A) crossed polars enhance "full" sample pan, (B) reflection on the aluminum enhances the "empty" sample pan impression.

A

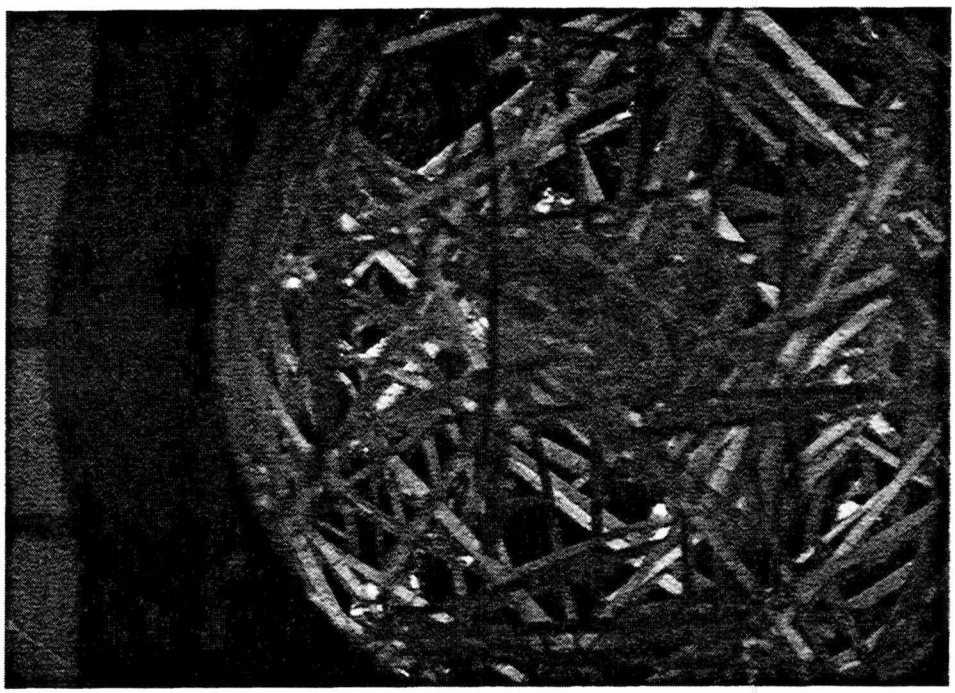

B

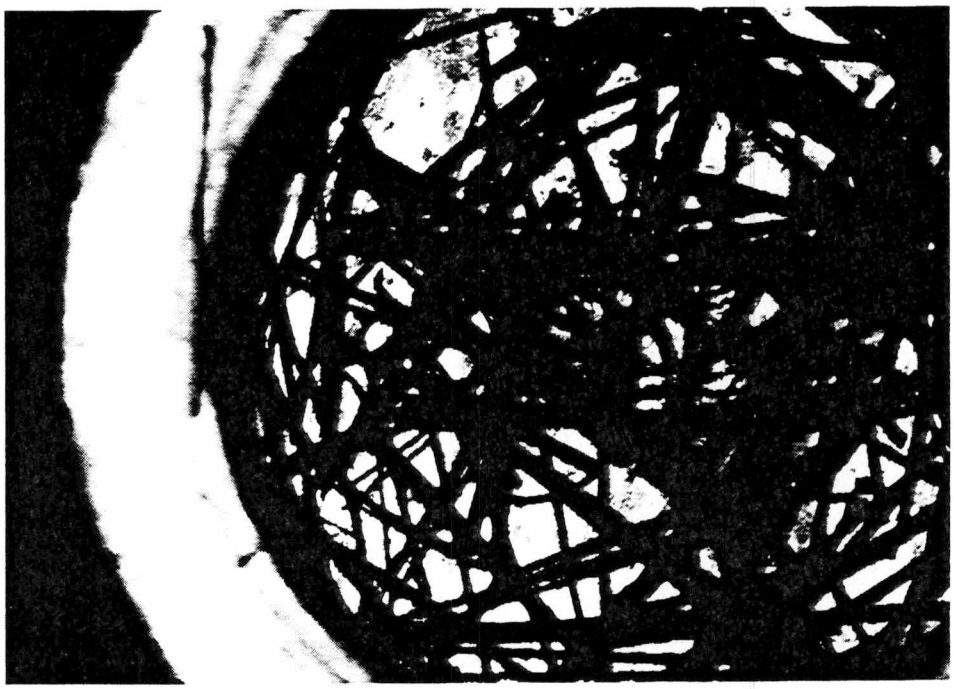

Fig. 5.4-3

Fig. 5.4-4 Sample preparation documentation for (A) 24 μg and (B) 0.5 mg sample (25x).

A

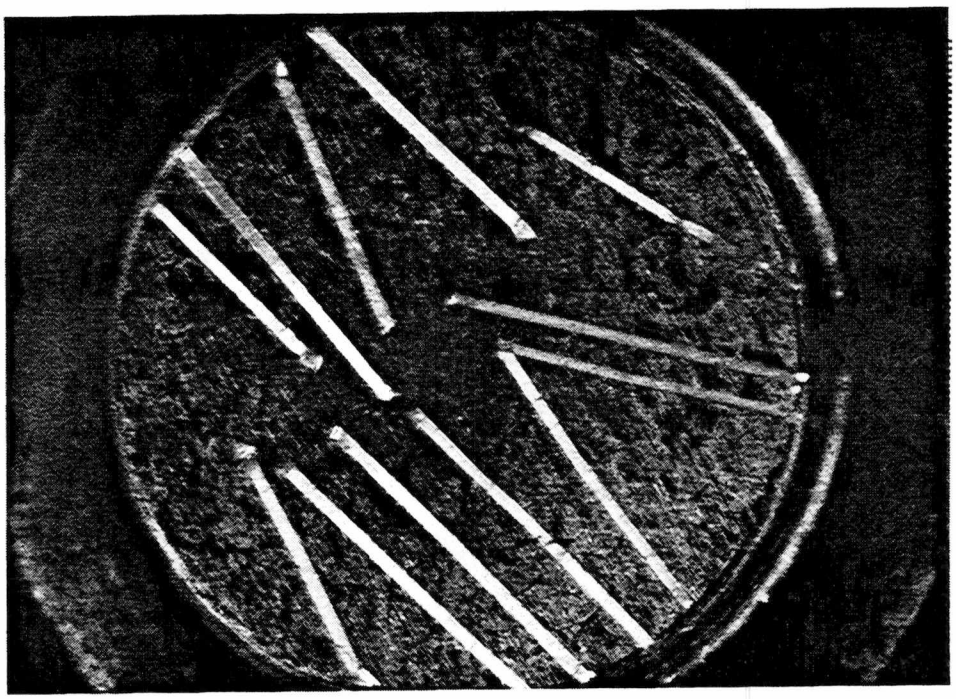

B

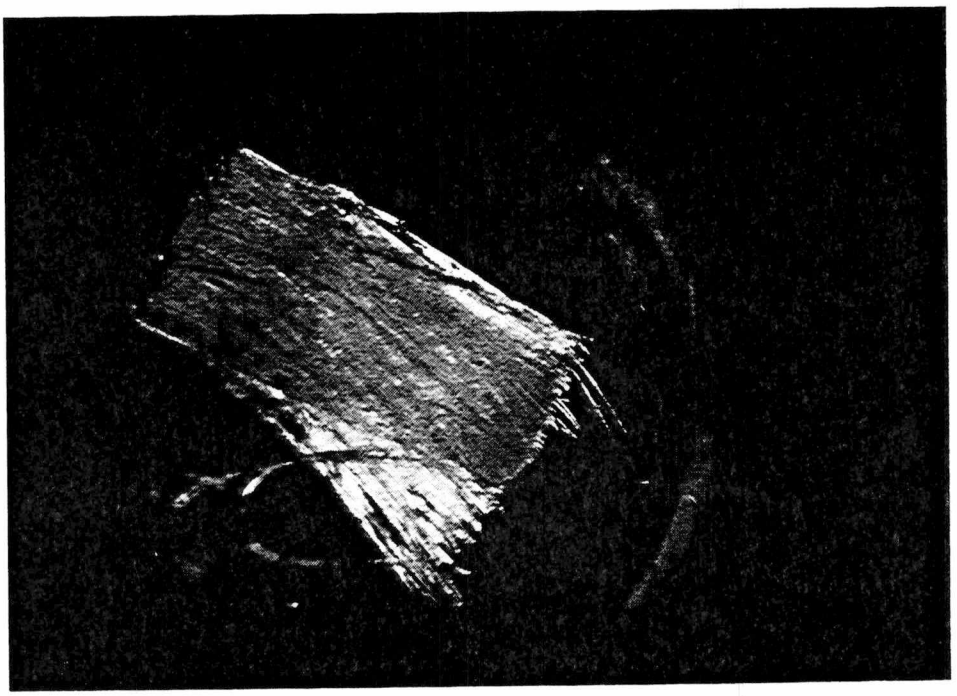

Fig. 5.4-4

Fig. 5.4-5 Sample preparation documentation for PE-IV sample with aluminum oxide powder (25x). (A) partially covered fibers, (B) finished sample.

A

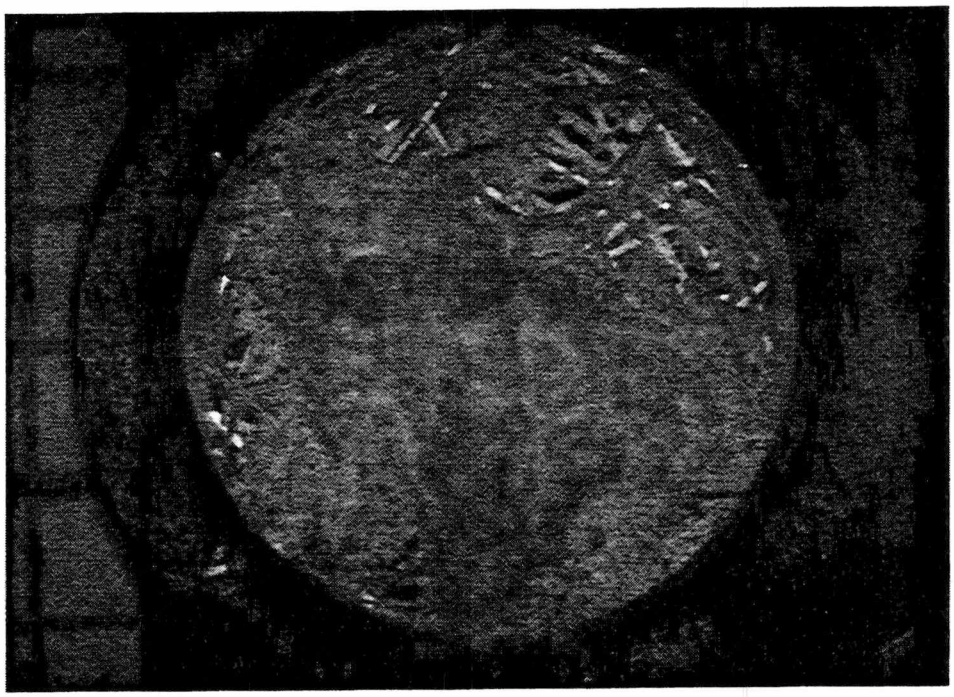

B

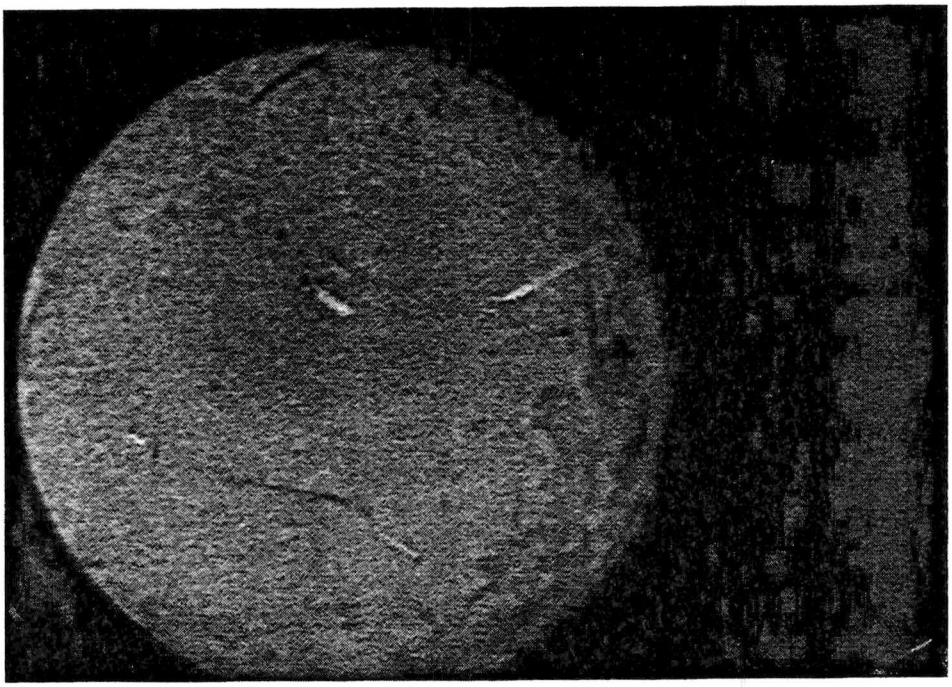

Fig. 5.4-5

Fig. 5.4-6 Documentation of constrained melting effects (A) Before melting (B) after melting.

A

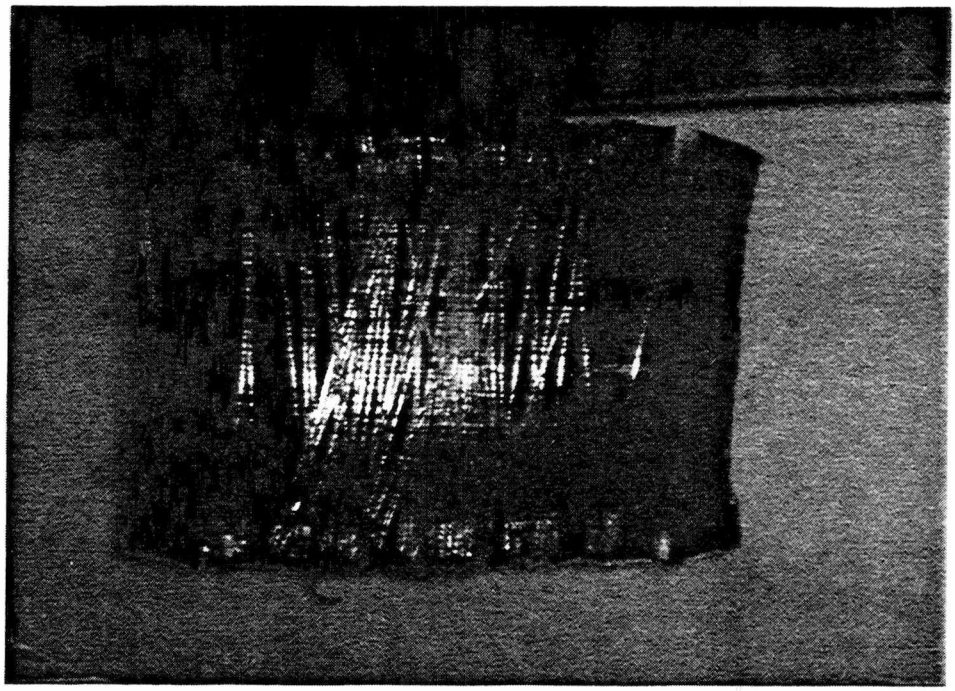

B

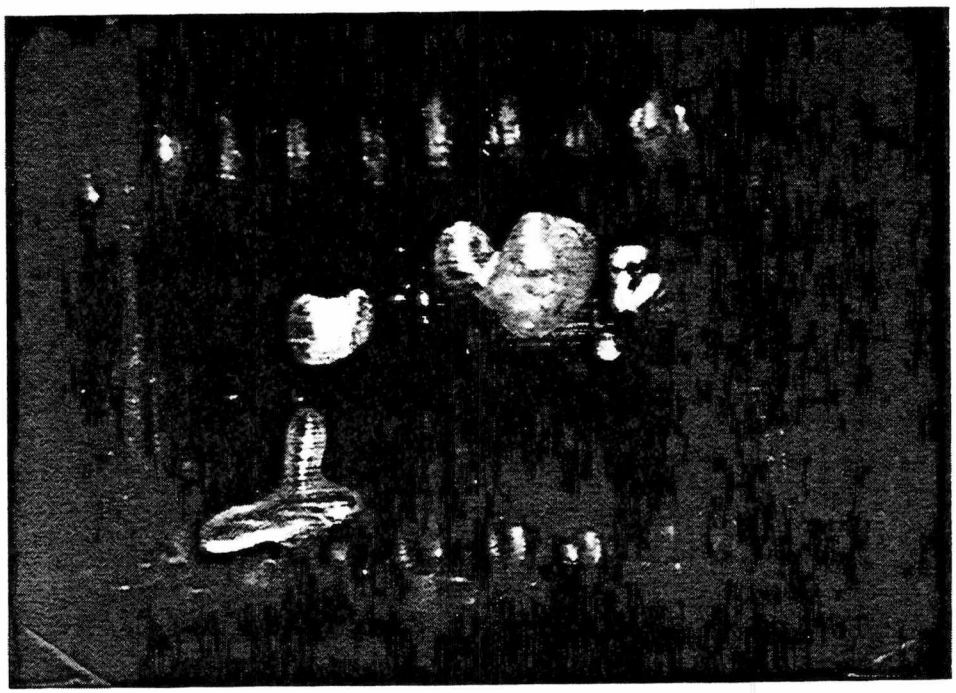

Fig. 5.4-6

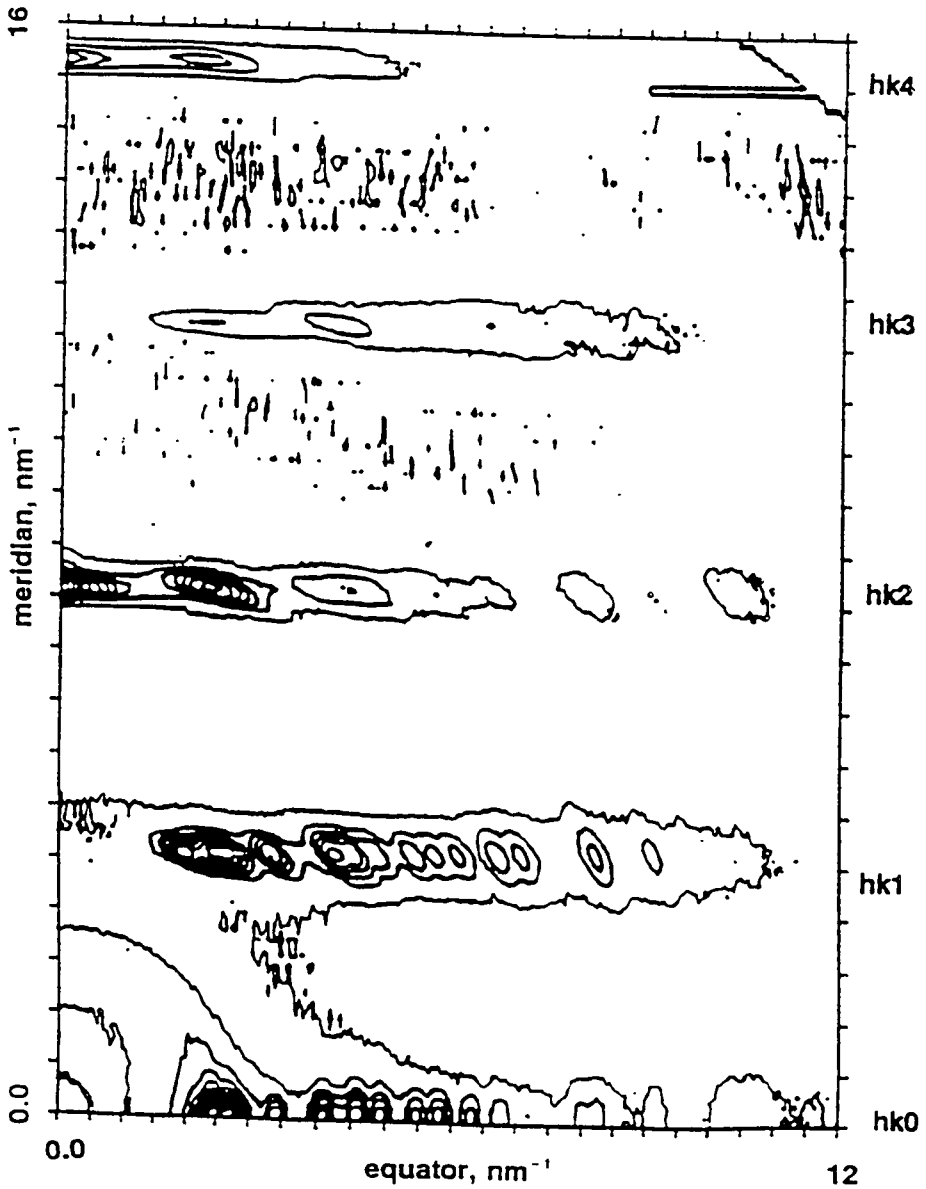

Fig. 5.5-1 Contour plot of the observed two-dimensional fiber diffraction pattern of sample PE-III. Successive contour lines are $0.1^{1/8}$ times higher in intensity.

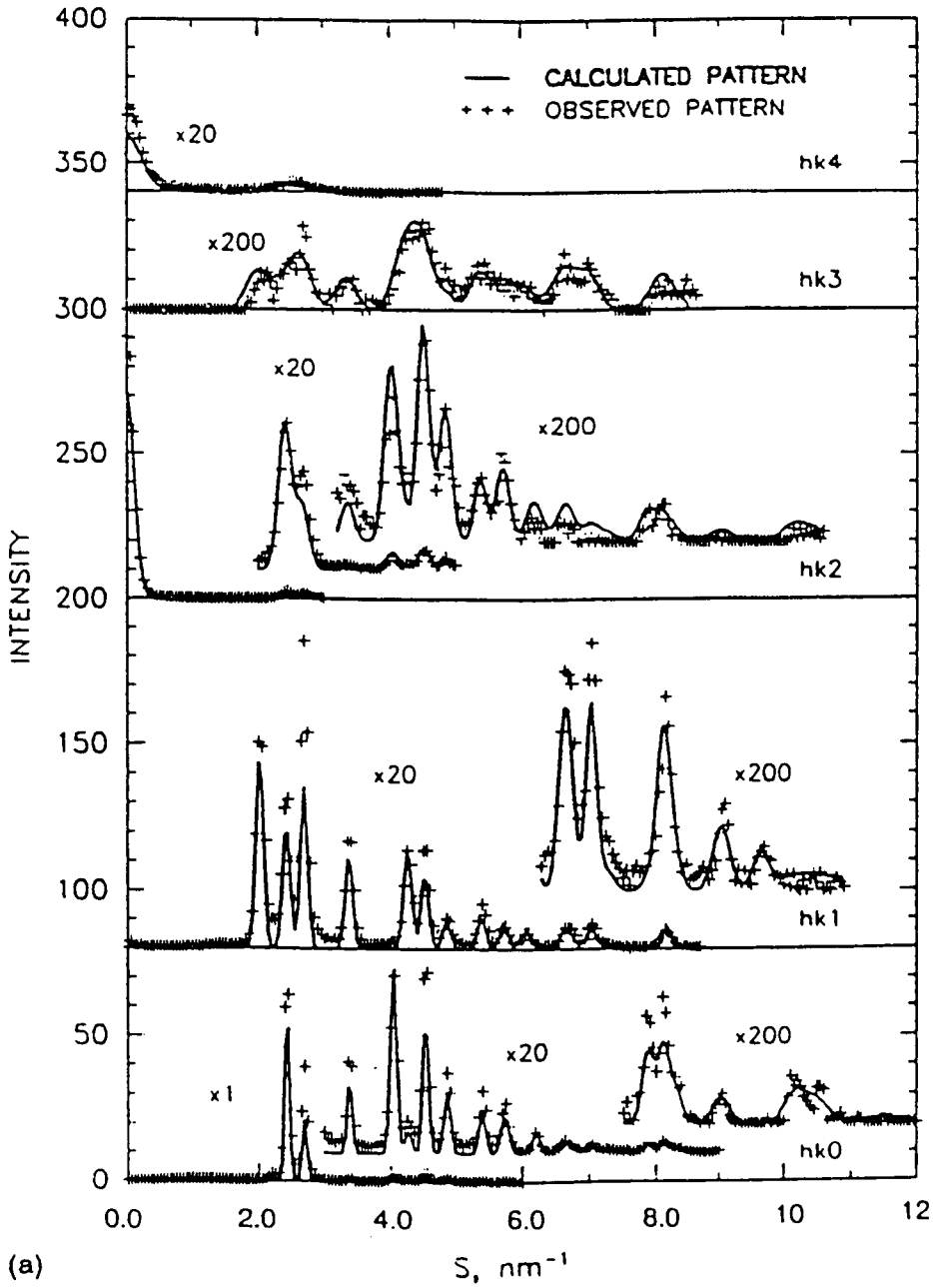

Fig. 5.5-2 Comparison of the intensities of the observed fiber diffraction and calculated orthorhombic crystalline diffraction along the layer lines. The data are plotted on different scales, as indicated in the figure. (A) PE-I; (B) PE-II; (C) PE-IIII; and (D) PE-IV.

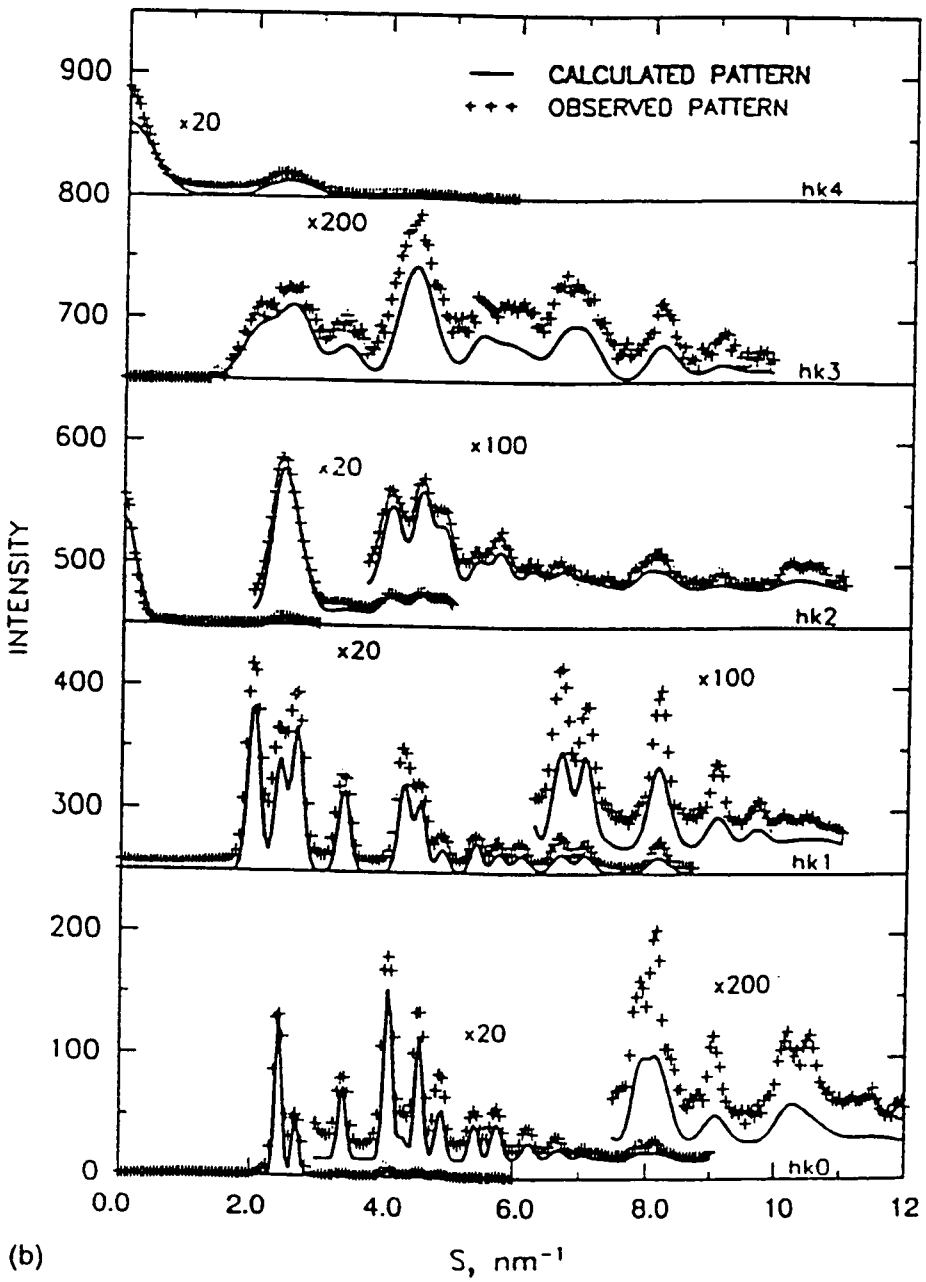
CALCULATED PATTERN
OBSERVED PATTERN
x20
hk4
x200
hk3
x100
x20
hk2
x20
x100
hk1
x200
x20
hk0
INTENSITY
900
800
700
600
500
400
300
200
100
0
0.0
2.0
4.0
6.0
8.0
10
12
S, nm⁻¹
(b)

Fig. 5.5-2 (B)

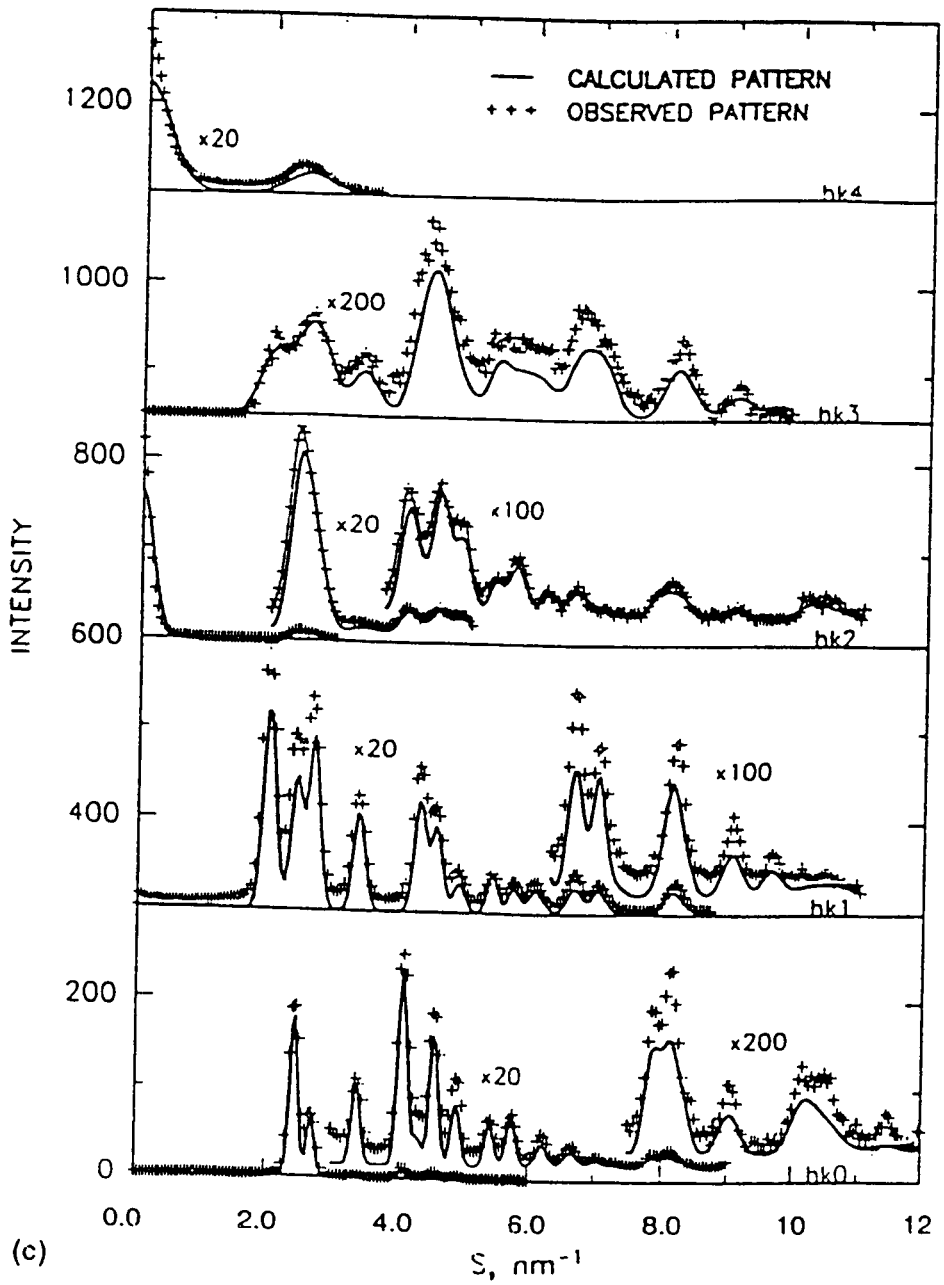
CALCULATED PATTERN
OBSERVED PATTERN
INTENSITY
1200
1000
800
600
400
200
0
x20
x200
x100
hk4
hk3
hk2
hk1
hk0
0.0
2.0
4.0
6.0
8.0
10
12
S, nm⁻¹
(c)

Fig. 5.5-2 (C)

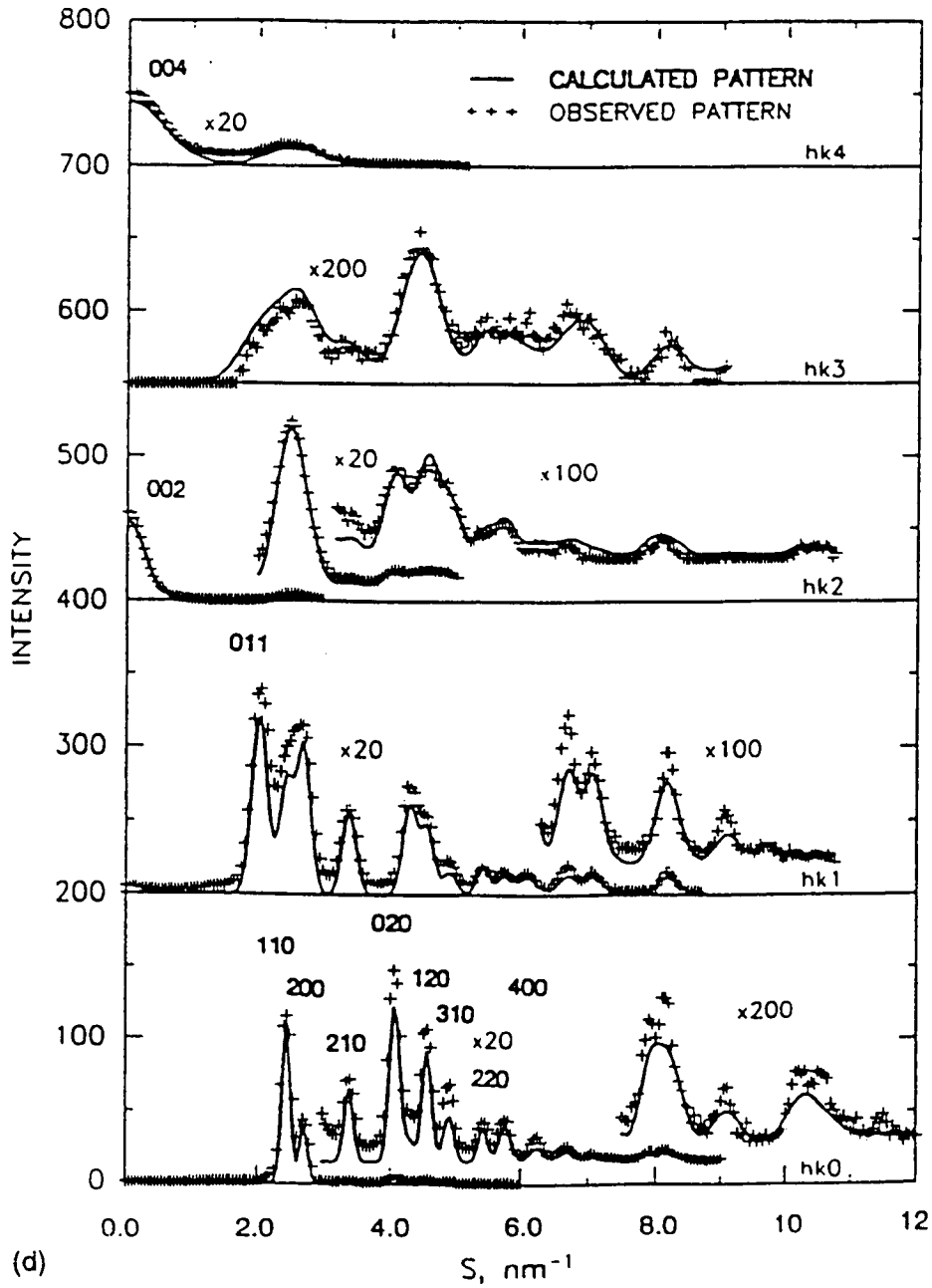
800
700
600
500
400
300
200
100
0
INTENSITY
004
x20
CALCULATED PATTERN
OBSERVED PATTERN
hk4
x200
hk3
002
x20
x100
hk2
011
x20
x100
hk1
020
110
200
120
400
310
210
x20
220
x200
hk0
0.0
2.0
4.0
6.0
8.0
10
12
S, nm⁻¹
(d)

Fig. 5.5-2 (D)

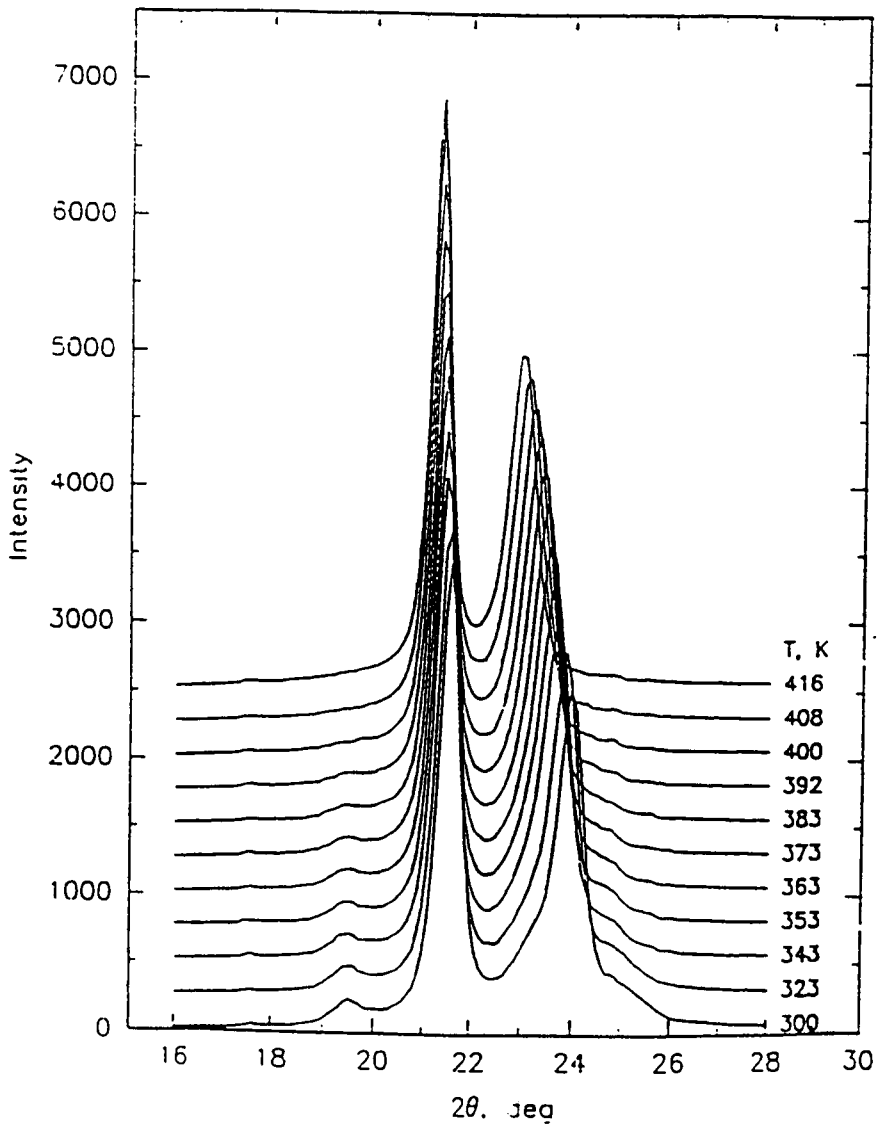

Fig. 5.5-3 Powder x-ray diffraction patterns of sample PE-I as a function of temperature. The small peak at 19.5° is due to the monoclinic 010 reflection; the peaks at 21.5° and 23.5° (at 300 K) are the orthorhombic 110 and 200 reflections.

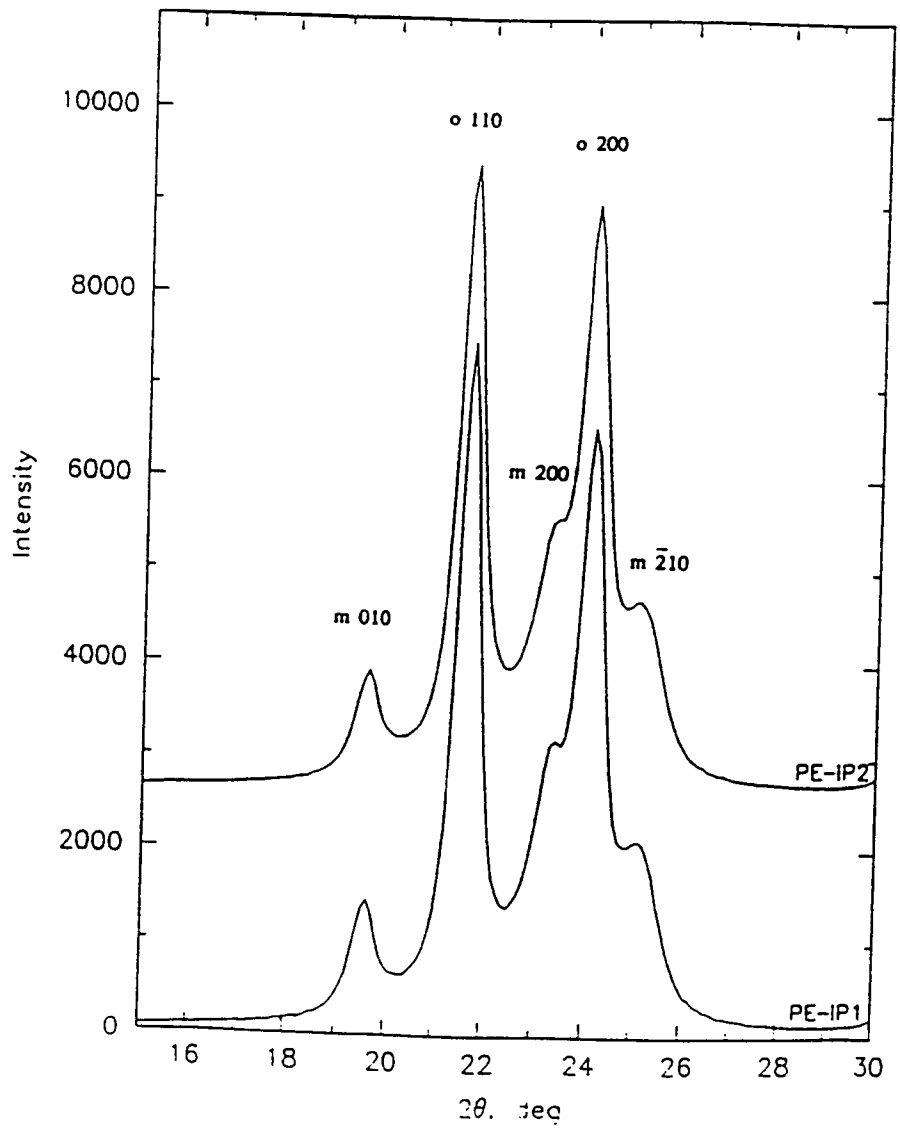

Fig. 5.5-4 Powder x-ray diffraction patterns of the compressed PE-I fibers showing an increase in the intensities of the monoclinic reflections.

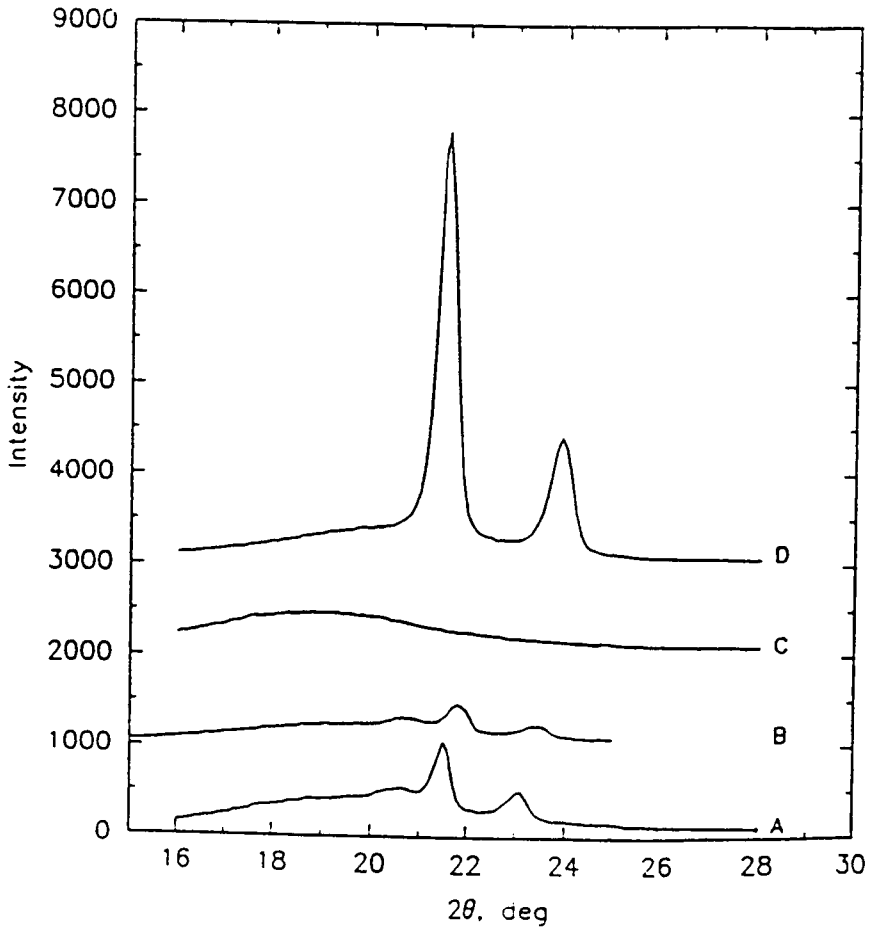

Fig. 5.5-5 Powder x-ray diffraction patterns of sample PE-I at (A) 418 K; (B) 423 K; (C) 429 K; and of a recrystallized molten sample analyzed at 300 K (D).

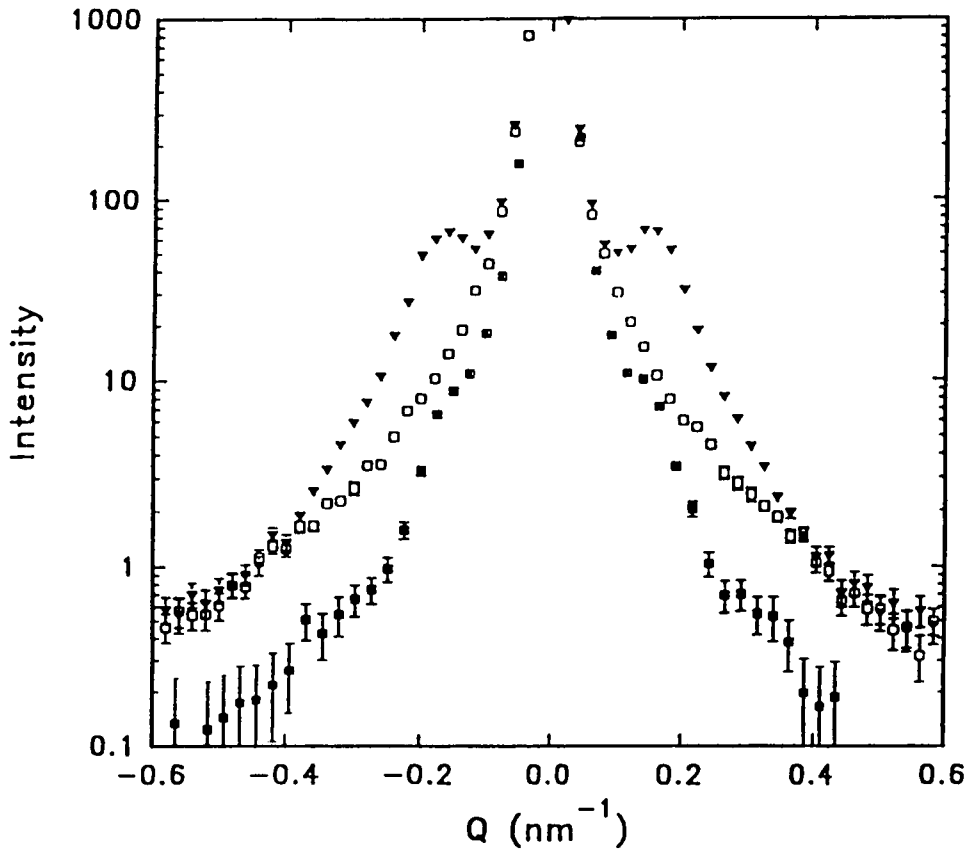

Fig. 5.5-6 Meridional SAXS intensities and error range for samples PE-II (▼), PE-III (❑), and PE-IV (■). Scattering intensity scale is arbitrary.

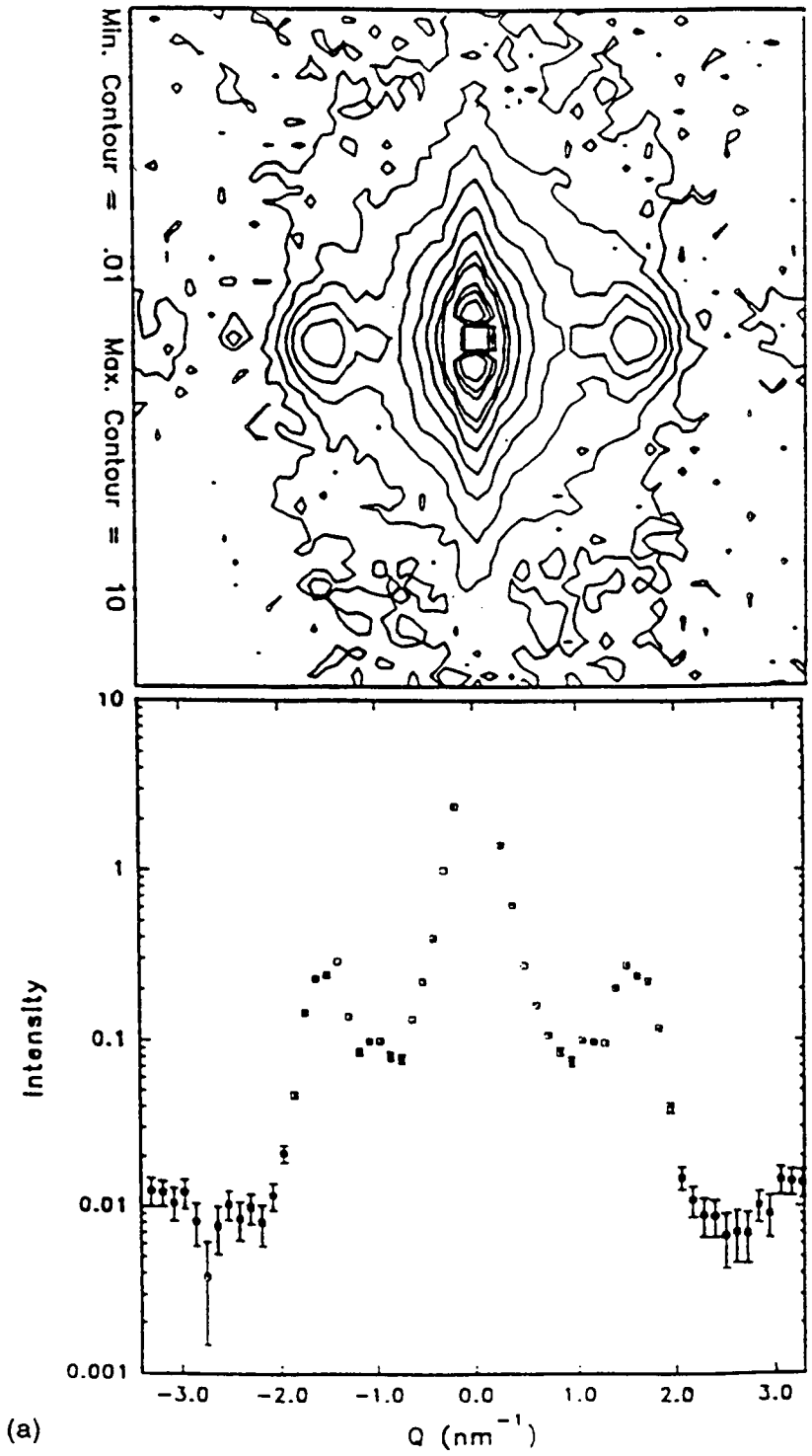

Fig. 5.5-7 Contours and meridional SAXS intensities of (A) sample PE-I and (B) sample PE-V. The horizontal axis is approximately parallel to the meridian (z) and the vertical axis is approximately parallel to the equator (s). Scattering intensity scale is arbitrary.

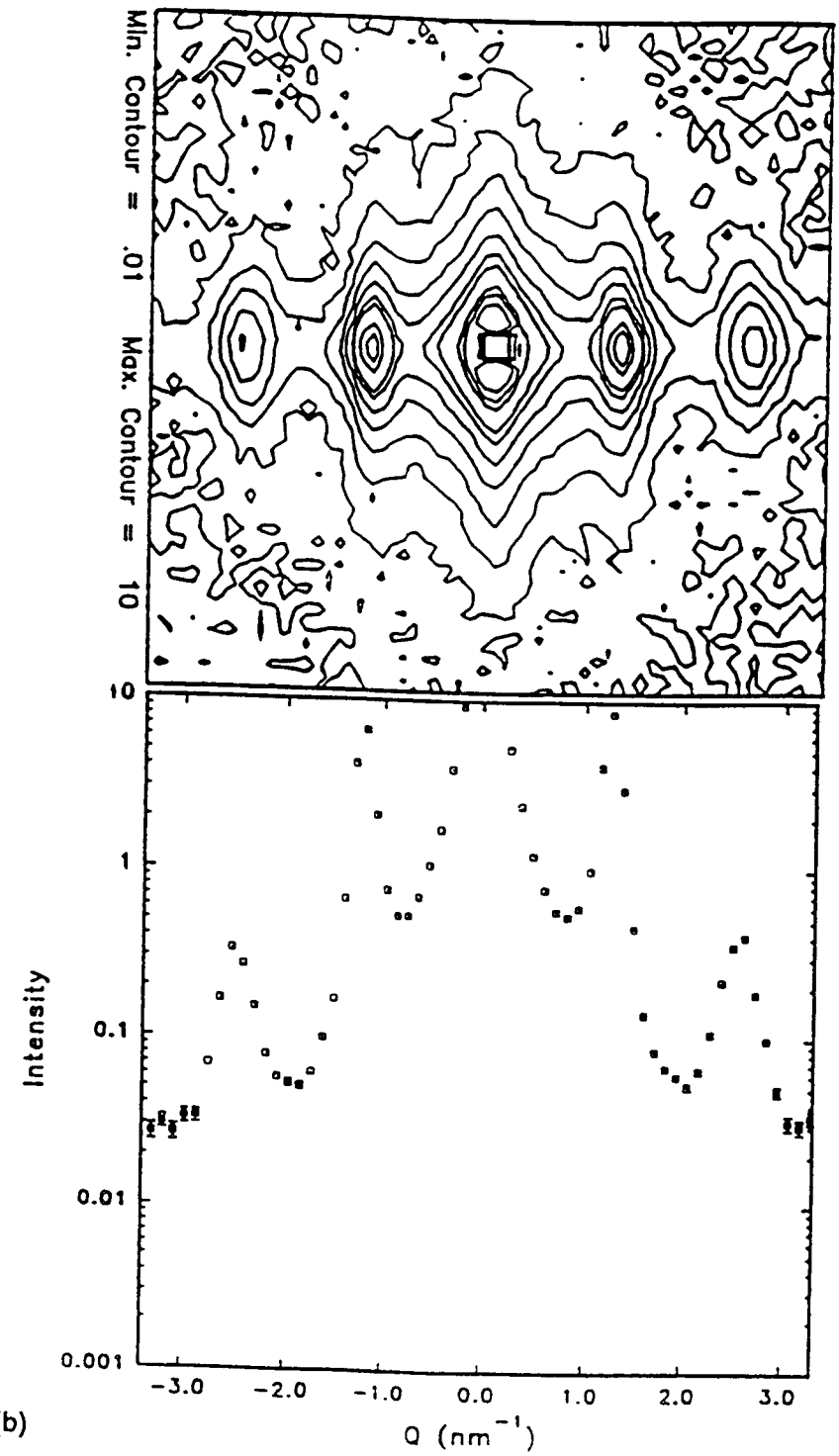
Min. Contour = .01
Max. Contour = 10
10
1
0.1
0.01
0.001
Intensity
-3.0
-2.0
-1.0
0.0
1.0
2.0
3.0
Q (nm^{-1})

(b)

Fig. 5.5-7 (B)

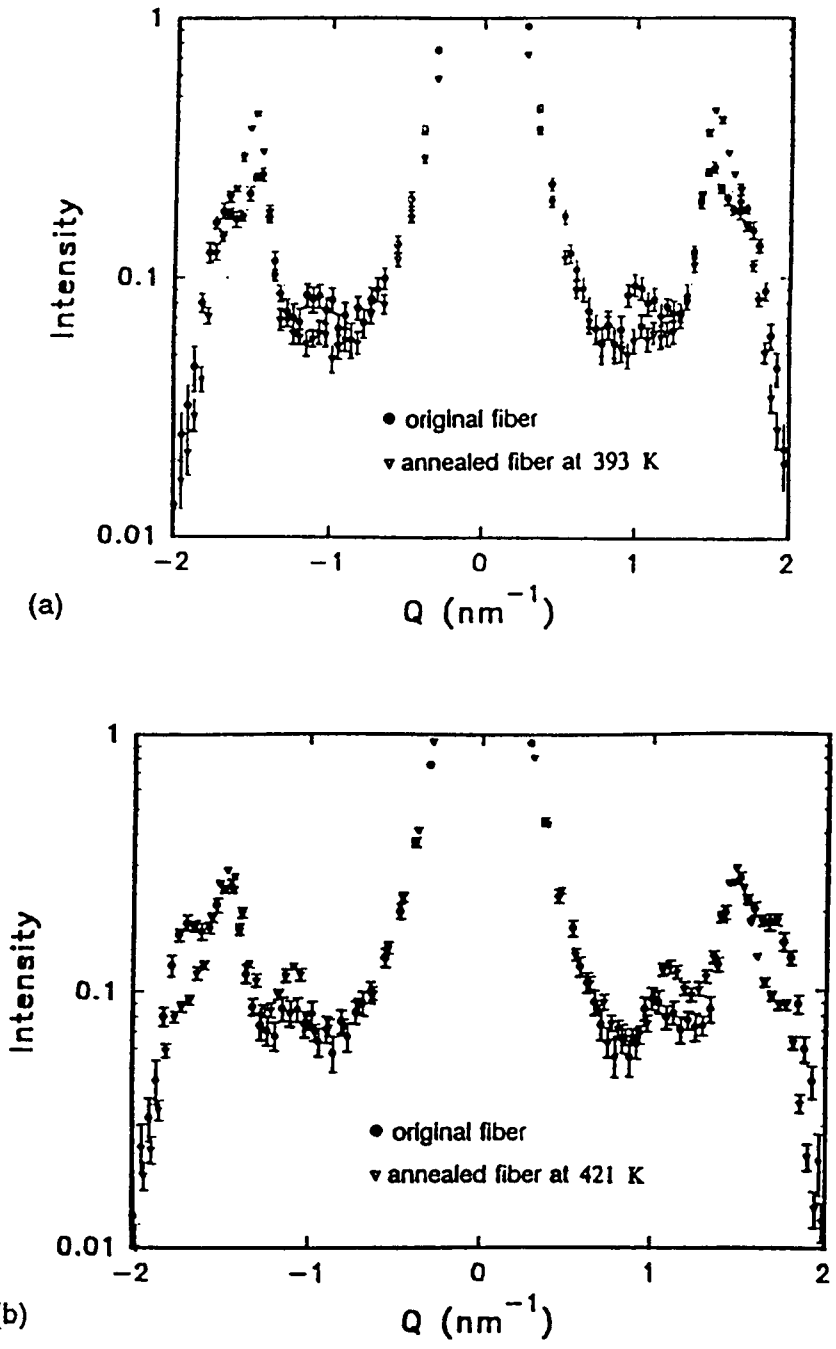

Fig. 5.5-8 Comparison of meridional SAXS intensities of the original and annealed PE-I samples at 393 and 421 K. Scattering intensity scale is arbitrary.

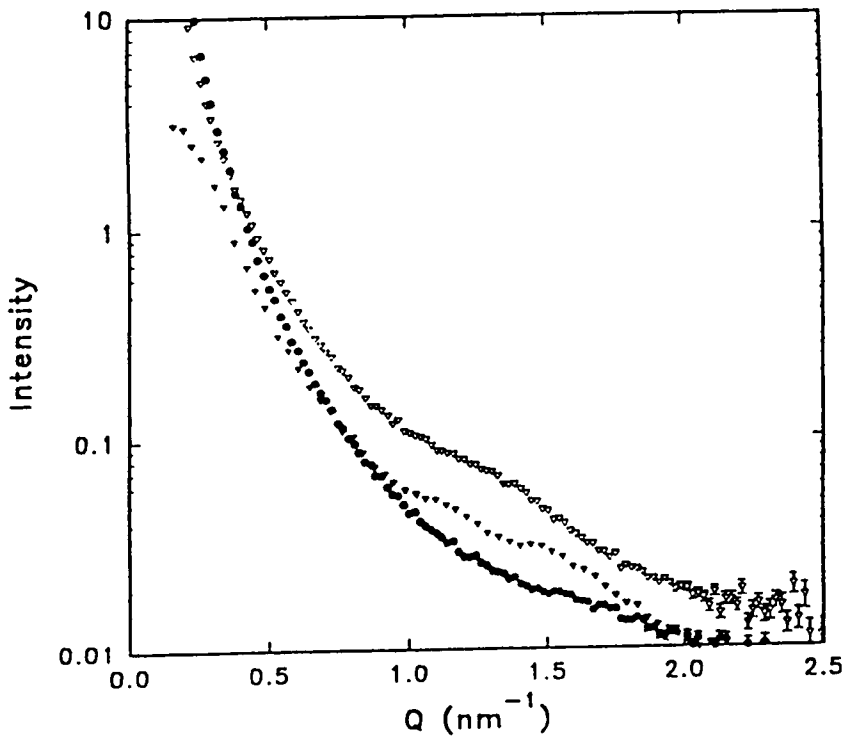

Fig. 5.5-9 Comparison of the meridional SAXS intensities of randomly oriented cut PE-I fibers (▼), recrystallized PE-I from the melt (●) and recrystallized PE-V from the melt (▽).

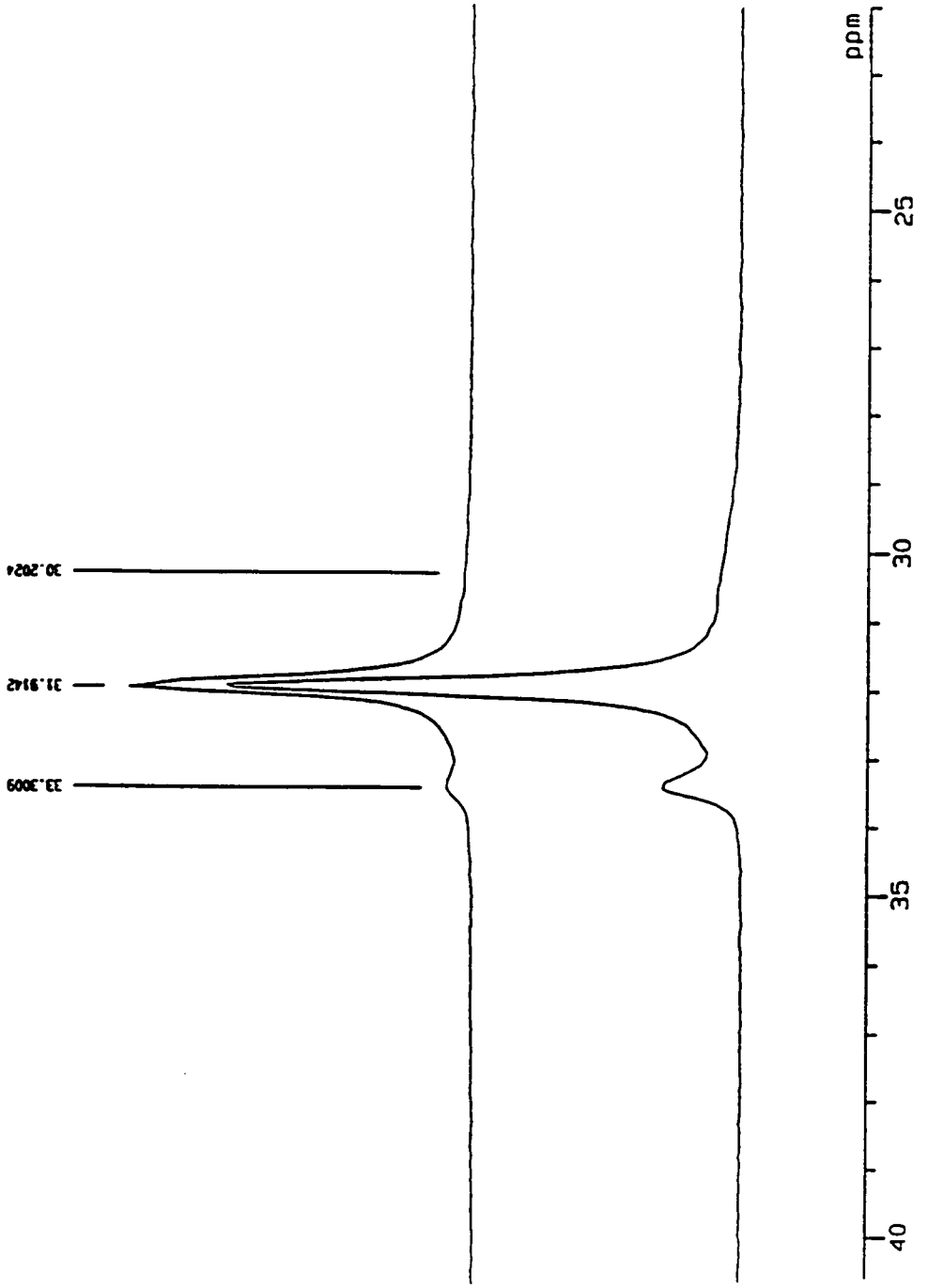

Fig. 5.6-1 The ^{13}C CP-MAS NMR spectra of samples PE-I tob and PE-IV (bottom). The three marked peaks are due to monoclinic crystals, orthorhombic crystals, and the amorphous phase (left-to-right).

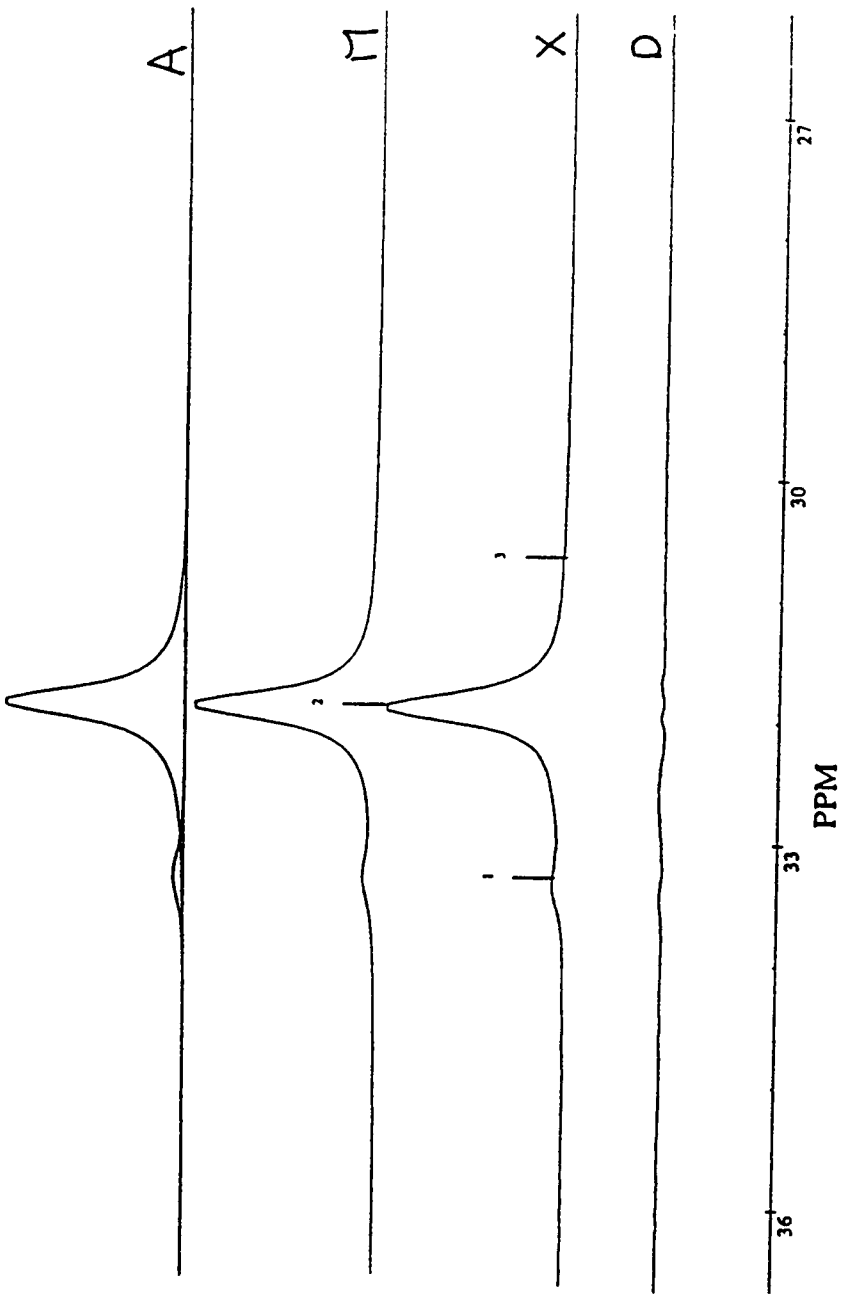

Fig. 5.6-2 The line deconvolution of ^{13}C CP-MAS NMR spectra of sample PE-I. Curves A are the computer simulations of the orthorhombic, monoclinic, and amorphous phases; curve M is the sum of the three components of A; curve X represents the experimental spectrum; curve D is the difference between X and M.

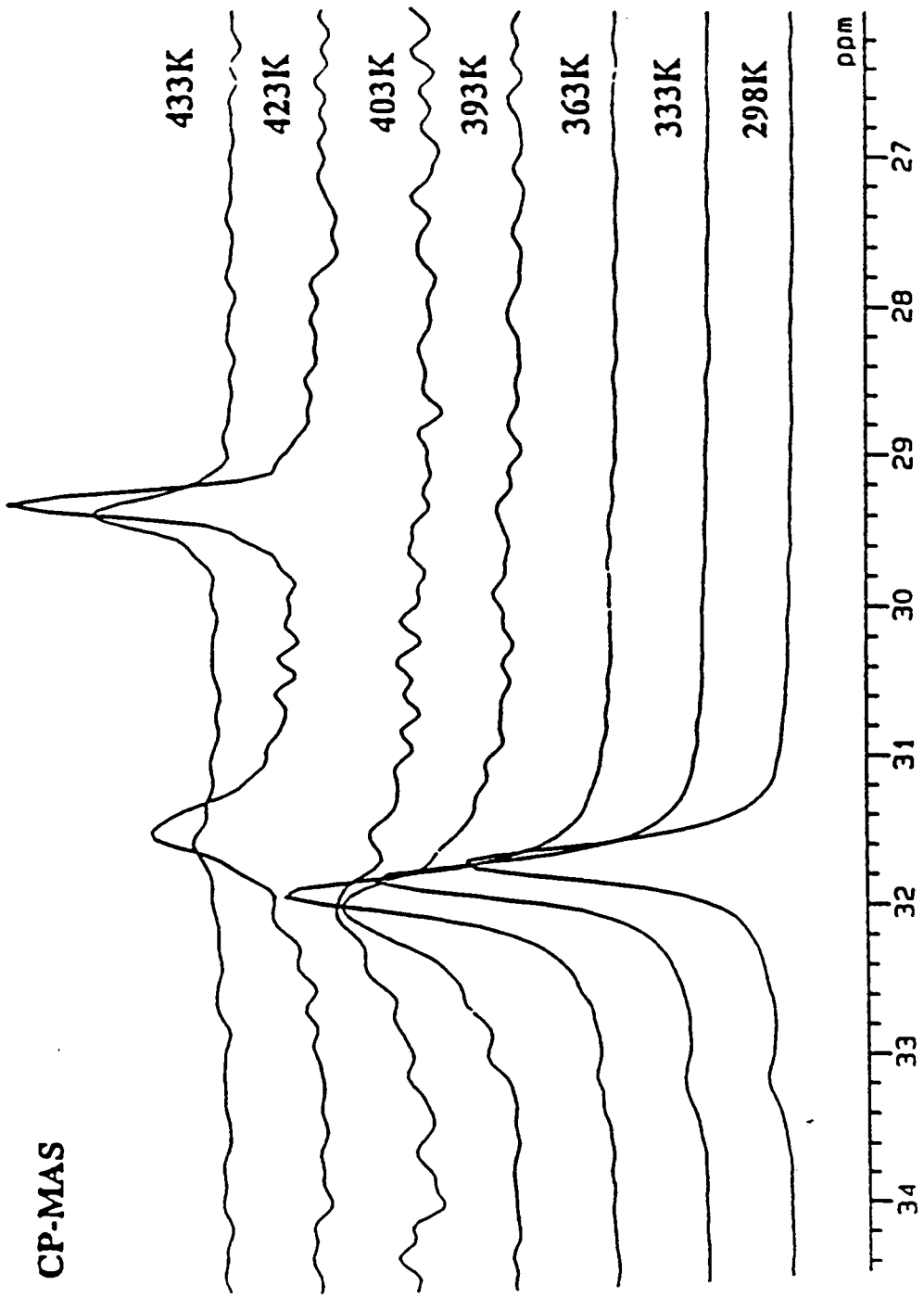

Fig. 5.6-3 The ^{13}C CP-MAS NMR spectra of sample PE-I as a function of temperature.

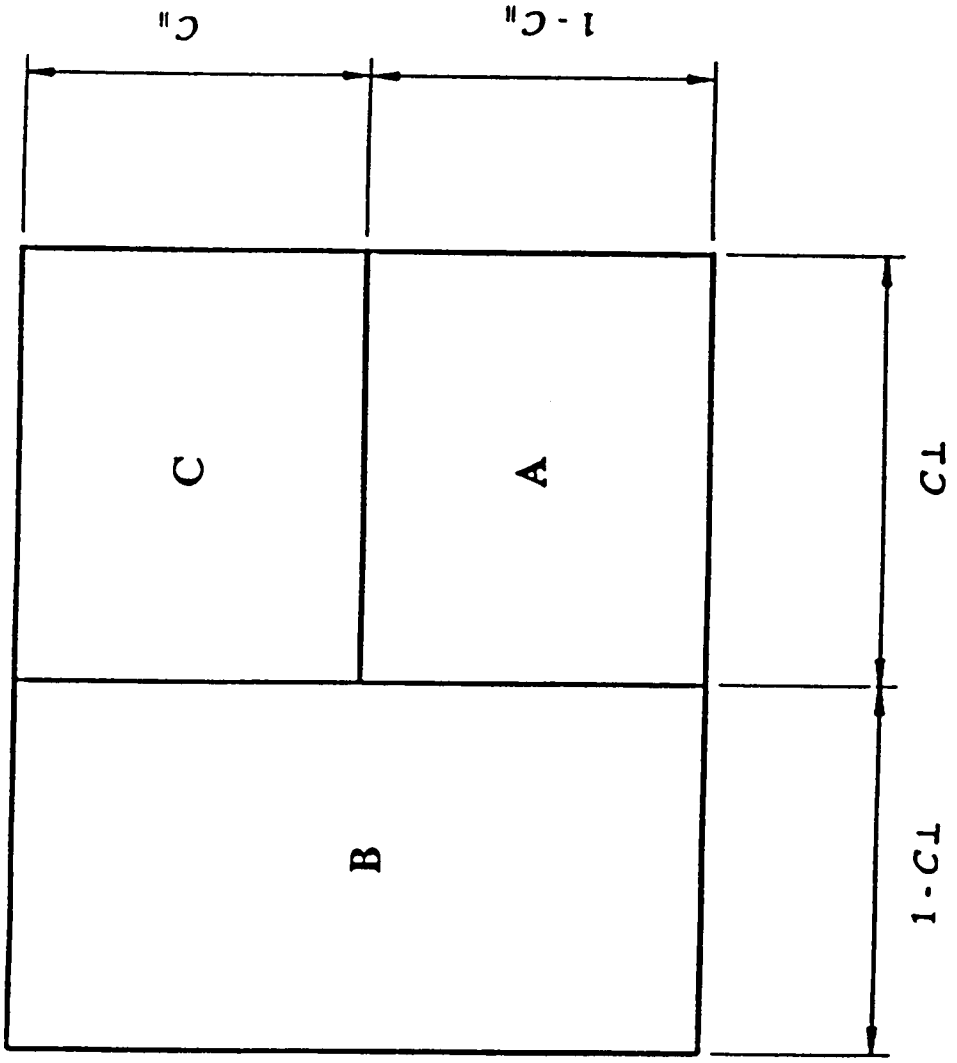

Fig. 6.1-1 Schematic representation of the structure model for PE fibers. C represents the crystalline domain. B represents the intermediate phase, held in its metastable state by connections to C. A consists of intermediate and most of the remaining amorphous phase.

Appendix B:
Tables

Table 1. Properties of the PE Fibers

Sample[a]	Modulus,[b] GPa	Tensile strength,[b] GPa	Density, Mg/m^3	Crystallinity, %
PE-I	179	3.9	0.964	80
PE-II			0.971	84
PE-III	125	2.7	0.974	86
PE-IV	59	1.6	0.978	88

[a]Gel-spun fibers supplied by Allied-Signal Corp. with MW > 10^6

[b]Data Supplied by Allied-Signal Corp.

Table 2. PE Crystal Structure from Full-Pattern Refinement

	PE-I	PE-II	PE-III	PE-IV
a, nm	0.7410	0.7388	0.7422	0.7379
b. nm	0.4950	0.4923	0.4944	0.4924
c, nm	0.2551	0.2550	0.2548	0.2544
Density, Mg/m^{-3}	0.996	1.004	0.996	1.008
Disorientation, deg.	0.73	1.29	1.15	1.88
Crystallite size, nm				
$L_1 = L_2$, (lateral)	17.6	9.4	7.7	6.3
L_3, (axial)	10.8	5.8	5.8	5.8
C-C Bond, nm	0.151	0.151	0.152	0.152
C-C-C angle, deg.	115.5	114.9	114.0	113.8
Setting angle, deg.	44.9	44.7	44.7	45.0
Paracrystallinity, 10^4 nm^2				
$T_{11} = T_{22} = T_{12} = T_{21}$	-2.26	2.81	2.53	-2.86
$T_{31} = T_{32}$	-0.84	0.84	0.71	-1.13
$T_{13} = T_{23}$	-0.19	0.27	0.02	0.15
T_{33}	0.18	-0.06	-0.03	0.01

Table 3. Phase Fractions Determination by Solid State NMR

	M_{mono}	M_{Inter}	M_{orth}	M_{amor}
PE-I	11%	13%	73%	3%
PE-IV	14%	12%	64%	10%

Table 4. ^{13}C Spin-Lattice Relaxation Time T_1 (in seconds)

	$T_{1,orth}$	$T_{1,Inter}$	$T_{1,amor}$
PE-I	319.1	9.4	0.28
PE-IV	756.4	17.4	0.22

Table 5: Fiber heat capacities

T / K	PE-I C_p /J mol^{-1} K^{-1}	PE-II C_p /J mol^{-1} K^{-1}	PE-III C_p /J mol^{-1} K^{-1}	PE-VI C_p /J mol^{-1} K^{-1}
175	14.25	14.32	14.18	14.27
180	14.75	14.75	14.75	14.75
185	14.98	15.08	15.07	15.07
190	15.46	15.50	15.46	15.46
195	15.57	15.76	15.60	15.69
200	16.06	16.16	16.11	16.18
205	16.27	16.43	16.33	16.39
210	16.79	16.80	16.69	16.81
215	16.96	17.13	16.94	17.07
220	17.46	17.50	17.35	17.55
225	17.67	17.72	17.69	17.81
230	18.19	18.12	18.07	18.30
235	18.40	18.47	18.36	18.57
240	18.93	18.94	18.86	19.06
245	19.15	19.23	19.18	19.47
250	19.73	19.73	19.58	19.94
255	20.00	20.18	19.93	20.27
260	20.56	20.60	20.43	20.88
265	20.86	20.93	20.84	21.30
270	21.46	21.52	21.26	21.89
275	21.77	21.93	21.55	22.40
280	22.28	22.45	21.98	23.09
285	22.52	22.79	22.42	23.70
290	23.13	23.27	22.92	24.34
295	23.37	23.64	23.26	24.85

Table 5: Fiber heat capacities (contd.)

T / K	PE-I C_p /J mol^{-1} K^{-1}	PE-II C_p /J mol^{-1} K^{-1}	PE-III C_p /J mol^{-1} K^{-1}	PE-VI C_p /J mol^{-1} K^{-1}
300	23.95	24.12	23.79	25.43
305	24.19	24.34	24.22	25.69
310	24.84	24.86	24.76	26.22
315	25.22	25.35	25.24	26.68
320	25.73	25.85	25.69	27.31
325	26.04	26.21	26.15	27.72
330	26.67	26.79	26.76	28.32
335	27.17	27.30	27.19	28.86
340	27.74	27.87	27.72	29.61
345	28.18	28.43	28.39	30.24
350	28.90	29.11	28.99	30.92
355	29.44	29.61	29.60	31.62
360	30.12	30.38	30.33	32.46
365	30.84	31.05	31.10	33.45
370	31.57	31.86	31.84	34.29
375	32.62	32.77	32.84	35.90
380	33.49	33.75	33.77	37.08
385	34.89	35.03	35.16	39.54
390	36.04	36.17	36.32	40.35

Vita

Andreas Boller was born in Hittnau (ZH), Switzerland. He received his "Matura" from the Kantonsschule Zürcher Oberland in Wetzikon (ZH). After the mandatory military service in a transportation and logistics unit he went on to get his Masters Degree in Chemistry at the Swiss Federal Institute of Technology (ETH) in Zürich. The thesis dealt with the synthesis and characterization of biodegradable polymers for medical implants.

Working experience in the laboratory for special characterization in thermal analysis, under the guidance of Dr. H.G. Wiedemann introduced him to the many aspects of thermal analysis. Presented with the opportunity to perform thermal analytical characterizations on ancient artefacts in the desert of China or pursuing doctoral research in the Advanced THermal AnalysiS (ATHAS) Laboratory with Prof. B. Wunderlich, he chose to investigate the thermal properties of polymers. In the course of these studies he of a new method in differential scanning calorimetry. The advancement of knowledge on Temperature Modulated Differential Scanning Calorimetry (TMDSC) resulted in twelve publications, four presentations at thermal analysis meetings and an invited plenary lecture at the Ohio Regional Thermal Analysis Symposium in May 1996.

Andreas Boller is a member of the North American Thermal Analysis Society (NATAS), the American Physical Society (APS), and the American

Chemical Society (ACS). He also is the cofounder of the first chapter of the Young Chemists Committee (YCC) in the Southeast.

Andreas Boller is married to Maria Cecilia Austin, formerly of Greeneville, Tennessee.